

TECHNICAL UNIVERSITY OF LIBEREC
Faculty of Mechanical Engineering



Dynamic behaviour of laser-induced cavitation bubbles

Ph.D. Thesis
by Ing. Miloš Müller

Doctoral Degree Programme:
Fluid Mechanics and Thermodynamics

Supervisor:
Prof. Ing. František Maršík, DrSc.

2007

Liberec

ANOTACE

Tato práce se zabývá studiem kavitačních bublinek se zaměřením na laserem indukovanou kavitaci v regulární a neregulární (retrogradní) tekutině. V úvodní fázi jsou shrnuty výsledky uvedené v literatuře zabývající se studiem efektů provádějících laserem indukovaný "break-down", jako jsou expanze plazmy, dynamika kavitační bublinky a šíření rázových vln. Provedená rešerše ukázala, že v dřívějších pracích nebyla věnována dostatečná pozornost porovnání dynamiky růstu a kolapsu bublinky v různých tekutinách včetně posouzení vlivu vlastností tekutiny na kolaps bublinky. Rešerše dále odhalila, že pouze v několika pracích byl analyzován vliv způsobu generace (typu laseru, vlnové délky) na tvar bublinky.

Dynamika bublinky byla posuzována jak z teoretického hlediska, tak i z experimentů provedených ve třech různých tekutinách. Nejprve byl připraven experiment využívající pulzní Tm-Yag laser s vlnovou délkou 2000 nm a trváním pulzu 1 ms a Nd-Yag laser s vlnovou délkou 1064 nm a trváním pulzu 6 ns. Růst a kolaps bublinky s doprovodnými rázovými vlnami byl vizualizován nově vyvinutou metodou vícenásobné expozice, pomocí níž lze bublinku zaznamenat do jednoho snímku v různých fázích. Dále byl studován vliv pevné stěny na dynamiku bublinky, umístěním L-profilu do blízkosti místa vzniku bublinky. Hustota tekutiny uvnitř bublinky byla odhadována z její rychlosti stoupání v glycerinu. Experimentální výsledky ukázaly na značný rozdíl v chování bublinky ve vodě, isooktanu a glycerinu. Data získaná z experimentů byla použita k ověření fyzikálního modelu laserem indukované bublinky. Odvozené diferenciální rovnice dynamiky bublinky uvažují vazkou stlačitelnou tekutinu s vlivem povrchového napětí a s počátečními podmínkami respektujícími pohlcení energie laseru tekutinou. Počáteční rychlost růstu poloměru bublinky byla modelována na základě úvahy, že bublinka je obálkou expandující plazmy, která vznikne pohlcením energie laserového pulzu. Pro výpočet šíření rázových vln je použita modifikovaná metoda charakteristik, která však neuvažuje vliv disipace energie. Disipace energie rázové vlny byla zahrnuta použitím poloempirického modelu založeného na předpokladu podobnosti časových průběhů tlaků v různých čela rázové vlny. Tento předpoklad je formulován pomocí dvou jednoduchých diferenciálních rovnic pro skokovou změnu tlaku a energii rázové vlny. Počáteční podmínky pro rovnice poloempirického modelu jsou stanoveny řešením rovnic šíření rázové vlny bez disipace. Na základě výpočtu tlakového pole obklopujícího bublinku bylo určeno rozdělení energie laserového pulzu na mechanickou energii rázové vlny, energii pro růst bublinky, energii vyzářenou plazmou a energii potřebnou k odpaření objemu tekutiny bublinky. Pro modelování kolapsu bublinky v blízkosti pevné stěny byl použit komerční software Fluent, s jehož využitím byla dynamika pohybu fázového rozhraní modelována pomocí metody Volume of fluid - VOF. Vypočítané deformace bublinky při kolapsu dobře korespondují s tvary zaznamenanými při experimentu.

ABSTRACT

This work studies cavitation bubbles with a special emphasis on the laser-induced cavitation in regular and irregular (retrograde) fluids. The introductory part reviews the literature dealing with the effects of the laser-induced breakdown such as plasma expansion, cavitation bubble dynamics and shock wave propagation. The review indicates that only some attention has been paid to comparing cavitation bubble dynamics in different liquids including the influence of the liquid properties on the bubble collapse. In addition, only a small fraction of the reviewed works concentrated on the influence of bubble generation (laser type, wavelength) on the bubble shape.

The cavitation bubble dynamics was studied theoretically and experimentally in three different liquids. First, experiments using the pulsed Tm-Yag laser with the wavelength 2000 nm and the pulse width 1ms and the Nd-Yag laser with the wavelength 1064 nm and the pulse width 6 ns were set up. The bubble growth and collapse with the attending shock waves were visualized using the newly designed multi-exposure method, which allowsto record into one frame different bubbles at the same time phase. Next, the influence of the solid wall on the bubble behaviour was investigated by placing an L-shaped profile close to the bubble origin. The density inside the bubble was estimated from its rising velocity in glycerine. The experimental results showed considerable differences in the behaviour of the bubble in water, isooctane and glycerine. The data obtained from the experiments were used for the verification of the physical model of the laser-induced bubble. The differential equations for the description of bubble dynamics consider viscous compressible liquid with the influence of surface tension and with the boundary conditions based on the absorption of the laser energy by the liquid. The initial velocity of the bubble radius was modelled using the assumption that the bubble formed an envelope of the expanding plasma, which originated from the absorption of the laser pulse. The shock wave propagation was calculated using the modified method of characteristics, which neglected the dissipation processes. The dissipation of the shock wave energy was included by using a semi-empirical model, which was based on the assumption of similarity between the shock pressure-time profiles in different shock front positions. This assumption led to a system of two ordinary differential equations for the pressure and energy jump in the shock wave. The initial conditions for the equations of the semi empirical model were obtained from the solution of the shock wave propagation without dissipation. The calculation of the pressure field surrounding the bubble was then used to break up the energy of the laser pulse into the mechanical energy of the shock wave, the bubble growth energy, the energy radiated by plasma and the energy required for evaporation of the liquid forming the bubble contents. The bubble collapse near the solid wall was calculated using the commercial software Fluent, which utilized the Volume of Fluid method (VOF) for the calculation of the phase interface dynamics. The resulting deformations during the bubble collapse and expansion show good agreement with the shapes recorded during the experiment.

ACKNOWLEDGMENTS

Before getting started, I would like to thank the people who made this thesis possible and who supported me in many ways. First of all, I would like to express my gratitude to my advisor Prof. Ing. František Maršík, DrSc., whose ideas have been my main inspiration and whose advise helped to steer me away from mistakes. I would also like to thank Prof. Dr. Walter Garen for his kind supervision during my externship at the university in Emden and to Dipl. Ing. Sandra Koch, my colleague there, for her friendship and help with the experiments. I am also very grateful to Doc. Ing. Jiří Unger, CSc., who supported me a lot and whose effort helped me to complete this work. I would also like to thank the people who worked together with me in various projects during the past years, namely Ing. Lukas Popelka, PhD., Ing. Patrik Zima, PhD., Ing. Jan Hrubý, CSc., and many others for their thoughts and invaluable help.

This work has been supported by the grant no. 4674788501 of the Ministry of Education.

Miloš Müller

CONTENTS

Contents	5
List of symbols	7
CHAPTER 1. Introduction	10
1.1 Definitions	10
1.2 Classification of cavitation	11
1.3 Adverse effects of cavitation	12
1.4 Utilization of cavitation	13
CHAPTER 2. Objectives	15
CHAPTER 3. current state of knowledge	16
3.1 Balance equations	16
3.1.1 General balance equation	16
3.1.2 Balance of mass	18
3.1.3 Balance of momentum	19
3.1.4 Balance of total energy	20
3.1.5 Constitutive relations	20
3.2 Laser-induced breakdown	21
3.2.1 Main effects accompanying LIB in aqueous media	21
3.2.2 Plasma dynamics	24
3.3 Cavitation bubble dynamics	27
3.3.1 Rayleigh-Plesset equation	28
3.3.2 Bubble stability	29
3.3.3 Bubble collapse	32
3.3.4 Dynamics of cavitation bubble in compressible liquid	33
3.3.5 Influence of viscosity and surface tension on bubble dynamics	35
3.3.6 Dynamics of non-spherical bubble	36
3.4 Theory of shock waves	38
3.5 Regular and retrograde fluid	45
CHAPTER 4. Experiment and measurement	46
4.1 Measurement methods and experimental devices	46
4.1.1 Basic principle of lasers - types of lasers	46
4.1.2 Principles of optical methods used in measurements	48
4.1.3 Methods of the shock wave and bubble measurements	49
4.1.4 Single and multi-exposure recording	50
4.2 Experimental setups	52
4.2.1 Experimental setup using Tm-Yag laser	52

4.2.2	Experimental setup using Nd-Yag laser.	53
4.3	Measurement results	56
4.3.1	Results of measurements using the Tm-Yag laser.	56
4.3.2	Results of measurements using the Nd-Yag laser	59
4.3.3	Cavitation bubble collapse near a solid wall and in free liquid.	64
4.3.4	Cavitation bubble rising in glycerine.	65
4.4	Summary of the measurement results	67
CHAPTER 5. Problem solution		69
5.1	General strategy.	69
5.2	Physical model.	71
5.2.1	Plasma growth modelling.	71
5.2.2	Application of the compressible model of the bubble dynamics.	72
5.2.3	Pressure and velocity fields in the liquid surrounding the bubble.	74
5.3	Energy distribution	76
5.3.1	Shock wave energy	76
5.3.2	Cavitation bubble energy	77
5.3.3	Energy of evaporation of the bubble content.	78
5.3.4	Energy radiated by plasma.	78
5.4	Semi-empirical solution of the shock wave propagation	78
5.5	Cavitation bubble in glycerine.	83
CHAPTER 6. Results		86
6.1	Numerical simulation of the laser induced bubble dynamics	86
6.2	Numerical simulation of the pressure and velocity field.	88
6.3	Evaluation of the shock wave pressure-time profiles	91
6.4	Numerical simulation of energy dissipation at the shock wave	92
6.5	Energy distribution during the bubble growth and collapse	94
6.6	Density of cavitation bubble rising in glycerine	94
6.7	Numerical simulation of bubble collapse	94
CHAPTER 7. Conclusion		99
7.1	Summary and critical evaluation.	99
7.2	Application and near objectives	101
	References	103
	Author's publications	105
	Appendix A	107
	Appendix B	109
	Appendix C	111
	Appendix D	113
	Appendix E	115

LIST OF SYMBOLS

ROMAN LETTERS

a	[m ²]	Surface
B	[Pa]	Coefficient of Tait's equation
c	[m.s ⁻¹]	Speed of sound; Speed of light
c_v, c_p	[J.kg ⁻¹ .K ⁻¹]	Specific heat at constant volume, Specific heat at constant pressure
d	[m]	Diameter, Distance
E	[J]	Energy
h	[J.kg ⁻¹]	Specific enthalpy
I	[J.m ⁻² .s ⁻¹]	Irradiance
j^k		Flux density of quantity Φ in space coordinates
$J(\Phi)$		Total flux of a balanced quantity
l	[m]	Length
m	[kg]	Mass
n	[-]	Coefficient of Tait's equation, Refractive index
t	[s]	Time
P	[W]	Power
$P(\Phi)$		Total production of the balanced quantity Φ
p	[Pa]	Pressure
R	[m]	Bubble radius
R_G	[J.kmol ⁻¹ .K ⁻¹]	Universal gas constant
r	[m]	Radial coordinate
s	[J.kg ⁻¹ .K ⁻¹]	Specific entropy
T	[K]	Temperature
t^{kl}	[Pa]	Stress tensor
t^k	[Pa]	Density of the surface forces per unit surface area ∂V
u	[m.s ⁻¹]	Shock wave velocity
V	[m ³]	Volume
∂V	[m]	Boundary of the volume V
v	[m.s ⁻¹]	Particle velocity
w	[m]	Beam radius
w_0	[m]	Beam waist radius
x, y, z	[m]	Cartesian coordinates

Y	[J.kg ⁻¹]	Specific kinetic enthalpy
z_{Ra}	[m]	Rayleigh's length

GREEK LETTERS

α	[m]	Absorption coefficient
β	[-]	Relation between the LIB threshold parameters and Gaussian beam parameters
Γ	[-]	Gamma function
γ	[-]	Polytrophic coefficient
ε	[J]	Internal energy; Emissivity
λ	[m]	Wave length, heat conduction coefficient
μ	[Pa.s]	Dynamic viscosity
ν	[m ² .s ⁻¹]	Kinematic viscosity
σ	[N.m ⁻¹]	Surface tension
σ^k		Density of production of quantity Φ in space coordinates
σ_B	[-]	Ratio between the distance of the bubble from a wall and its maximum radius
τ_{La}	[s]	Full width at half maximum of the laser power
τ_{col}	[s]	Collapse time
τ'	[-]	Dimensionless time
ϕ		Density of an extensive quantity in space coordinates
φ	[m ² .s ⁻¹]	Velocity potential
Φ		Total amount of quantity φ

SUBSCRIPTS

B	Bubble
bd	Breakdown
$crit$	Critical value
dis	Dissipated
G	Gas
L	Liquid
La	Laser
P	Plasma
R	Value at the bubble wall

<i>Ra</i>	Rayleigh
<i>s</i>	Shock wave
<i>sat</i>	Saturation line
<i>v</i>	Vapor
∞	Infinity, far in liquid
<i>0</i>	Initial value

1. INTRODUCTION

Cavitation is a unique phenomenon, which occurs in many fields of human activities. Although the presence of cavitation is most obvious in the field of hydrodynamics it can occur in any hydraulic machinery. Cavitation is not generated only in water, but in any kind of liquid. The presence of cavitation causes many troubles in the design of pumps and turbines. It can also be observed in the nature in running waters, where it takes many different forms. In contrast to the adverse effects, there is a great potential to utilize cavitation for various useful applications.

In recent years the cavitation generated by a beam of highly concentrated light in liquid has become a substantial area for research in the field of biophysics, biomedical engineering, and medicine. This type of cavitation does not fit into the classical definitions; however, it represents an excellent opportunity for laboratory modelling of cavitation phenomena.

This chapter proposes to classify the problem studied in this work, defines the fundamental terms in order to prepare background for statements in the following chapters and provides some examples of adverse effects of cavitation as well as its applications.

1.1 Definitions

The term *cavitation* originates from the Latin word *cavea*, which means a hollow place. Cavitation in general can be defined as a collection of effects associated with the formation, occurrence and activity of macroscopic cavities in liquid. The cavities can be void, or filled with gas or vapour or their mixture. Isolated cavities are often called *bubbles*.

The formation of new cavities involves two phases - nucleation and growth. *Nucleation* is a process by which nuclei of a new phase are formed in the previously homogeneous liquid body or solid. The term "nucleus" is defined as the smallest microscopic region of the new phase, which is capable of spontaneous growth. If this nucleus arises spontaneously because of macroscopic fluctuation or intermolecular interaction, this process is called *homogeneous nucleation*, whereas if it arises near a wall or on a foreign inclusion, the nucleation is called *heterogeneous*. If the nuclei are stable and specific conditions are met, they expand to a macroscopic size. This is termed *bubble growth*. The subsequent life of the bubbles, for example their oscillation, collapse, interaction with the ambience and other bubbles, shape deformation and formation of cavitation structures, is called bubble activity.

The cavitation generated by the absorption of highly concentrated light in a liquid is very closely associated with the term *laser-induced breakdown* (LIB), which denotes the dielectric breakdown due to partial or complete ionization of a solid, liquid or gas through absorption of thermal or electromagnetic energy. The ionization results in the formation of gas of charged particles, *plasma*, which constitutes the fourth state of matter.

In the scope of this work, the term *Laser* (acronym for Light Amplification by Stimulated Emission of Radiation) refers to a device that emits highly amplified and coherent radiation on one or more discrete frequencies.

1.2 Classification of cavitation

One way of classifying cavitation is according to the bubble content and the way of inducing the bubble growth. The bubble can contain gas or vapour or a mixture of both. For a gas-filled bubble, the growth can be caused by pressure reduction, increase in temperature or mass diffusion across the bubble boundary. If the bubble contains mainly vapour (see Figure 1.1), reducing the ambient pressure at nearly constant temperature causes an explosive vaporization into the cavities. This process is called vapour cavitation and it is initiated by overcoming the tensile strength of the liquid. On the contrary, vaporization initiated by superheating the liquid at nearly constant pressure is called boiling. Vapour cavitation thus appears similar to boiling except that the driving mechanism is not a temperature change but a pressure change. In practice, the bubble contains a mixture of gas and vapour, but one of the components can be of more importance.

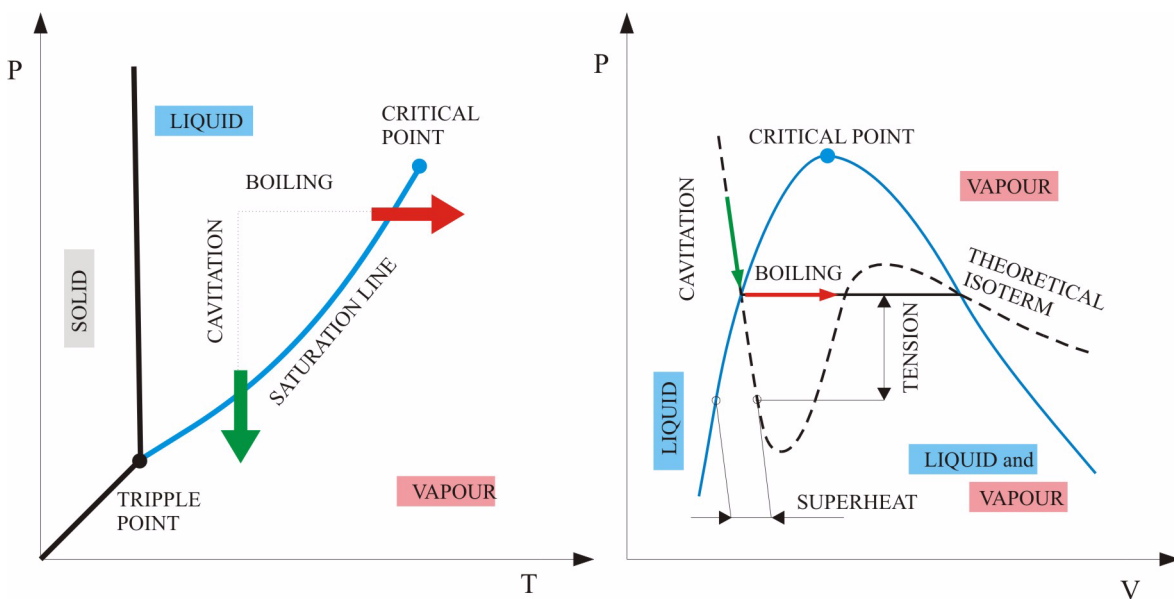


Fig.1.1 Typical phase diagrams illustrating the difference between cavitation (green curves) and boiling (red curves).

Another way of classifying cavitation is according to the way of bubble generation. From this point of view we can distinguish four types of cavitation.

Hydrodynamic cavitation - occurs when the liquid flows through a region of lower pressure, e.g. in accelerated flow inside of a pump or around an obstacle, such as a rapidly spinning propeller. The pressure of the fluid falls due to increased speed and when the pressure drops below the vapour pressure of the liquid, it vaporizes.

Acoustic cavitation - is produced in a non-flowing system when the ambient pressure varies by applying a strong acoustic field. The high intensity acoustic field leads to rupturing the liquid and formation of cavities or bubbles. If the pressure amplitudes are increased to produce negative pressures, the bubble growth is accelerated. Cavitation bubbles in ultrasonic fields aggregate into

1.3 INTRODUCTION - ADVERSE EFFECTS OF CAVITATION

various structures due to attractive and repulsive forces exerted by the acoustic field and the interaction between the oscillating bubbles.

Optical cavitation - is produced by photons of high intensity light generated by lasers focused into the liquid. This type of cavitation is therefore more often called *laser-induced cavitation*. The strong laser pulse produces a vapour cavity - bubble, which first expands and then collapses with several successive rebounds. Laser-induced cavitation is one of many effects associated with the foregoing phenomenon - LIB. The optical cavitation can also be interpreted as a mechanical effect of LIB. Considering that the laser induced-breakdown is one of the fundamental definitions of the presented work it will be described in detail in the following chapters.

Particle cavitation - is produced by any other type of elementary particles, e.g. a proton. It is based on the growth of bubbles in a superheated liquid. If a charged particle is sent through the liquid, it creates a ionization track. The liquid around the track is vaporized, forming microscopic bubbles that grow to a macroscopic size.

These four types of cavitation can be organized into two supergroups: the *tension cavitation*, which is produced via a drop in pressure, includes hydrodynamics cavitation and acoustic cavitation and the *energy deposition cavitation*, which includes optical cavitation and particle cavitation.

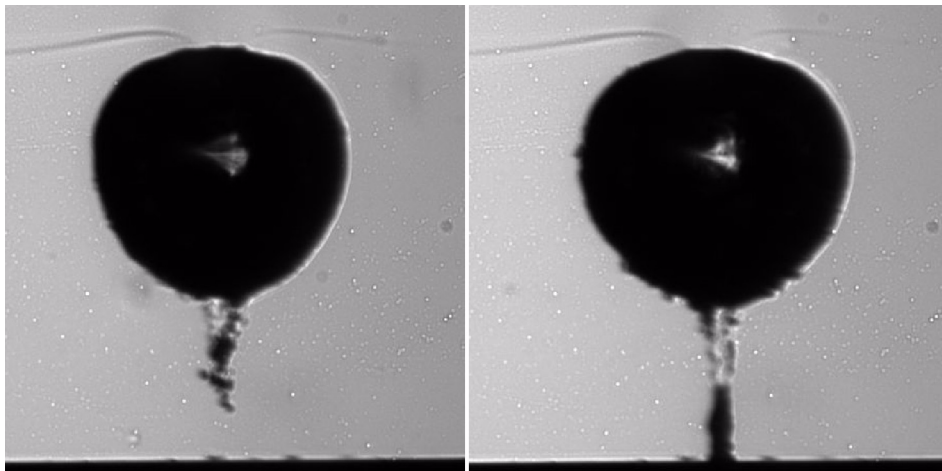


Fig.1.2 A bubble generating a liquid jet against the solid wall during the collapse. (Author's own experiment.)

1.3 Adverse effects of cavitation

If a system operating with fluid is designed, the fluid is assumed to be homogenous, but the presence of cavitation can dramatically change the characteristics and behaviour of such system. The presence of cavitation can cause decrease in turbo machinery efficiency due to thrust lowering, increasing of drag force and appearance of additional forces on solid surfaces. Cavities dissolved in the vehicle brake system can change the density of the working liquid in an unsuitable moment and thus cause an accident. Finally, the generation of noise and vibration can also indicate the presence of cavitation.

1.4 INTRODUCTION - UTILIZATION OF CAVITATION

The undesirable phenomena associated with cavitation are mostly caused by thermal and mechanical effects accompanying the bubble collapse. One of the most famous is the cavitation erosion. It represents a mechanical degradation of solid materials, which arises when cavities (or bubbles) collapse near solid walls. These unwelcome effects typically affect screw-propellers, water turbines, pumping devices and pipe systems. The cavitation erosion due to the bubble collapse is primarily caused by two effects. The first one is generation of high speed liquid jet against the wall (see Figure 1.2) and the second one is production of acoustic energy in the form of shock waves.

The thermal effect of cavitation appears during the bubble implosion, when the gas trapped inside the bubble is highly compressed. The temperature in such a collapsing bubble is in the range from 4000K to 9000K, which corresponds to the plasma temperature. Since the compression occurs in a very short time interval, only a small fraction of heat is transferred to the surrounding liquid and thus to the solid walls. Nevertheless, these high temperatures can cause local burning of liquid, as it was observed in hydraulic shock absorbers by Müller [62].

Cavitation can also be found in the human body, living organisms and plants. Syringomyelia, development of a fluid-filled cavity or syrinx within the spinal cord, can cause back pain, headaches, and weakness. Cavitation in arteries and veins can damage heart valves and cause arteriosclerosis.

LIB in liquids is followed by expansion of plasma, which leads to production of shock waves or acoustic waves and to formation and collapse of cavitation bubbles in the liquid. These mechanical effects of LIB are typically more important than the plasma expansion itself, because they represent the plasma action on the surrounding liquid far from the breakdown site. For LIB within the eye, the high peak pressures generated by shock waves and large cavitation bubble expansion are a potential tissue damage mechanism. It is not clear whether the majority of tissue damage is induced by cavitation effects (bubble jet) or by shock waves, but the recent research work of Vogel [24] indicates that cavitation effects cause more tissue damage than the shock waves, which have only a short duration.

1.4 Utilization of cavitation

The negative effects of cavitation are often stressed, although cavitation is frequently used in many industrial processes. For its ability to concentrate energy on small surfaces and produce high pressure peaks, cavitation is used for surface cleaning by ultrasonic energy or cavitation jets [25]. Because ultrasound travels thorough metals and many other materials, the ultrasonic energy penetrates into blind holes and complex shapes, which cannot be reached by any other method.

An important application of cavitation is in water treatment [26]. Acoustic irradiation of polluted waters can influence the cleaning process in different ways, depending on the type of pollutant. Cavitation bubbles are responsible for the degassing of gas pollutants by rectified diffusion, bubble coagulation and bubble drift. Bubbles can separate solid pollutants from the liquid by accumulation at bubble surface and agglomeration due to bubble drift. Free radicals that are produced during the strong bubble collapse neutralize chemical pollutants. Shear flows, shock waves

and erosion mechanisms of strongly oscillating bubbles and the additional chemical impact of free radicals can deactivate living microorganisms.

The ultimate case of cavitation is supercavitation, which is a hydrodynamic process in which a body submerged in the liquid is almost entirely enveloped in a layer of gas initiated at a cavitator mounted at the head of the body. Supercavitating bodies can achieve very high speeds under water by virtue of a reduced drag: with suitable design, cavitation bubble is generated at the tip and the skin friction is drastically reduced. The supercavitation principle is used in the design of high-performance propellers and underwater projectiles. In 1997, the Naval Undersea Warfare Centre developed an underwater bullet, which exceeded the velocity of 1500 m/s.

An example of the application of a single cavitation bubble is in *Laser Induced Breakdown Spectroscopy* (LIBS) as used e.g. by Koch [59]. When LIB produces plasma in the liquid, a large number of electrons is released. This process is followed by emission of photons whose energy characterizes the substance composition. One of the main limitations of LIBS for underwater analyses of solid targets is related to its relatively low sensitivity due to the plasma quenching process. The use of a dual-pulse technique could significantly improve LIBS sensitivity and resolution in liquid medium. Under water, the first laser pulse produces the cavitation bubble, while the second pulse ablates the sample and excites the plasma inside the bubble. The application of the second pulse in a gaseous environment prevents the plasma quenching that occurs in the liquid phase. An experimental setup for LIBS in a bubble is in Figure 1.3.

Laser-induced cavitation and its accompanying phenomena are also widely used in many medical applications. In laser lithotripsy, the shock waves and bubble microjets generated during the violent bubble collapse are used to break up stones formed in the urinary tract. Revascularization therapy uses liquid jets generated by the interaction of gas bubbles with shock waves to impact on the thrombi. Cavitation bubbles have been proved to be a driving force of tissue cutting during pulsed laser applications in vitreoretinal surgery.

There is an ambitious hypothesis that high temperatures reached during the violent bubble implosion, can produce thermonuclear fusion. Sonoluminescence and sonochemistry are generally thought to be well explained by this phenomenon.

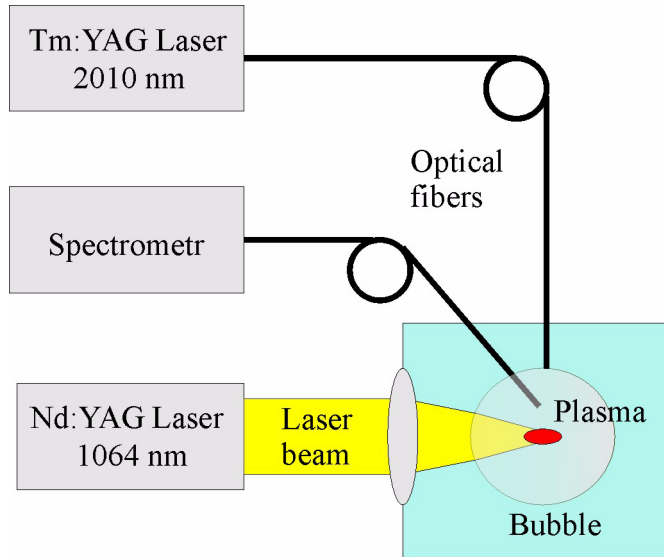


Fig.1.3 Experimental setup of LIBS in the cavitation bubble.

2. OBJECTIVES

The objectives of the present work were imposed into the framework of long term research in the field of cavitation and bubble dynamics, which simultaneously is carried out at the Technical University of Liberec, Institute of Thermomechanics of the Academy of Sciences of the Czech Republic and the University of Applied Sciences Oldenburg/Ostfriesland/Wilhelmshaven. This work focuses on cavitation, which is produced by an optical breakdown in liquid. Although the research activities in this area are extensive, especially in connection with medical applications of lasers, there are still many phenomena that have not been satisfactorily explained and remain in the state of presumptions. The main problem to be solved in technical and medical applications of laser induced breakdown (LIB) is to determine the mechanism of deposition of the energy of the laser pulse. Shock waves and cavitation bubbles usually occur in liquids as a mechanical effect of LIB and the knowledge of the energy deposition mechanism can help to describe their destructive effect. The investigations in this area are usually performed in regular liquids, mainly in water, and only few investigations have been realized in irregular liquids. The aim of the presented work is to contribute to the understanding of cavitation bubble phenomena with a focus on bubble dynamics in various liquids and the corresponding energy distribution. Special attention is paid to the comparison of the bubble dynamics during the collapse in those liquids. The experimental investigation of the effects accompanying LIB is often based on high-speed recordings where the resolution of such experiments is limited by the framerate of the camera. On this account this work also suggests to design a new measurement methodology within the frame of experiment, which would help to improve the recording possibilities and reproducibility of the measurement. The requirements for this work can be formulated as follows:

- 1) Make a thorough review of the literature on theoretical and experimental investigation of cavitation bubble phenomena with a special emphasis on laser-induced cavitation and the phenomena associated with the laser-induced breakdown in a liquid, such as shock waves produced during the bubble growth and collapse and cavitation bubble behaviour during its collapse near a solid wall.

- 2) Perform a detail analysis of the physical models and select an appropriate model for the description of the bubble dynamics, shock wave distribution and calculation of the energy associated with the different phases of the bubble life and for the simulation of the bubble interface deformation.

- 3) Design an experiment for investigation of cavitation bubble behaviour and shock wave emission in various types of liquids providing also a possibility of investigation of cavitation bubble collapse close to a solid wall with the aim of preparing experimental data for numerical simulations. For the experiment, design a new methodology to improve the recording possibilities and reproducibility of the measurement.

- 4) Perform a numerical simulation of the growth and collapse of the cavitation bubble in various liquids and of the accompanying shock wave phenomena. Calculate the deformation of the bubble interface during the collapse.

3. CURRENT STATE OF KNOWLEDGE

This chapter provides the fundamentals necessary for the solution of the problem treated in this work and presents an overview of the latest knowledge in the field of cavitation with the focus on laser-induced cavitation. Some findings and equations introduced in this chapter are used in *Chapter 5. Problem solution* to reach the physical and mathematical formulation of the problem.

Section 3.1 Balance equations introduces the basic equations describing the motion of fluid and the material relations for thermoviscoelastic material. *Section 3.2 Laser-induced breakdown* provides the basic principles of modelling of laser beam propagation in the liquid medium and of plasma dynamics. *Section 3.3 Cavitation bubble dynamics* gives an overview of the physical models of cavitation bubble behaviour in compressible and incompressible liquid, including the basic principles of modelling of dynamics of non-spherical bubble and its interaction with bodies. *Section 3.4 Theory of shock waves* describes the shock wave phenomenon as the product of LIB and bubble collapse. The physical models used for the calculation of the pressure and velocity distribution in the liquid surrounding the bubble are stated here. The chapter also describes the procedures for calculation of the shock wave energy. As the term irregular (retrograde) fluid is frequently used within this work, *Section 3.5 Regular and retrograde fluid* gives a short review of the retrograde behaviour.

3.1 Balance equations

The balance equations represent the fundamental principles of conservation of mass, momentum, energy and entropy, and together with the constitutive relations they form a complete description of the behaviour of fluid. As the entropy balance is not explicitly used in this work its balance is omitted in the following chapter, but it can be found e.g. in Maršík [3]. For the purpose of the problem treated in this work, the balance equations are formulated for the regions with moving discontinuities such as cavitation bubbles or shock waves. The balance equations are formulated in the Cartesian coordinate frame and then transformed into spherical coordinates, which are mostly used in this work. In the derivations, fluid passing through a volume fixed to the base is considered. It corresponds to the Euler account, though in some cases, if needed, Lagrange coordinates are used by considering a small volume moving with the fluid and containing the same definite mass of fluid at all times. The detailed derivation of the balance equations can be found e.g. in Bird [1], Maršík [3] or Šesták [4].

3.1.1 General balance equation

A general scheme of balance of a general quantity $\Phi(t)$, characterizing the behaviour of a system (fluid) and having the volume V (fixed in space) and the surface ∂V can be set as follows

3.1 CURRENT STATE OF KNOWLEDGE - BALANCE EQUATIONS

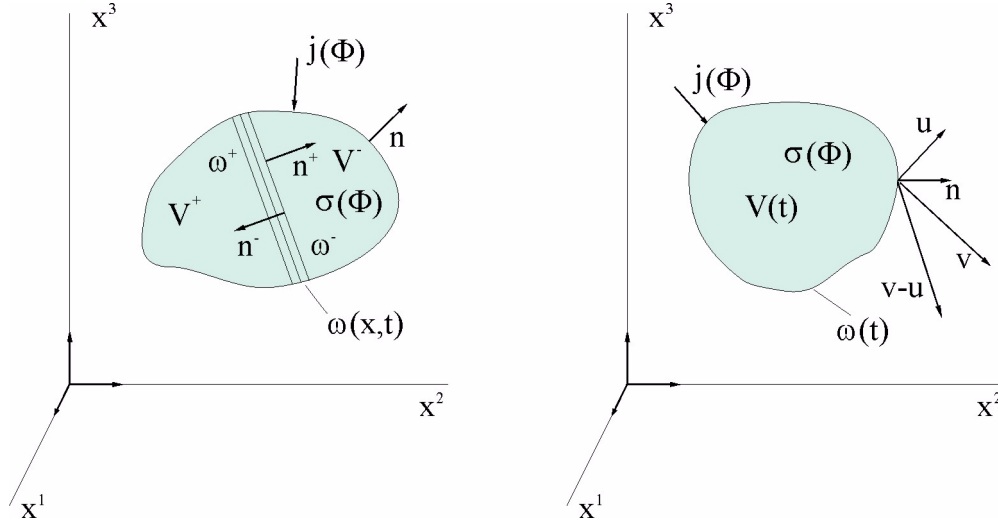


Fig.3.1 Right: The balance of quantity $\Phi(t)$ in a body of a volume V , where the discontinuity $\omega(t)$ occurs. Left: The moving discontinuity $\omega(t)$ representing the boundary of the volume.

$$\frac{d\Phi(t)}{dt} = J(\Phi) + P(\Phi). \quad (3.1)$$

The above equation reflects the general experience that the time change of the quantity $\Phi(t)$ in the volume V is caused due to

- a) The inflow (outflow) of the quantity $\Phi(t)$ in (out of) the body through its boundary ∂V
- b) the production (annihilation) of the quantity $\Phi(t)$ inside the body.

The total value of the quantity $\Phi(t)$ is given by the volume integral from its density $\phi(x,t)$

$$\Phi(t) = \int_{V-\omega} \phi(x,t) dV, \quad (3.2)$$

The quantity $J(\Phi)$ in Eq. (3.1) represents the flux of $\Phi(t)$ across the boundary ∂V and can be expressed by the surface integral

$$J(\Phi) = \int_{\partial V} j^k(\Phi) da_k, \quad (3.3)$$

where j^k is flux density of $\Phi(t)$ and a_k is an element of the boundary. Similarly, the total production $P(\Phi)$ of the quantity $\Phi(t)$ is given by

$$P(\Phi) = \int_{V-\omega} \sigma^k(\Phi) dV, \quad (3.4)$$

3.1 CURRENT STATE OF KNOWLEDGE - BALANCE EQUATIONS

where σ^k is the production of $\Phi(t)$ in the volume V . Having substituted (3.2), (3.3) and (3.4) into the general balance Eq. (3.1) and having performed the material derivative in (3.1), after using the Gauss theorem the global balance law can be obtained in the form

$$\int_{V-\omega} \left[\frac{\partial \Phi}{\partial t} + \frac{\partial(\Phi v^k)}{\partial x^k} - \frac{\partial j^k(\Phi)}{\partial x^k} - \sigma(\Phi) \right] dV + \int_{\omega} \left\| \Phi(v^k - u^k) - j^k(\Phi) \right\| = 0, \quad (3.5)$$

where u^k is the velocity of the discontinuity ω and v^k is the velocity of the particle close to the boundary surface. The double bracket in the above equation defines the difference of the values on the discontinuity. In order to include the discontinuity into the balance equation, the body has to be divided into two overlapping parts as shown in Figure 3.1. Eq. (3.5) can also be used when the discontinuity represents the surface of a body. The moving discontinuity can be represented by a bubble wall or a shock wave. In the case of the bubble, the non-zero particle velocity v_k simulates the transfer of mass through the bubble surface. Because no restriction was imposed on the volume V , the balance (3.5) has to be valid for any volume. Reducing the volume V to an infinitesimal one, the local form of the general conservation law takes the form

$$\frac{\partial \Phi}{\partial t} + \frac{\partial(\Phi v^k)}{\partial x^k} - \frac{\partial j^k(\Phi)}{\partial x^k} - \sigma(\Phi) = 0 \quad (3.6)$$

for the volume V and

$$\left\| \Phi(v^k - u^k) - j^k(\Phi) \right\| = 0 \quad (3.7)$$

for the discontinuity ω .

3.1.2 Balance of mass

The simplest restriction of the motion of fluid is the mass conservation. If the mass m is used in Eq. (3.4) instead of the general quantity $\Phi(t)$, it takes the form

$$m(t) = \int_{v-\omega} \rho dV. \quad (3.8)$$

Neglecting the flux and the origin of the mass defined by Eqs. (3.3) and (3.4), the local balance of mass is

$$\frac{\partial \rho}{\partial t} + \frac{\partial(\rho v^k)}{\partial x^k} = 0 \quad (3.9)$$

for the volume V and

3.1 CURRENT STATE OF KNOWLEDGE - BALANCE EQUATIONS

$$\| \rho(v^k - u^k) \| n_k = 0 \quad (3.10)$$

for the discontinuity ω .

3.1.3 Balance of momentum

Momentum is defined as the mass of an object multiplied by the velocity of the object and it can be expressed in agreement with (3.2) as

$$\int_{v-\omega} \rho(x, t) v^i(x, t) dV. \quad (3.11)$$

The balance of momentum is an expression of Newton's second law. It describes the equilibrium between the external forces acting on the body and the inertial forces. In general, we may divide the acting forces into two major categories: the volume forces and the surface forces. The volume forces act on all elements of the body. The simplest volume force is that of gravitational attraction, but also important are electromagnetic forces. If the forces act only on the boundary of the body, they are called surface forces. The pressure, viscous friction or surface tension are examples of surface forces. The total impact of surface forces is expressed by the integral

$$\int_{\partial v-\omega} t^{ki}(x, t) n_k da, \quad (3.12)$$

where t^{ki} (see Eq. (3.22)) is the density of the surface forces per unit surface area ∂V with the outgoing normal n_k . The density of the surface forces is called local stress. Another contribution to the total balance of momentum is its production, expressed by the surface integral

$$\int_{v-\omega} \rho f^i dV, \quad (3.13)$$

which results from the acting volume forces. Having substituted Eqs. (3.11), (3.12) and (3.13) into the general balance law (3.5), the local balance of momentum takes the form

$$\frac{\partial \rho v^i}{\partial t} + \frac{\partial (\rho v^i v^k)}{\partial x^k} - \frac{\partial t^{ki}}{\partial x^k} - \rho f^i = 0 \quad (3.14)$$

for the volume V and

$$\| \rho v^i (v^k - u^k) - t^{ki} \| n_k = 0 \quad (3.15)$$

for the discontinuity ω .

3.1.4 Balance of total energy

It is known that the total energy of a system consists of the sum of mechanical energy $v^i v_i / 2$ and internal energy ε .

$$\int_{v-\omega} \left(\frac{v^i v_i}{2} + \varepsilon \right) dV \quad (3.16)$$

The total flux of energy into the system through its boundary is defined by

$$\int_{v-\omega} (t^{ki} v_i + q^k) da_k, \quad (3.17)$$

where the mechanical and the thermal interaction of the system with surroundings is assumed. Here, q^k is the heat flux and t^{ki} is the total impact of the surface forces acting on the body, introduced in Eq. (3.12). The total production of the energy can be induced either by the volume forces or by other energetic effects included in the quantity \tilde{q} . The production of the total energy can be expressed as a sum of these two effects

$$\int_{v-\omega} (\rho f^i v_i + \tilde{q}) dV \quad (3.18)$$

Substituting Eqs. (3.16), (3.17) and (3.18) into the general balance equation the local balance of the total energy takes the form

$$\frac{\partial}{\partial t} \left\{ \rho \left(\frac{v^i v_i}{2} + \varepsilon \right) \right\} - \frac{\partial}{\partial x^k} \left\{ \rho v^k \left(\frac{v^i v_i}{2} + \varepsilon \right) - t^{ki} v_i + q^k \right\} - \rho f^i v_i - \tilde{q}. \quad (3.19)$$

for the volume V and

$$\left\| \rho \left(\frac{v^i v_i}{2} + \varepsilon \right) (v^k - u^k) - (t^{ki} v_i + q^k) \right\| n_k = 0 \quad (3.20)$$

for the discontinuity ω .

3.1.5 Constitutive relations

The basic equations for the determination of the velocity, pressure and temperature field in the liquid are the balance of mass (3.9), momentum (3.14) and energy (3.19). These equations and

one inequality include unknown functions for x^i , T , ε , q^i , v^i and t^{ij} . To determine the thermodynamic state of the system one has to establish the remaining functions. These functions have to satisfy the fundamental thermodynamic inequality, but they also have to satisfy many natural conditions, which are known as the axioms of constitutive relations. The complete derivation of the relations can be found in detail in Maršík [3]. The fluids considered in this work can be described by an isotropic Newtonian model, which uses the linear equations to express the heat flux and the stress tensor in the form

$$q^k = -\lambda(\rho, T)\delta^{kl}\frac{\partial T}{\partial x^l}, \quad (3.21)$$

$$t^{kl} = -p(\rho, T)\delta^{kl} + t_{dis}^{kl}, \quad (3.22)$$

$$t_{dis}^{kl} = \mu_v(\rho, T)d_{(1)}\delta^{kl} + 2\mu(\rho, T)\hat{d}^{kl}, \quad (3.23)$$

where λ is the heat conductivity, p is the pressure, μ_v and μ are volume and sharing viscosity, $d_{(1)} = \partial v^i / \partial x_i$ is the first invariant of the deformation velocity tensor and \hat{d}^{kl} is the differentiator of the deformation velocity tensor defined by

$$\hat{d}^{kl} = d^{kl} - \frac{d_{(1)}}{3} = \frac{1}{2}\left(\frac{\partial v_k}{\partial x_l} + \frac{\partial v_l}{\partial x_k}\right) - \frac{1}{3}\frac{\partial v^i}{\partial x_i}. \quad (3.24)$$

3.2 Laser-induced breakdown

3.2.1 Main effects accompanying LIB in aqueous media

In order to describe the initial stages of the life of a bubble created by focusing of the laser beam into the liquid medium and to understand some accompanying effects, some basics of plasma dynamics will be described in this chapter. The following paragraphs represent summary of findings published by Kennedy [9], Keldysh [10] and Vogel [23]. In these works, references to other literature sources can be found.

Most lasers produce beams of electromagnetic radiation whose transverse electric field and irradiance distributions are described by the Gaussian functions. Such beams are called Gaussian beams. The irradiance I_{La} denotes the power of electromagnetic radiation at a surface per unit area. To define the beam boundary, its diameter is defined at the position where the irradiance drops to $1/e^2$ (13.5%) of its value at the beam centre I_{La0} . It follows that decreasing the laser beam radius increases the irradiance value. To produce a breakdown, a part of the irradiance has to be absorbed into the liquid. The irradiance I_{La} absorbed in the liquid layer of thickness z can be expressed using the Beer-Lambert law

$$I_{La}(z) = -I_{La0}e^{-\alpha z}, \quad (3.25)$$

where α is absorption coefficient and I_{La0} is the irradiance value at the layer boundary. The dependence of the coefficient α on the wavelength in water is shown in Figure 3.2.

As it was mentioned in the introductory chapter, plasma is created as a result of ionization of gas. The ionization is the ejection of one or more electrons from an atom or molecule to produce a fragment with a charge. For this purpose, it is necessary to supply energy to the particles in the form of incident electromagnetic radiation. To ionize the matter, the irradiance has to reach a level noted as the ionization potential. In nature there are two possibilities of ionizing the matter. The first one is a thermally induced breakdown, where the matter is heated up to very high temperatures, which cause melting of the basic matter, vaporization and then ionization due to thermally induced collisions. Such kind of breakdown occurs in the sun. In electrostatic breakdown, which represents the second possibility of plasma production, the matter is exposed to a very strong electrostatic field. The plasma is produced by a process called electron cascade ionization or avalanche ionization. In this way the lightning bolt occurs in nature. An artificial process of plasma creation is the optical absorption of laser radiation produced by an intense electromagnetic field in lasers. Laser-induced breakdown takes two different forms: thermal breakdown and optical breakdown. Laser-induced thermal breakdown occurs in materials with almost linear absorption coefficients, when the radiation is acting on the matter in a relatively long time interval, such as in the case of lasers, producing continuous radiation or radiation with high repetitive frequency of high power. Relatively slow absorption process allows ionization due to the thermally induced collisions as in the case of naturally induced thermal breakdown. Optical breakdown, by contrast, occurs in the case of short laser pulses in the range from nanoseconds to femtoseconds. These short time intervals do not allow direct heating of matter due to the thermally induced collisions. In this regime, plasma is produced by electron cascade, also called cascade ionization, and direct

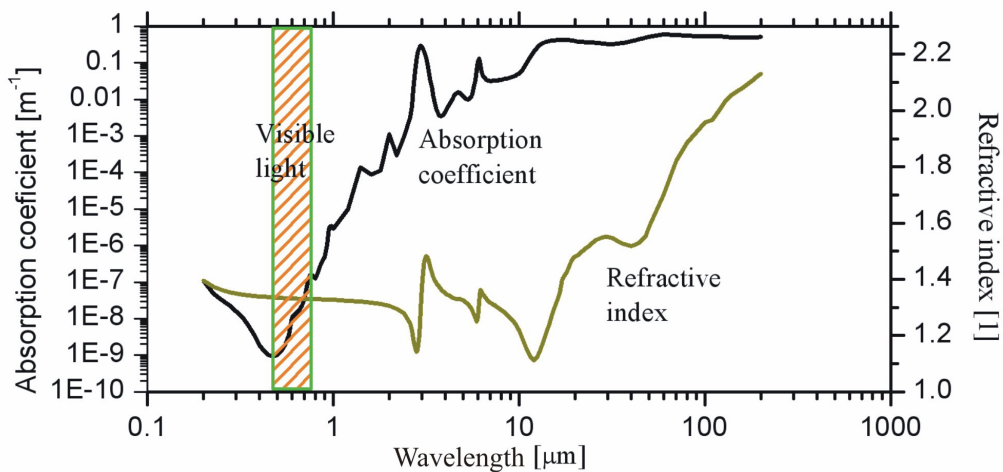


Fig.3.2 Absorption coefficient and refractive index in dependence on wavelength.

ionization of the matter by a multi-photon absorption. The multi-photon absorption is a process in which two or more photons are absorbed by an atom simultaneously, mimicking the effects of the absorption of a higher energy photon. Each electron is separately ionized by absorption of a group of photons. No other particles are needed for the initiation. The cascade ionization includes two steps, cascade initiation through

Ref., τ_{La}, λ	d (μm)	Medium	E_{bd} (μJ)	I_{bd} (W/cm^2)
Vogel $\tau_{La} = 6$ ns $\lambda = 1064$ nm	5.39	Distilled- H_2O	89.9	6.6×10^{10}
	7.66	Distilled- H_2O	140.6	5.1×10^{10}
	11.53	Distilled- H_2O	493.4	7.9×10^{10}
	14.57	Distilled- H_2O	1082.0	1.08×10^{11}
	47.78	Distilled- H_2O	8022.9	7.5×10^{10}
Kennedy $\tau_{La} = 7$ ns $\lambda = 1064$ nm	22.00	Ultrapure- H_2O	483	1.5×10^{10}
	22.00	Tap-Water	150	1.05×10^{10}
	22.00	Saline	221	3.96×10^9

Table 3.1 Experimental values for irradiance breakdown flash endpoint I_{bd} (long pulse width τ_{La}) and the corresponding energy E_{bd} for different materials in dependence on spot size d . The data originally published by Kennedy [9].

creation of seed electrons and cascade buildup to high free electron densities. Cascade initiation requires one or more free electrons to be present in the focal volume. In impure medium these electrons originate from impurities, but in pure media these electrons have to be created by a multi-photon absorption. The presence of impurities can significantly reduce initiation threshold of ionization. The cascade buildup is provided through inverse bremsstrahlung absorption. In that process, seed electrons absorb laser photons during the collisions with molecules or ions. Having achieved energy greater than the ionization potential, a free electron can ionize a bound electron and produce two free electrons of lower energy. Repetitions of this process leads to growth of the number of free electrons (free electron density) geometrically and to the breakdown. The threshold for the multi-photon absorption is usually higher than for the avalanche ionization so the cascade ionization is a much more common process. For long pulses, e.g. in the nanosecond regime, the breakdown is primarily caused by the cascade ionization, while the multi-photon absorption dominates the breakdown in the femtosecond regime. When plasma is created in the liquid it absorbs visible radiation much more strongly than the surrounding liquid (transparent matter). The incoming laser light is absorbed in plasma by the inverse bremsstrahlung absorption, which causes the heating of plasma to high temperatures in the order of 10^4 K.

In experiment, the breakdown in aqueous media is defined by detectable aftereffects, such as visible plasma emission, bubbles and shock waves. The visible plasma emission, however, can be observed for exposures in the range of nanoseconds or longer. For shorter pulses plasma emission becomes undetectable. Detection of cavitation bubbles or after collapse bubbles is used to find plasma endpoint in those cases.

The threshold irradiance needed to produce LIB in liquid depends on the material of the medium and the beam characteristic. Some characteristics of the irradiance threshold on the pulse width, are for different spot size figured in Table 3.1.

When plasma is created in the liquid, it is of high temperature and pressure. These conditions lead to plasma expansion at high velocities (as in gas), producing shock waves and cavitation

effects. When the plasma is produced by pulses in order of nanoseconds or picoseconds, it tends to expand back to the incoming beam. This phenomenon is known as moving breakdown. The moving breakdown causes plasma quenching into the focal volume because of a shielding effect of the plasma created on the side of the incoming light. The shielding effect is the reduction of the laser energy due to absorption, reflection or scatter. Plasma shielding also causes increasing of the focal volume. An increase of the plasma volume, after its formation, is supported by two effects. First, the high temperatures in the focal volume produce thermal expansion, and second, plasma expands due to the continued ionization. For a nanosecond pulse this leads to the formation of new plasma on the side of the incoming light. This phenomenon is being explained by three different mechanisms. First, the laser-supported detonation model postulates that the laser light is preferentially absorbed by plasma shock front. Second, ionization wave model postulates that new plasma is created by free electrons or ionizing radiation, which occurs in the original focal volume and then expands back to the direction of the incoming light. Third, moving breakdown model postulates that the breakdown occurs independently on the beam side at the position where the irradiance threshold is reached. It is at first in the focal volume and it continues along a path, as the irradiance threshold is being achieved.

After the laser pulse has passed, plasma begins the process of cooling. It is caused by the energy losses to the shock waves, heat conduction to the surrounding liquid, which cause the liquid vaporization and the cavitation bubble creation, and due to spectral emission. In the last stages the plasma decays through electron-ion recombination. The high temperature plasmas produce a luminescence spectrum, which arises from three sources. They are bremsstrahlung emission from free electrons, emission from electron-ion recombination and emission from bound state electronic transitions, which produce spectral lines characteristic for the material.

3.2.2 Plasma dynamics

As it was mentioned above plasma is produced by absorption of laser irradiation in the form of a beam, which usually takes the Gaussian distribution. The temporal shape of such a beam can be expressed in the following form

$$P_{La}(t) = P_{La0} e^{\left[(-4\ln 2)\left(\frac{t}{\tau_{La}}\right)^2\right]} \quad (3.26)$$

where P_{La0} is the maximal value of the laser power and τ_{La} is the pulse width at half maximum. The laser energy can be calculated by an integration of the laser power (3.26) over the pulse duration as

$$E_{La} = P_{La0} \int_{-\infty}^{\infty} e^{\left[(-4\ln 2)\left(\frac{t}{\tau_{La}}\right)^2\right]} dt = 1.064 P_{La0} \tau_{La}. \quad (3.27)$$

3.2 CURRENT STATE OF KNOWLEDGE - LASER-INDUCED BREAKDOWN

The laser beam is usually focused through optics to a small spot to increase the irradiance intensity above the breakdown threshold. The beam spot size $w(z)$ is a function of axial position z as

$$w(z) = w_0 \left(1 + \left(\frac{z}{z_0} \right)^2 \right)^{0.5}, \quad (3.28)$$

where w_0 is the beam waist at the focal point and

$$z_{Ra} = \frac{n\pi w_0^2}{\lambda} \quad (3.29)$$

is the Rayleigh range or focal region. Using the pulse width τ_{La} also the pulse length l_{La} is defined by

$$l_{La} = \tau_{La} c, \quad (3.30)$$

where c is the speed of light in the material. For the relatively long-duration laser pulses (in the range of nanoseconds) the pulse length is much higher than the region where the beam is focused. For a pulse with the duration $\tau_{La} = 1$ ns, wavelength $\lambda = 800$ nm and $w_0 = 20$ μm l_{La} is approximately equal to 30 cm. Therefore, it is possible to assume that the laser pulse originates at one point and its character is dependent only on time. Supposing that the beam radius $w(z)$ is a function of the axial coordinate z according (3.28), the irradiance I can be reformulated as

$$I(t, z) = \frac{P_{La0}}{\pi w^2(z)} e^{\left[(-4 \ln 2) \left(\frac{t}{\tau_{La}} \right)^2 \right]} = I_{La0}(z) e^{\left[(-4 \ln 2) \left(\frac{t}{\tau_{La}} \right)^2 \right]}. \quad (3.31)$$

In some cases, the small region around the focus point - plasma, can be modelled as a cylinder with time changing length. To determinate the laser energy absorbed by plasma the Beer-Lambert law (3.25) can be used in a slightly different form

$$I_{La}(t) = I_{La0} e^{-\alpha z(t)_P}, \quad (3.32)$$

where α is the time independent absorption coefficient and $z(t)_P$ is the time dependent plasma length, which can be expressed as

$$z_P = z_{Ra} \sqrt{\beta (-4 \ln 2) \left(\frac{t}{t_P} \right)^2 - 1} \quad (3.33)$$

where

3.2 CURRENT STATE OF KNOWLEDGE - LASER-INDUCED BREAKDOWN

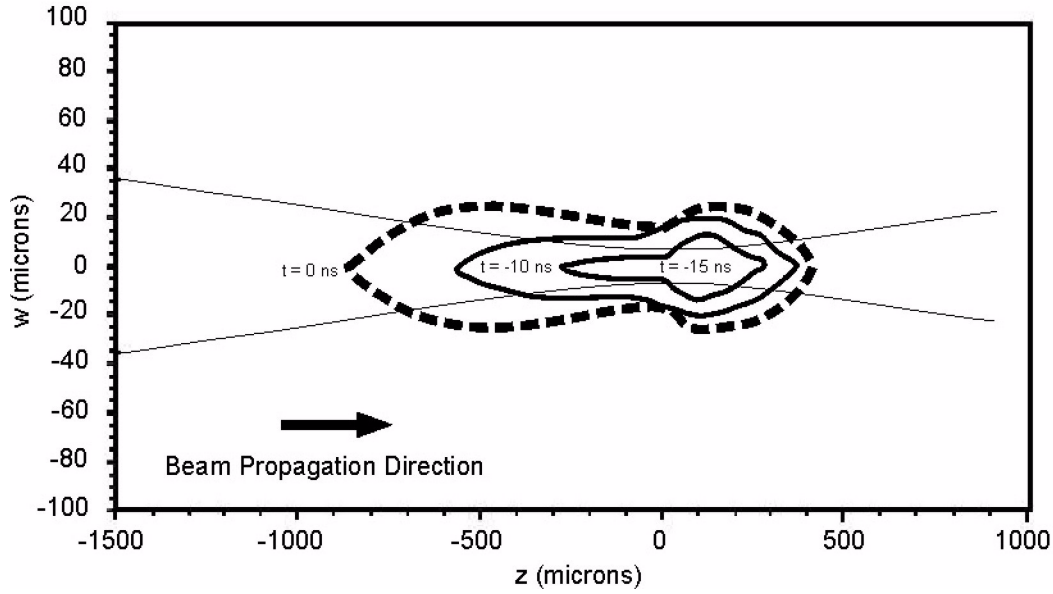


Fig.3.3 Temporal and spatial plasma evolution predicted by distributed shielding model of moving breakdown, which takes into the account spatial dependence of the absorption coefficient. The figure was reprinted from Kennedy [9].

$$\beta = P_{La0}/P_{bd} = I_{La0}/I_{bd} \quad (3.34)$$

is defined as a ratio between the maximal laser power and the power needed to produce the breakdown as introduced in Chapter 3.2.1. This kind of plasma modelling is known as the moving breakdown model. This model was modified by Docchio [7] to include the effect of plasma shielding. This version is known as the distributed shielding model of moving breakdown. The distributed shielding is expressed as a multiplicative function to the Gaussian temporal pulse shape, which takes into account a spatial dependence of the absorption coefficient. A temporal and spatial plasma evolution predicted by the moving breakdown as shown in Figure 3.3 is often visible during the bubble production by laser and can strongly influence the initial shape of the bubble.

3.3 Cavitation bubble dynamics

The complete analysis of the bubble dynamics represents a problem, which includes a solution of balance of mass, momentum, energy and entropy in space and time. In some cases there is a possibility of using simplifications, which can reduce the problem. The typical simplifications include:

- The assumption of a spherical bubble in an infinite body of liquid
- The bubble keeps its spherical shape while changing its radius
- The centre of the bubble is fixed in space and the bubble is stationary
- The bubble content is homogeneous
- The liquid surrounding the bubble is incompressible
- No heat and mass transfer are taken into account
- Gravity forces are neglected.

The application of these simplifications depends on the situation that needs to be solved, but they give the first insight into bubble dynamics. These simplifications, however, neglect some phenomena, which can be important in some cases. In real liquid the bubbles often associate into clouds and thus the simplification of a single bubble may not be satisfied. On the other hand bubble clouds can behave as a single bubble, however, in most cases they form structures that exhibit different behaviour. If the bubble is near a solid wall or a free boundary, the assumption of spherical symmetry can be disturbed. Especially, if the bubble collapses near a solid wall, its shape is strongly affected due to asymmetric pressure distribution around the bubble. In most cases the bubble moves in the liquid and thus also the assumption of the fixed centre is not satisfied. The temperature and pressure inside the bubble are not uniform within the bubble volume and the shock waves generated during the bubble collapse strongly influence their distribution inside the bubble. During collapse, the behaviour of a real bubble is perhaps most influenced by compressibility of the surrounding liquid. In numerical calculations a bubble collapsing in a compressible liquid shows one order lower collapse velocity than in an incompressible liquid. The mass transfer into the bubble volume can drive the bubble growth and influence the pressure inside the bubble. This effect was intensively studied theoretically e.g. by Zima [11]. In the case of laser-induced cavitation, evaporation of the surrounding liquid into the bubble increases the density of the bubble. Neglecting the gravity of the bubble content plays a significant role when the bubble stays in the liquid for a longer time. Gravitation forces cause an uplift of the bubble towards the free surface.

Currently there is a large number of physical and mathematical models derived e.g. by Gilmore [49], Brennen [16], Fujikawa [36] and others, which describe the bubble behaviour in a more complex way. The basic task in the bubble modelling is to determine the dependence of the bubble radius on time and describe the pressure, velocity and temperature fields in the bubble. If the spherical symmetry is not satisfied, it is necessary to estimate also the deformed shape of the bubble and its position in space.

3.3.1 Rayleigh-Plesset equation

Consider a spherical microbubble of radius R , containing gas and vapour, within an infinite body of liquid, as shown in Figure 3.4. The liquid has viscosity μ , surface tension σ and density ρ at temperature T_∞ and pressure p_∞ , where the infinity notation expresses values in undisturbed liquid. The bubble radius is considered sufficiently small for the difference in hydrostatic pressure to be negligible compared to the pressure difference corresponding to the surface tension. The values of physical properties of the liquid as viscosity, surface tension and compressibility are assumed to be constant and uniform. The behaviour of the radius R is of a primary interest in describing the bubble behaviour. The dynamics of such a bubble is described by Rayleigh-Plesset equation, which can be found e.g. in Brennen [16] as

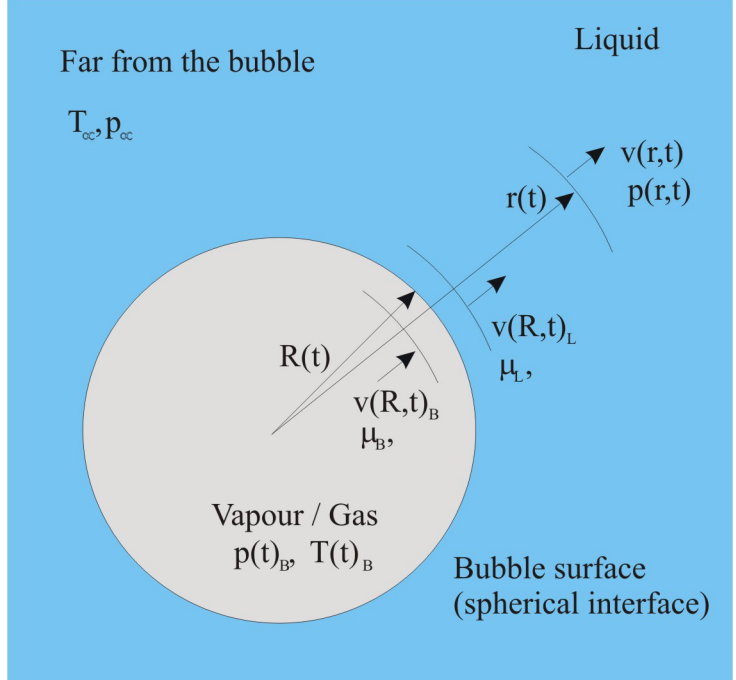


Fig.3.4 Bubble in the infinite field of liquid

The dynamics of such a bubble is described by Rayleigh-Plesset equation, which can be found e.g. in Brennen [16] as

$$\frac{p_B(t) - p_\infty(t)}{\rho} = R\ddot{R} + \frac{2}{3}\dot{R}^2 + \frac{2\sigma}{\rho R} + \frac{4\mu\dot{R}}{\rho R}, \quad (3.35)$$

where the term p_B represents homogeneous pressure of the bubble content at uniform temperature T_B . For a non-viscous liquid, the last term on the right-hand side vanishes. The corresponding equation is known as Rayleigh's equation. The differential equation (3.35) is nonlinear, due to the inertial term and in most cases can be solved only numerically. The initial conditions are usually based on a known initial bubble radius R_0 and a bubble velocity $\dot{R}(0)$ at the time $t = 0$. Substituting this condition into (3.35) yields

$$p(0)_B = p(0)_\infty + \frac{2\sigma}{R_0}. \quad (3.36)$$

The pressure $p(0)_B$ denotes the ambient pressure of the liquid exerted on the bubble in the initial state. In general, the bubble can contain vapour or gas or a mixture of both at temperature T_B (temperature inside the bubble). If there is no mass transfer from the liquid the pressure inside the bubble can be expressed as

$$p(t)_B = p_v(T_B) + p_g(t). \quad (3.37)$$

The gas (or a mixture of gases) inside the bubble is treated as non-condensable (inert) and not experiencing phase transition. If the mixture of gases satisfies the Dalton's law, the pressure of the gas can be expressed as a sum of partial pressures. If all the gasses satisfy the perfect-gas condition, also the sum can be considered as an ideal gas. Most often, the gas is believed to obey the polytropic behaviour

$$p(t)_G \left(\frac{4}{3} \pi R^3 \right)^\gamma = p(0)_G \left(\frac{4}{3} \pi R_0^3 \right)^\gamma, \quad (3.38)$$

where the polytropic exponent of the gas γ is supposed to be constant. The difference between the temperature of bubble content T_B and the temperature of the surrounding liquid is usually insignificant T_∞ , however in the case of the laser-induced bubble this difference can play an important role and influence the bubble dynamics. To obtain the temperature one has to solve heat and mass transfer between the bubble content and the surrounding liquid coupled into a set of equations. There are some analytical approximations valid for some particular cases as the ones derived by Plesset [19]. However, it is often necessary to solve the problem numerically. After all the above assumptions are combined they lead to the expression for the pressure inside the bubble

$$p(t)_B = p_v(T_\infty) + p_{G0} \left(\frac{R_0}{R} \right)^{3\gamma}. \quad (3.39)$$

If this term is introduced into Eq. (3.37) the corresponding boundary condition for the time $t=0$ is

$$p_v(T_\infty) + p(0)_B = p(0)_\infty + \frac{2\sigma}{R_0}. \quad (3.40)$$

The mass of gas trapped in the bubble is therefore

$$m_g = \frac{4}{3} \pi R_0^3 \frac{p_{g0}}{R_g T_B} = \text{const}. \quad (3.41)$$

3.3.2 Bubble stability

Although the Rayleigh-Plesset equation is only a first approximation of the bubble dynamics, its analysis can be used for explanation of some basic modes of bubble behaviour. The solution of the Rayleigh-Plesset equation strongly depends on the initial conditions, namely on the partial pressure of gas inside the bubble p_{g0} and the pressure in the surrounding liquid p_∞ . The reason is found in the stability of the equilibrium state. To perform this analysis a small perturbation of the bubble radius has to be introduced as

$$R = R_0(1 + \delta R), \quad (3.42)$$

where $\delta R \ll R$. Substitution of Eq. (3.42) into the Rayleigh-Plesset equation (3.33) results in

$$\frac{\delta R}{\rho} \left[\frac{2\sigma}{R_0} - 3\gamma p_{G0} \right] = RR + \frac{2}{3} \dot{R}^2 + \frac{4\mu \dot{R}}{\rho R}. \quad (3.43)$$

Note: Let us have a bubble, originally in equilibrium, which is subjected to an accidental perturbation of the bubble radius. If this perturbation decreases, the equilibrium is called stable equilibrium. On the contrary, if the perturbation increases the equilibrium is called unstable equilibrium.

Supposing that R_0 , R , σ , μ , ρ are all positive, the sign of the perturbation must be opposite to the sign of \dot{R} and \ddot{R} to satisfy the stability condition of the equation. To ensure that, the expression in the brackets on the left-hand side of Eq. (3.43) must be negative. This leads to the stability condition in the form

$$p_{G0} > \frac{2\sigma}{3nR_0} = p_{Gcrit}, \quad (3.44)$$

which introduces the critical value of gas pressure p_{Gcrit} . The inequality (3.44) has the following meaning. For a given mass, if the pressure $p_{G0} < p_{Gcrit}$ the bubble equilibrium is unstable. This directly implies that any vapour bubble for which $p_{G0} = 0$ must always be unstable. If such a bubble is subjected to decrease in pressure in the surrounding liquid the bubble will grow explosively, unless the pressure is increased up to some higher value. If the gas pressure inside the bubble is $p_{G0} > p_{Gcrit}$, the bubble will be brought back to equilibrium after a pressure change. To make the situation clearer it is appropriate to illustrate graphically the dependence of the equilibrium pressure in the liquid at the equilibrium bubble radius according to Eq. (3.40) as shown in Figure 3.5. In this analysis, two stability criteria were introduced by Blake [12]. The critical bubble size, R_{crit} , which for an isothermal case has the form

$$R_{crit} = \frac{9m_g T_B R \gamma}{8\pi \sigma}. \quad (3.45)$$

and the equilibrium liquid pressure $p_{\infty crit}$, the value of which can be obtained by imposing the value of R_{crit} into Eq. (3.40). The solid lines in Figure 3.5 represent the dependence of the critical bubble radius on the critical liquid pressure for a different amount of gas trapped inside the bubble and the dotted lines separate the regions of equilibrium and non-equilibrium states. The stability condition can be formulated as $(p_v - p_\infty) / \partial R < 0$. According to this condition the left branch of the curve corresponds to the equilibrium region. Since the bubble radius at this branch of the curve is close to the initial bubble radius, the gas pressure inside the bubble is higher than the vapour pressure, which is constant at a constant temperature. After some accidental increase of

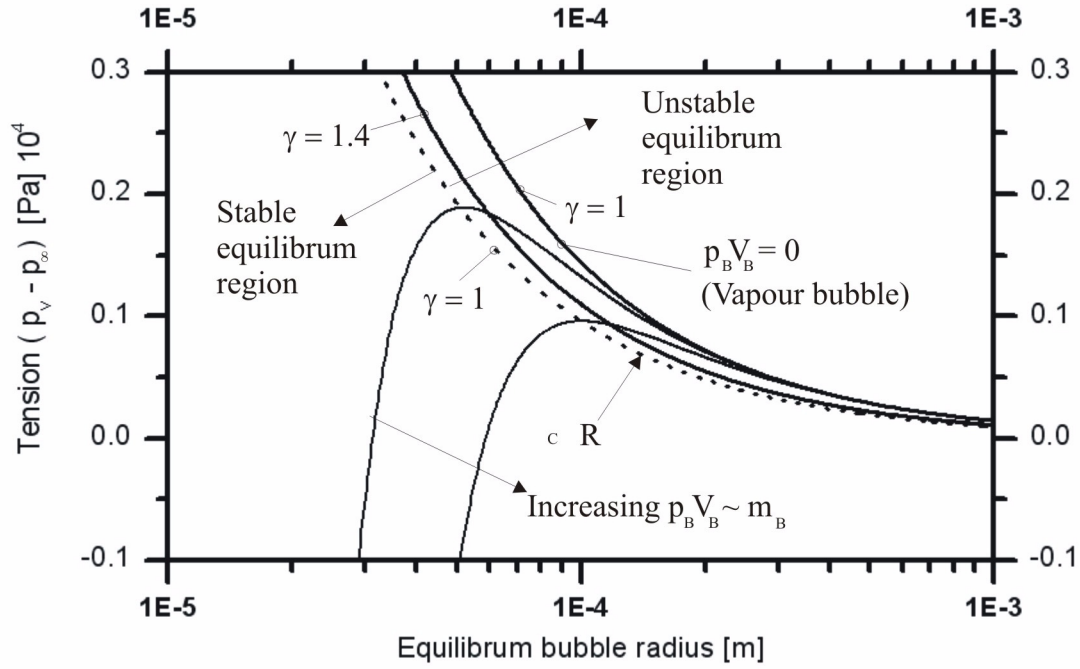


Fig.3.5 Equilibrium bubble pressure in dependence on the equilibrium bubble radius.

the bubble radius the pressure inside the bubble decreases inversely proportional to the cubic power of R , according to Eq. (3.39), i.e. faster than the capillary pressure, which decreases inversely proportional to the first power of R . The capillary pressure causes the return of the bubble into the equilibrium state. If the equilibrium bubble radius corresponds to the right branch of the curve the gas pressure is much lower than the vapour pressure. After some accidental increase of the bubble radius, the pressure inside the bubble changes only slightly and the capillary pressure, which could return the bubble to equilibrium, decreases and the bubble grows without limits. At the both branches of the curve any accidental decrease of the bubble radius causes its return to the critical value R_{crit} .

Note that the equilibrium in the previous paragraph is static equilibrium. To investigate the dynamic equilibrium, one has to examine Eq. (3.35). The equation can be written in the form

$$\dot{R}^2 = \frac{2p_v - p_\infty}{3} \frac{1}{\rho} \left[1 - \frac{R_0^3}{R^3} \right] + \frac{2}{3(\gamma+1)} \frac{p_{G0} R_0^3}{\rho R^3} \left[1 - \left(\frac{R}{R_0} \right)^{3(\gamma-1)} \right] - \frac{2\sigma}{\rho R} \left[1 - \frac{R_0^2}{R^2} \right], \quad (3.46)$$

if the pressure in the surrounding liquid is constant and its viscosity is neglected. The function (3.36) has the form $(dR/dt)^2 = f(R)$, which is frequently used in the solid body mechanics. The basis of the analysis is the existence of the roots of the equation, which determine the limits of the variation of the radius R . The equilibrium case, for which $p_\infty = p_{\infty 0}$, is the equilibrium condition

equivalent to the static equilibrium condition treated above, except that the additional conditions $\dot{R}_0 = 0$ and $\ddot{R}_0 = 0$ have to be valid. In the case of bubble growth, where $p_\infty < p_{\infty 0}$ the following situations have to be considered

- If the equation $f(R)$ has one root R_I larger than R_0 the bubble radius oscillates between the two values $R=R_I$ and $R=R_0$. The character of the oscillation strongly depends on the ratio of R_0 and R_I . If the ratio is large, the gas pressure inside the bubble has only a small influence on the bubble behaviour. The oscillations are sequences of successive expansions and compressions. If the root R_I is close to the initial radius R_0 , the behaviour is influenced by the gas pressure inside the bubble. The motion becomes harmonic with the oscillation frequency

$$f_0 = \frac{1}{2\pi R_0} \sqrt{\frac{1}{\rho_0} \left[3\gamma p_{G0} - \frac{2\sigma}{R_0} \right]}. \quad (3.47)$$

- If the equation $f(R)$ has no root larger than R_0 , the bubble grows without limits. The velocity of the growth tends to the value, which could be obtained from Eq. (3.46), where the bubble radius takes an infinite value as

$$\dot{R}_{max}^2 = \frac{2p_v - p_\infty}{3\rho}. \quad (3.48)$$

This equation is in good agreement with experimental measurements. The matter is complicated when a periodically changing pressure field in the liquid is considered. However, this situation is not of our interest and will not be considered here.

3.3.3 Bubble collapse

Consider a collapse of a spherical vapour bubble in non-viscous incompressible liquid. Before the collapse initiation, the bubble is supposed to be in equilibrium under liquid pressure $p_{\infty 0}$, which has to be equal to the vapour pressure p_v inside the bubble according to Eq. (3.40). At a time $t > t_0$ the pressure $p_\infty > p_{\infty 0}$ is applied to the liquid. It results in the bubble collapse in a characteristic time τ called the Rayleigh time. Neglecting the surface tension term, the Rayleigh - Plesset equation (3.35) can be integrated to give

$$\frac{dR}{dt} = - \sqrt{\frac{2}{3} \cdot \frac{p_\infty - p_v}{\rho} \cdot \left[\frac{R_0^3}{R^3} - 1 \right]}. \quad (3.49)$$

Note that at the bubble collapse ($R = 0$) the bubble wall tends to accelerate without limits, which is impossible in real fluids. However, the result shows that the bubble implosion occurs in a very short time. The time required for the bubble to collapse to $R = 0$, can be obtained from Eq. (3.49) after separation of variables

$$\tau_{Ra} = \sqrt{\frac{2}{3}} \cdot \frac{p_{\infty} - p_v}{\rho} \cdot \int_0^{R_0} \frac{1}{\sqrt{\frac{R_0^3}{R^3} - 1}} dR \cong 0,915 \cdot R_0 \cdot \sqrt{\frac{\rho}{p_{\infty} - p_v}} \quad (3.50)$$

The constant 0.915 is the approximate value of

$$\sqrt{\frac{\pi}{6}} \cdot \frac{\Gamma(5/6)}{\Gamma(4/3)}, \quad (3.51)$$

where Γ is the factorial Gamma function. The value of τ_{Ra} is in good agreement with the experimental values in a wide range of initial conditions. This equation was first obtained by Rayleigh.

3.3.4 Dynamics of cavitation bubble in compressible liquid

In real liquids the bubble dynamics is mostly influenced by the liquid compressibility, which plays the dominant role during the violent bubble collapse or explosive bubble growth. The liquid compressibility causes the decrease of the bubble wall velocity during the calculations and therefore can be considered as damping. The liquid compressibility is closely associated with the quantity

$$c^2 = \left(\frac{dp}{d\rho} \right)_s, \quad (3.52)$$

called speed of sound, which characterizes the velocity of propagation of density and pressure changes. In the late works by Rayleigh [35] the liquid was treated as incompressible. The first author who probably introduced the liquid compressibility into the bubble dynamics was Herring [13], who assumed a constant value of speed of sound in the liquid. His work was followed by Trilling [14], who investigated the pressure and velocity field around a collapsing bubble. Both of these approximations are suitable in the cases where the liquid velocity is much smaller than the speed of sound in the liquid. In the latter works, which dealt with underwater explosions, Kirkwood and Bethe [39] introduced the speed of sound depending on the pressure in the medium. Their work was used for the investigation of pressure and velocity field around a cavitation bubble by Gilmore [49], who also derived several analytical formulas useful for the calculation of the cavitation bubble dynamics in compressible liquid. In the following paragraph some models regarding the influence of compressibility effect are introduced.

The model introduced by Herring [13], who proposes the liquid velocity at the bubble surface to be slower in comparison to c_0 constant speed of sound in the liquid, has the following form

$$R \left(1 - \frac{2\dot{R}}{c_0} \right) \frac{d\dot{R}}{dt} + \frac{2}{3} \left(1 - \frac{4\dot{R}}{3c_0} \right) \left(\frac{dR}{dt} \right)^2 = \frac{R\dot{R}}{\rho c_0} \left(1 - \frac{\dot{R}}{c_0} \right) \frac{dp_R}{dR} + \frac{p_R - p_{\infty}}{\rho_{\infty}}. \quad (3.53)$$

The pressure p_R at the bubble wall can be obtained from the momentum balance (A.5) as

$$p_R = p_B - \frac{2\sigma}{R} + \frac{4\mu dR}{R dt}. \quad (3.54)$$

It is obvious that the Rayleigh-Plesset equation defined by Eq. (3.35) is only a special form of Eq. (3.53), where the speed of sound has (theoretically) infinite value. If the pressure difference between the liquid and the bubble content is constant and the liquid viscosity and the surface tension are neglected Eq. (3.53) can be solved analytically to give an implosion velocity of the bubble wall as it was first introduced by Flinn [50]

$$\dot{R}^2 = \frac{2p_\infty - p_v}{3\rho_L} \left(\frac{R_0^3}{R^3} - 1 \right) \left(1 - \frac{4\dot{R}}{3c_0} \right). \quad (3.55)$$

Note that this equation can be reduced to Eq. (3.49). Gilmore [49] derived the equation describing the dynamics of the cavitation bubble in a compressible liquid for arbitrary velocity based on the so-called Kirkwood-Bethe hypothesis. The authors supposed that the bubble interface was propagated from the source with a velocity, which was the sum of the local speed of sound c depending on the pressure and the particle velocity u . The expression was first introduced by Gilmore [49] and has the following form

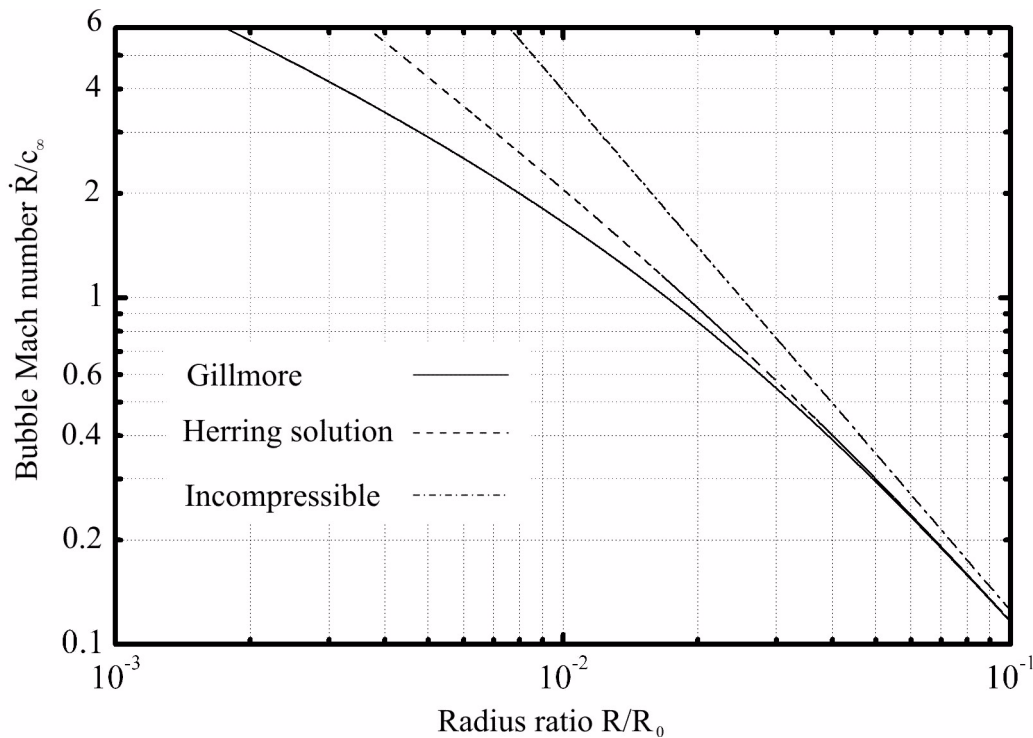


Fig.3.6 Velocity reached by the bubble wall during the bubble wall collapse.

$$R\left(1 - \frac{\dot{R}}{c}\right)\frac{d\dot{R}}{dt} + \frac{2}{3}\left(1 - \frac{\dot{R}}{4c}\right)\left(\frac{dR}{dt}\right)^2 = H\left(1 - \frac{\dot{R}}{c}\right)\frac{dp_R}{dR} + \frac{R}{c}\left(1 - \frac{\dot{R}}{c}\right)\dot{R}\frac{dH}{dR}. \quad (3.56)$$

The quantity H representing the undissipated enthalpy is defined by the integral

$$H = \int_{p_\infty}^{p_R} \frac{dp}{\rho}, \quad (3.57)$$

which has to be supplemented by an appropriate equation of state. The comparisons of models of bubble dynamics, which use different approximations of liquid compressibility are shown in Figure 3.6. From the figure it is obvious that the model based on the Kirkwood-Bethe theory embodies lower collapse velocities. From the comparison with the experimental data published by Gilmore [49], the model shows the best agreement with the measurements. As the Gilmore's model is of the most interest in this work, a summary of conclusions obtained by Gilmore during the detail analysis of the model is presented. From the analysis it follows that the model based on the hypothesis is accurate in the range of small wavelengths and arbitrary velocities, as well as for the small velocities and arbitrary wavelengths. From the analysis of the equation it also follows that the model is less accurate when the local velocity of the bubble motion is close to the sound velocity, where the terms in parentheses \dot{R}/C become large. The comparison of Gilmore's model (3.56) and Herring's model (3.53) reveals that the first model is accurate up to the second order of \dot{R}/C , whereas the second model is accurate up to the first order of \dot{R}/C only. For the case of the bubble collapsing under the constant pressure Gilmore shows that the magnitude of the bubble wall velocity increases monotonously as the radius decreases and becomes infinite at $R \rightarrow 0$. For small radiuses and high velocities \dot{R} behaves according to $R^{-1/2}$ in the Gilmore's modification whilst it behaves according to $R^{-3/2}$ for the incompressible case.

3.3.5 Influence of viscosity and surface tension on bubble dynamics

The influence of viscosity and surface tension on the bubble dynamics was first studied by Poritsky [27]. In order to investigate the effects, the author introduces the non-dimensional time τ , radius R' , viscosity μ' and surface tension σ' into the Rayleigh-Plesset equation as follows:

$$\tau' = \frac{t}{R_0} \left(\frac{p_\infty - p_v}{\rho} \right)^{\frac{1}{2}}, R' = \frac{R}{R_0}, \quad (3.58)$$

$$\mu' = \frac{4\mu}{R_0[\rho(p_\infty - p_v)]^{1/2}}, \sigma' = \frac{\sigma}{R_0(p_\infty - p_v)}. \quad (3.59)$$

Note that the equations are only valid for the bubble collapse; for the expansion the argument $p_\infty - p_v$ has to be replaced by $p_v - p_\infty$. The results obtained from the solution of the Rayleigh-

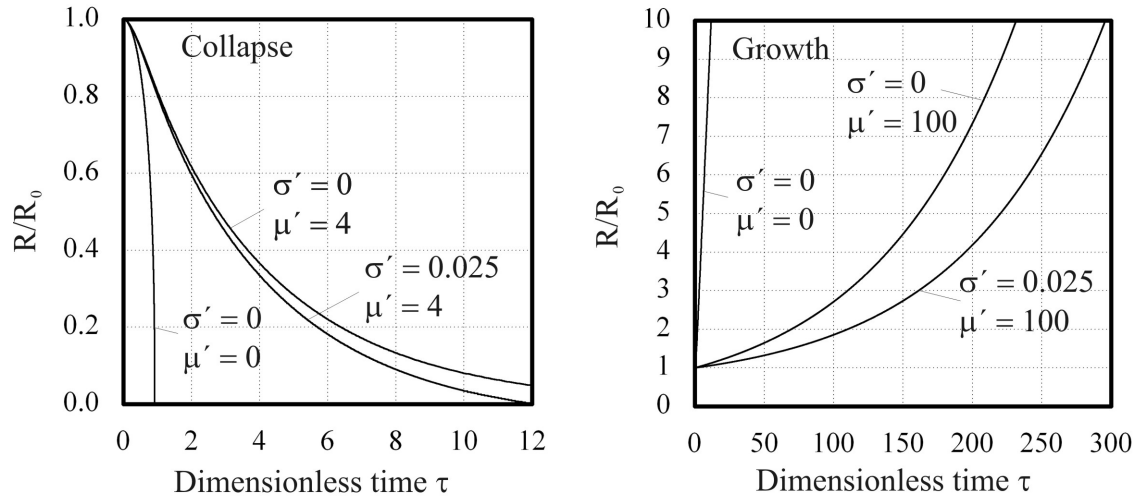


Fig.3.7 Influence of viscosity and surface tension on cavitation bubble dynamics.

Plesset equation for different parameters of non-dimensional viscosity and surface tension during the bubble collapse and expansion are plotted in Figure 3.7. The initial bubble radius and the pressure difference in the case of the bubble collapse were 10^{-7} m and 10^7 Pa and for the bubble growth they were 10^{-8} m and 1.6×10^6 Pa. From the comparison of ideal liquid and the viscous one it is evident that the viscosity lowers the collapse velocity. For the value of viscosity $\mu' = 4$ the collapse time increases to an infinitesimal value, which is in contrast with the case of the Rayleigh collapse. The author presents the critical value of $\mu' = 0.46$, which is the boundary between the ultimate and infinitesimal collapse time. From the figures it is also visible that the surface tension increases the collapse velocity, but decreases the growth velocity in the case of expansion..

The possibility of neglecting the surface tension and the viscosity effect were also discussed in Gilmore's work. The author shows that during the first part of the collapse, the surface tension effects are stronger than the viscous effects, while during the later part of the collapse the viscous effects predominate. Gilmore [49] also shows that the collective effect of viscosity and the liquid compressibility is negligible.

3.3.6 Dynamics of non-spherical bubble

As mentioned at the beginning of this chapter, the condition of spherical symmetry assumed in the derivations is not fulfilled in some situations. The spherical shape of the bubble is disturbed especially when the bubble collapses near a wall or free surface. The deformation is caused by the difference in the pressure distribution along the bubble axis. This chapter introduces the approaches used in the investigation of the bubble behaviour in those cases. The first approach used for the calculation of the deformed bubble surface (e.g. by Birkhoff [2] or Plesset [20]) is focused on the investigation of the stability of the spherical surface. This analysis essentially examines a spherical equivalent of the Rayleigh-Taylor instability, which requires the acceleration to be directed from the heaviest to the lightest fluid. The theory determines the conditions for

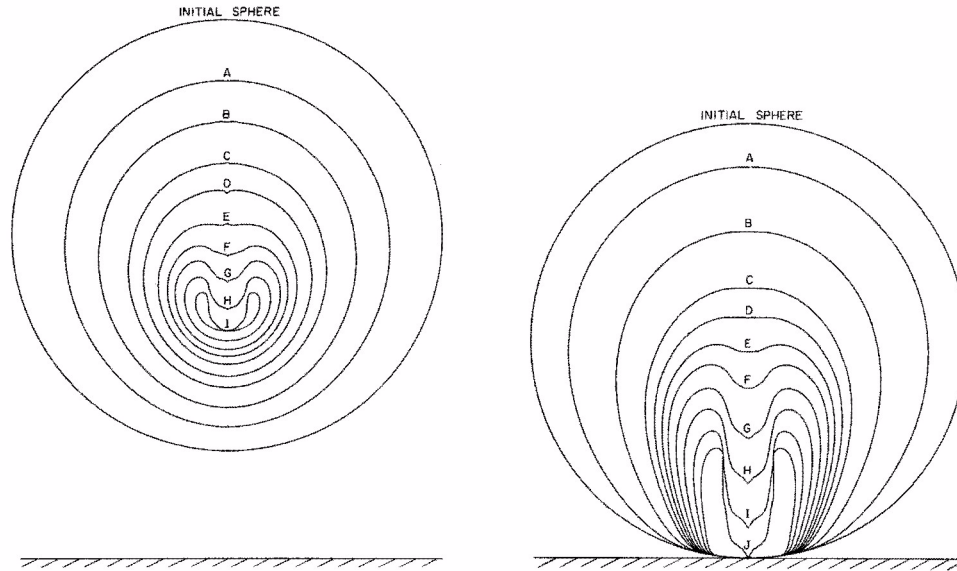


Fig.3.8 Deformation of the bubble interface (Reprinted from an article published by Plesset [30]).

which the bubble is stable or unstable, however, it does not describe the shape of the boundary. The analysis investigates the stability of the spherical boundary between two inviscid and incompressible liquids with densities ρ_1 and ρ_2 , respectively. The results of the analysis, which can be found in detail in Noskievič [18], can be summarized as follows: The movement of the interface between the liquids can be assumed as stable if the interface will increase in time and unstable if the interface will decrease in time. The linear theory of stability shows that during the implosion the bubble will be stable if the bubble radius will not differ much from the initial bubble radius. It means that in the case of a vapour bubble with a small fraction of gas the bubble radius could reach a relatively small value, the surface instability becomes evident and the bubble can break up into smaller bubbles. In the case of a gas bubble, where the pressure of gas is much higher than the vapour pressure, its presence could prevent the decrease of the bubble at a smaller value and the interface will remain stable.

One of the most popular approaches, which already includes calculation of the deformed bubble interface, was derived by Plesset and Chapman [30]. The authors proposed a collapse of an initially spherical bubble of the radius R_0 under a constant pressure difference. The surface tension, viscosity and liquid compressibility are neglected in the calculation. The simulation proceeds in a series of small time steps, during which the static velocity potential is calculated. As the liquid is incompressible, the potential is calculated using the Laplace equation with the boundary conditions at the bubble wall, at the solid wall and in the free liquid. The velocity of the particles on the bubble wall is calculated from the velocity potential using the equation $v_i = d\phi/dx_i$. As the velocity of the bubble particles is known at the time t , the new position of the bubble interface particles can be deduced assuming that the particles move with that velocity. Then the new value of the velocity potential at the bubble wall can be calculated from the equation

$$\frac{d\phi}{dt} = \frac{\partial\phi}{\partial t} + v_i \frac{\partial\phi}{\partial x_i} = \frac{p_\infty - p_v}{\rho} + \frac{v^2}{2}. \quad (3.60)$$

The new value of the velocity potential at the bubble surface in its new position is then used as the updated boundary condition for the calculation of the velocity potential in the whole region and the process is repeated. The most suitable method for the calculation of the potential field is the boundary integral method used by Toose [28] or Cunha [29]. The method reduces, with the help of the Green theorem, the calculation in the whole region of interest only to the calculation at its boundaries. Some results obtained from the Chapman-Plesset analysis are presented in Figure 3.8. The figures show the bubble compression at two distances from the solid wall. In both cases the jet against the boundary is produced, while a hollow of high curvature is occurring at the opposite side. The effects of surface tension, viscosity and compressibility, which were neglected in the above solution, were introduced into the method by Blake [31], however, the additional terms make the calculation of the velocity potential most tedious.

The last principle presented here uses the concept of the Kelvin impulse. The principle was developed in the framework of the potential flow and was first used by Benjamin and Ellis [33] and then extended by Blake [32]. The principle only gives information about the bubble jet and its direction. In the method presented above the velocity potential has to be calculated in each time step. In the Kelvin impulse concept the bubble represents a point source in potential flow. The velocity potential is computed only once and can be used for any similar configuration. The disadvantage of the method is that the information about the bubble shape is lost.

3.4 Theory of shock waves

The pressure distribution in the liquid around the collapsing bubble was already studied in the first work of Rayleigh [35]. However, the shock waves associated with the cavitation bubble growth and collapse were more frequently investigated during the Second World War especially in connection with underwater explosions. The main theory for this purpose was developed by Kirkwood and Bethe [39], Penney and Pike [38] and Brinkley and Kirkwood [40], which is summarized in Cole [41]. However, the first authors who investigated the pressure distribution in the liquid surrounding the cavitation bubble were Hickling and Plesset [37]. They used a modified method of characteristics to obtain the pressure profiles in the liquid around the collapsing bubble, however, due to a numeric instability they had stopped the calculation before the shock wave had developed. A more complex approach than the one done by Hickling and Plesset [37], was applied by Fujikawa and Akamatsu [36], who introduced the effects of condensation and evaporation into the calculations. The latest work dedicated to the shock wave produced by the optical breakdown in liquids was done by Vogel [23]. The following chapters include some important formulas and equations used for the calculation of the propagation of the spherical wave in the liquid.

The simplest form of the spherical wave is one whose parameters are a function of the radial distance r . The motion of such a wave can be described by Eqs. (A.8) and (A.10), which provides

the relation between velocity and pressure in the liquid. If viscosity and heat conduction can be neglected the density is only a function of the pressure and can be determined from the equation of state. For small amplitudes Eqs. (A.8) and (A.10) can be simplified into the following form

$$\frac{1}{\rho c_0^2} \frac{\partial p}{\partial t} = -\frac{1}{r^2} \frac{1}{\partial r} \left(r^2 \frac{\partial v}{\partial t} \right), \quad (3.61)$$

$$\rho_0 \frac{\partial v}{\partial t} = -\frac{\partial p}{\partial r}, \quad (3.62)$$

where the speed of sound c_0 is introduced by Eq. (3.52). If the second equation is differentiated with respect to t and the particle velocity v is eliminated by the first equation, a one-dimensional form of the wave equation for a spherical wave is obtained

$$\frac{1}{c_0^2} \frac{\partial^2 p}{\partial t^2} = \frac{1}{r^2} \frac{1}{\partial r} \left(r^2 \frac{\partial p}{\partial r} \right). \quad (3.63)$$

The solution of the above equation is any function in the form

$$p - p_0 = \frac{1}{r} f \left(t - \frac{r}{c_0} \right). \quad (3.64)$$

The negative sign corresponds to an outgoing wave. As the velocity c_0 is constant, the shape of the wave is unchanged but its amplitude diminishes with the increasing r . If the solution of Eq. (3.64) is introduced into Eq. (3.63), the expression for $v(r)$ is obtained as

$$\frac{\partial v}{\partial t} = \frac{1}{\rho_0 c_0} \frac{1}{r} f' \left(t - \frac{r}{c_0} \right) + \frac{1}{\rho_0 r^2} f' \left(t - \frac{r}{c_0} \right). \quad (3.65)$$

Eq. (3.65) can be integrated at the constant position in order to obtain the explicit expression for $v(r)$

$$v(t) - v(t_0) = \frac{p - p_0}{\rho_0 c_0} + \frac{1}{\rho_0 r} \int_{t_0}^t (p(r, t') - p_0) dt'. \quad (3.66)$$

The first term on the right side of Eq. (3.66) represents the velocity for plane wave and the second term represents the so-called *afterflow*. The meaning of the term afterflow can be explained using the following considerations. If the time t_0 is chosen before the shock wave reaches the position r , it is obvious that the pressure at the time t is influenced by the pressure changes given by the integral in the fluid before the wave reaches the position. This can be made more explicitly by consid-

3.4 CURRENT STATE OF KNOWLEDGE - THEORY OF SHOCK WAVES

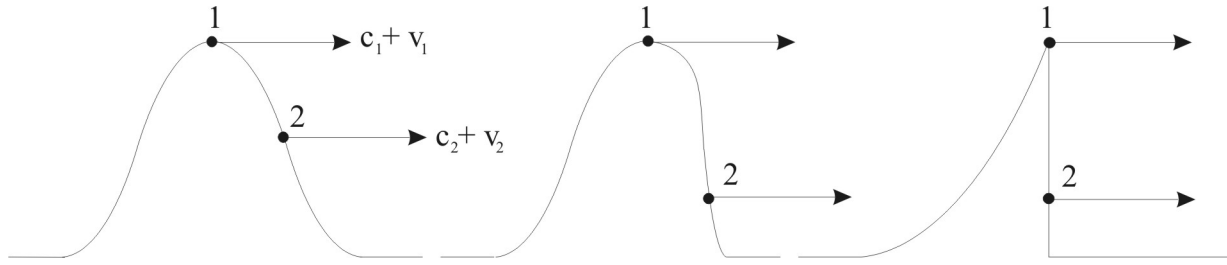


Fig.3.9 Development of a shock wave.

eriving the relation between the pressure at any point in the fluid and at the bubble of radius R . If the pressures are expressed from Eq. (3.64), the following expression is obtained:

$$p - p_0 = \frac{R}{r} \left[p \left(R, t - \frac{r-R}{c_0} \right) - p_0 \right]. \quad (3.67)$$

The pressure at any point in the liquid is thus determined by the pressure at the radius R at time

$$\frac{R-r}{c_0}. \quad (3.68)$$

earlier. This time is the time required for the pressure to be transmitted from R to r .

The approximations used above are valid only for small variations of the density and pressure. It has been assumed that the velocity c_0 used in the equations could be treated as a constant independent of the pressure. This assumption means that any part of the disturbance is propagated with the velocity c_0 . If the velocity $c = \sqrt{dp/d\rho}$ is assumed variable with the density, the matter becomes more complicated. Note that for any normal fluid the speed of sound c increases with increasing compression. Suppose that a plane wave is advancing from left to right, which at some instant has a shape according to Figure 3.9. The wave will travel with the velocity c relative to the fluid, the particles of which move with the velocity v . At position 1 the velocity with respect to the fixed coordinate system is $c_1 + v_1$ and at position 2 the velocity is $c_2 + v_2$. If the pressure is higher at position 1 than at position 2, the particle velocity and the speed of sound will be higher at position 1 than at position 2. At a later time the region of higher pressure will approach the regions of lower pressure upstream. This will result in a very steep wave, which is known as a shock wave. It has been proved experimentally that waves of this kind are so steep as to be virtually discontinuous. The wave for which position 1 is propagated with a lower velocity than at position 2 is called rarefaction wave. When the discontinuity (shock wave) occurs, the temperature and the pressure of the adjacent elements of fluid are very different and a large amount of energy is dissipated as heat. Although these considerations were made for a plane wave, they are valid also for the spherical wave, except that the amplitude will be weakened with the increasing r . The relations between the possible stages ahead and behind the shock wave are given by Rankine-Hugoniot curve (Figure 3.9 - right). The equations applicable to such discontinuity were originally devel-

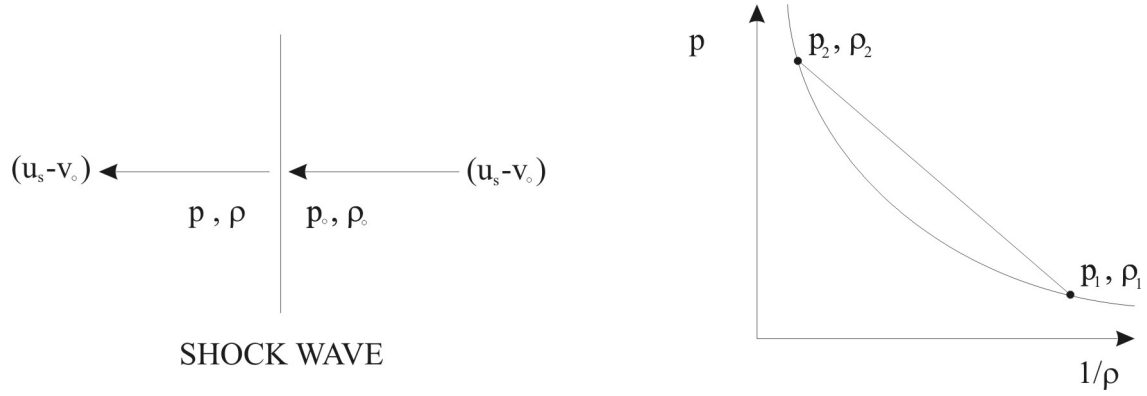


Fig.3.10 Conditions at the shock front (Left) and a typical Rankine-Hugoniot curve (Right)

oped by the Rankine and Hugoniot and are easily obtained from the balance Eqs. (3.10), (3.15) and (3.20) by considering regions close ahead and behind the discontinuity according to Figure 3.10. If an observer moves with the velocity u_s of the shock wave into a region with the particle velocity v_0 and density ρ_0 , the apparent velocity of the fluid towards him is $u_s - v_0$ and the velocity leaving the front is $-(u_s - v)$, where v is the particle velocity in the fixed coordinate frame. The expression of conservation of mass (3.10) at the shock front can be written as

$$\rho_0(u_s - v_0) = \rho(u_s - v). \quad (3.69)$$

The conservation of momentum (3.15) of the flow into and out of the shock wave has the form

$$\rho_0(u_s - v_0)(v - v_0) = p_s - p_0, \quad (3.70)$$

where the difference $p_s - p_0$ represents the impulse of the net forces per unit area, which compensates the change in momentum. The conservation of energy (3.20) at the discontinuity requires that the work done by the pressures is equal to the increase of the potential and kinetic energy:

$$p_s v - p_0 v_0 = \rho_0(u_s - v_0) \left[\varepsilon - \varepsilon_0 + \frac{1}{2}(v^2 - v_0^2) \right]. \quad (3.71)$$

The wave usually propagates into a region of undisturbed fluid where $v_0 = 0$. Using this simplification and after some rearrangement, the Rankine-Hugoniot relations can be obtained in a more convenient form

$$\rho_0 u_s = \rho(u_s - v), \quad (3.72)$$

$$\rho_0 u_s v = p_s - p_0, \quad (3.73)$$

3.4 CURRENT STATE OF KNOWLEDGE - THEORY OF SHOCK WAVES

$$\varepsilon - \varepsilon_0 = \frac{1}{2}(p_s + p_0)\left(\frac{1}{\rho} - \frac{1}{\rho_0}\right). \quad (3.74)$$

Equation (3.71) is usually transformed using the enthalpy definition $h = \varepsilon + p_0\Delta(1/\rho)$ into

$$\Delta h_s = \frac{p}{2}\left(\frac{1}{\rho} + \frac{1}{\rho_0}\right), \quad (3.75)$$

where Δh_s is the specific enthalpy increment experienced by the fluid in traversing the shock wave. Note that Eqs. (3.72) and (3.73) can also be obtained from the balance equations given in Appendix A.

The solution of the shock wave propagation in the case of finite amplitudes is complicated and it is not possible to obtain an analytical solution in the spherical case because of the divergent term $1/r$. The first group of methods is based on the transformation of the system of Eqs. (A.8) and (A.10). One approximation called the Riemann treatment introduces a new variable

$$\sigma = \int_{\rho_0}^{\rho} \frac{c(\rho)}{\rho} d\rho, \quad (3.76)$$

into the equations, which allows the transformation of the system into the form

$$\frac{\partial}{\partial t}(\sigma \pm v) \pm (\sigma \pm v) \frac{\partial}{\partial t}((\sigma \pm v)) = -\frac{2cv}{r}, \quad (3.77)$$

suitable for numerical integration using appropriate boundary conditions. The method was used by Penney [38] to calculate propagation of the shock wave produced by the TNT charge explosion. The author used the solution to determine the equation for the peak pressure propagated along the position r_s as

$$p_s = G \frac{R_0}{r_s} e^{\frac{2R_0}{r_s}}, \quad (3.78)$$

where G is the constant characterizing the source and R_0 is the initial radius of the source.

Somewhat more analytical solution than the one given by Riemann was given by Kirkwood and Bethe [39]. The authors solved the fundamental equations by introducing the new quantity

$$Y = h + \frac{1}{2}v^2 \quad (3.79)$$

called kinetic enthalpy. If this quantity is introduced into the continuity (A.8) and momentum (A.10) equations and irrotational flow is considered, the second equation gives

$$rY = \frac{\partial \phi}{\partial t}, \quad (3.80)$$

where ϕ is the velocity potential and the first equation can be written as

$$\frac{\partial^2 \phi}{\partial r^2} - \frac{1}{c^2} \frac{\partial^2 \phi}{\partial t^2} = \frac{1}{c^2} \left[v \frac{\partial v^2}{\partial r} - \frac{\partial v^2}{\partial t} \right]. \quad (3.81)$$

Note that the equations were evaluated in the spherical coordinates and the solution in the form $\phi = \phi/r$ was assumed. The basics of the analysis is the evaluation of the function $rY(r,t)$ from the boundary conditions at the gas sphere (bubble). The authors shows that Eq. (3.81) for $c = \infty$ (incompressible liquid) results in infinite velocity of propagation of $rY(r,t)$. In case of the constant speed of sound in the liquid the equation gives $rY(r,t) = f(t-r/c_0)$, which is the well-known equation for the propagation of the sound wave. Using this basis, the authors assumed that in the case of a finite amplitude the shock wave could propagate with a variable velocity

$$\bar{c} = \left(\frac{\partial r}{\partial t} \right)_{rY = \text{const}}. \quad (3.82)$$

Eq. (3.82) is the most important equation introduced in the Kirkwood-Bethe theory, but in fact it represents only a modified method of characteristics, which is often used in hydrodynamics. Based on the equation the authors showed that the relation between the kinetic enthalpy at the position r related to the value at the bubble surface R is

$$Y(r, t) = \frac{R(\tau)}{r(t)} Y(R, \tau). \quad (3.83)$$

The main problem of the method is to determine the function $Y(R, \tau)$ at the bubble wall.

Both solutions presented above were evaluated at constant entropy, which finally gives a conclusion that the shock wave propagates without any dissipative processes and only the amplitude of the wave decreases with the increasing shock wave position.

The last approach to be presented here was developed by Brinkley and Kirkwood [40]. The authors solved the problem of propagation of the shock wave in the liquid using a different point of view. The basic idea of the theory is the following. The equation of continuity (A.8) and the equation of motion (A.10) include four partial derivatives of pressure and velocity. The third equation to complete the set of equations can be obtained from the Rankine-Hugoniot relation at the shock front (3.72)-(3.74). The authors obtained the fourth relation using the assumption that at some distance from the charge the decrease of the shock wave energy must be equal to the internal energy stored in the liquid after the shock wave has passed. In order to express the energy, the

3.4 CURRENT STATE OF KNOWLEDGE - THEORY OF SHOCK WAVES

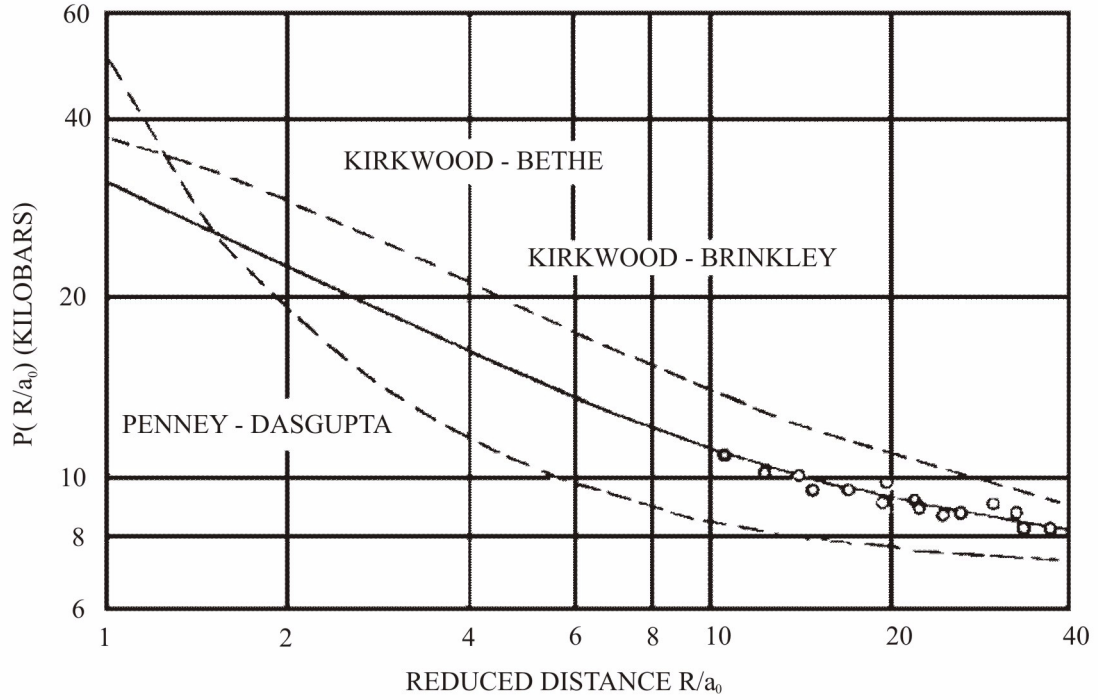


Fig.3.11 Comparison of calculated pressures for TNT charge. Reprinted from Cole [35].

authors introduced a similarity parameter into the equations, which represents a shape of the pressure-time profile of the shock wave. After combining the equations the authors evaluated the peak pressure p_s and the shock wave energy E_s as a simple derivative of position r_s in the form

$$\frac{dp_s}{dr_s} = \frac{\partial p_s}{\partial r_s} + \frac{1}{u_s} \frac{\partial p_s}{\partial t} = f[E_s, p_s, r_s] , \quad (3.84)$$

$$\frac{dE_s}{dr_s} = -\rho_0 r_s^2 h_{dis}(p_s) . \quad (3.85)$$

Here E_s presents the energy of the shock wave and $h_{dis}(p_s)$ is the specific enthalpy increment experienced by the liquid after crossing the shock wave and also after reaching the final equilibrium. If the enthalpy $h_{dis}(p_s)$ is known as a function of the peak pressure, these two equations give a complete distribution of the shock wave energy along the shock wave position. The comparison of these three theories is shown in Figure 3.11. The comparison shows that the theory given by Kirkwood and Brinkley is in the best agreement with the experimental values. Note that this theory is the only theory presented here, which does not neglect the dissipation effects.

3.5 Regular and retrograde fluid

As the term retrograde fluid will be often used within this work, the following chapter gives a short review of retrograde behaviour. The essential feature of retrograde fluid is that its vapour can condense when subjected to an adiabatic compression. In contrast, the regular fluids can only condense upon adiabatic expansion. A sufficient condition for fluid to be retrograde is that some part of the saturated vapour boundary in the temperature-entropy plane has a positive slope:

$$\left(\frac{\partial s}{\partial T}\right)_{sat} > 0. \quad (3.86)$$

Index “*sat*” indicates a change along the saturation line. Some examples of $T - s$ diagrams for retrograde and regular fluids are illustrated in Figure 3.12. The slope of the saturation line can be evaluated from the exact differential of entropy $s = s(T,s)$ with the help of Maxwell’s relations that can be found e.g. in Středa [5],

$$T\left(\frac{\partial s}{\partial T}\right)_{sat} = c_v + T\left(\frac{\partial p}{\partial T}\right)_v \left(\frac{\partial 1/\rho}{\partial T}\right)_{sat}. \quad (3.87)$$

In this equation, c_v is the specific heat capacity at constant volume. On the left branch of the saturation curve (up to the critical point) the derivatives on the right-hand side of Eq. (3.87) are always positive. As the capacity is positive, the saturation line cannot change its sign in this region. On the right branch the second term on the right hand side is always negative. However, in some cases, when the heat capacity is sufficiently large, the slope can become positive in some regions. In order to determine whether the fluid is retrograde or not, standard heat capacity has been introduced by Thompson [48]. This capacity is expressed as a function of molar heat capacity, which is an increasing function of molecular weight. Thus the retrogradicity is usually associated with fluids having high molecular weight, because a complex molecule has many degrees of freedom, which can be used to store internal energy. The retrograde liquids are thus capable to store more energy to cause the phase change than the regular fluids.

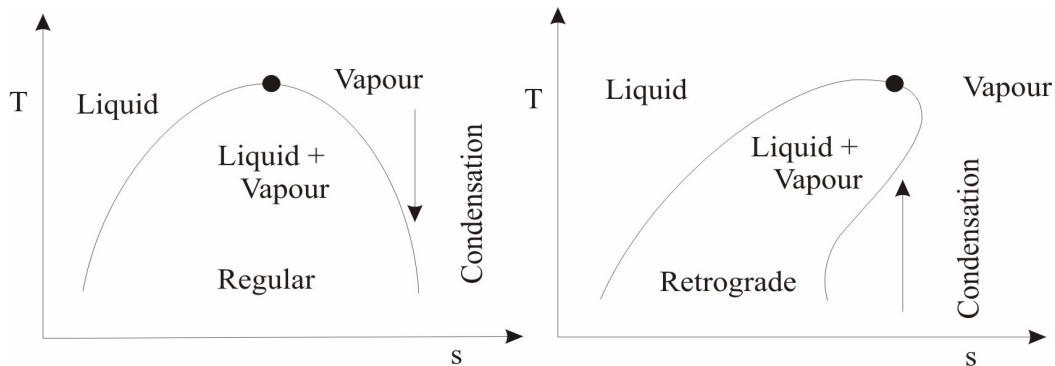


Fig.3.12 Condensation in temperature-entropy diagram for illustration of the difference between regular and retrograde fluids.

4. EXPERIMENT AND MEASUREMENT

This chapter describes the design of experimental setups for measurement of cavitation bubbles and shock waves generated in different liquid media. The introductory part is focused on the laser techniques used in the experiments to produce LIB. In order to interpret the results of the experiments, the basic principle of shadow imaging method is given in brief. The next part of the chapter describes the experimental setups used for the shock wave and cavitation bubble measurement, including the setups used for the investigation of the bubble collapse near the solid wall and bubble flotation in liquid. A new multi-exposure method for the measurement of the shock wave propagation and cavitation bubble dynamics is described in detail. The results from the individual measurements are summarized and discussed in the main part of the chapter to deduce the phenomena accompanying LIB and to prepare the background for the compilation of the physical model.

4.1 Measurement methods and experimental devices

4.1.1 Basic principle of lasers - types of lasers

Laser (Light Amplification by Stimulated Emission of Radiation) is an optical device, which uses the effect called stimulated emission to produce an intensive beam of light of defined frequency, phase, direction and polarization properties. A schematic diagram of a basic laser is shown in Figure 4.1. The stimulated emission can be explained using Bohr's atom model, in

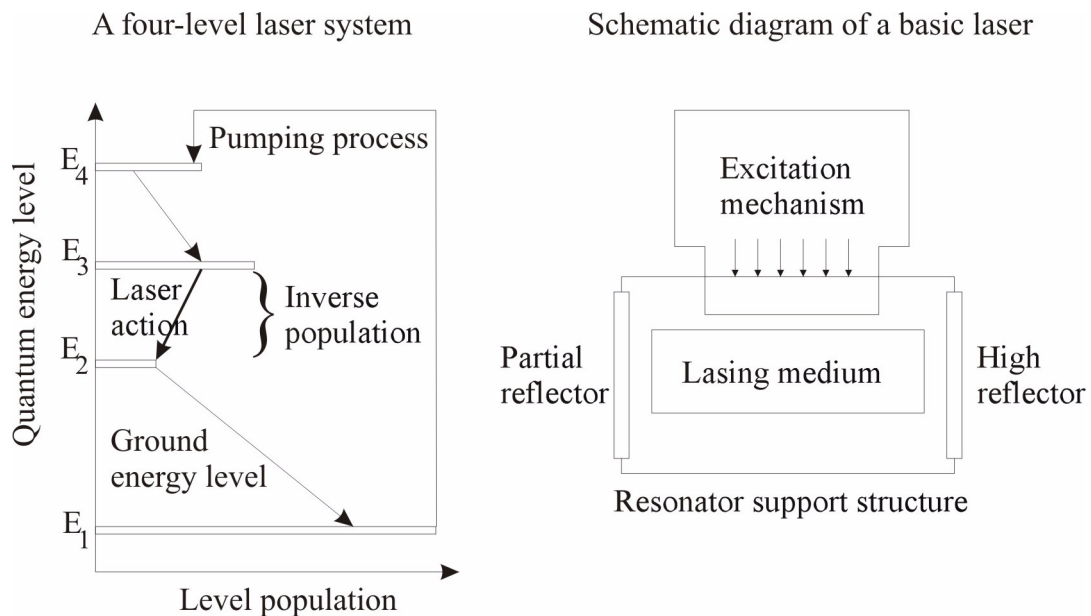


Fig.4.1 Basic principle of laser.

which the electrons are placed at given orbits around an atom nucleus. The placement of the orbits is given by the lasing medium and each orbit is defined by its energy level called “quantum level”. Only a limited number of fixed orbits are available for the electrons. An electron of the atom can be excited from a lower energy level to a higher one by absorption of external energy in the form of a photon, which is given by $E_{\text{photon}} = h\nu$, where h is Planck’s constant and ν is the frequency of the light. If an electron is in an excited state, it must decay to a lower one, losing energy in form of a photon. This effect is called spontaneous emission and the electron is emitted in a random direction and in a random phase. The average time for the electron to decay from the higher level to a lower one is called time constant of spontaneous emission. See illustration in Figure 4.1. If an electron is in the energy state E_2 , and it has to decay to E_1 , then if a passing photon is absorbed, whose energy is approximately equal to the difference between the levels, there is a probability that the radiated photon will have the same direction and the same phase as the passing electron. This process is called stimulated emission. The passing photon and the radiated photon can cause the stimulated emission of two other photons and the stimulated emission is amplified in this way. Bringing the electrons to excited states is ensured externally by an energy source, which is usually called “pump” source. Under common criteria the probability of simulated emission is quite small, because there are always more atoms at lower energy levels than at the higher ones and the probability of the spontaneous emission is the same as the probability of the stimulated emission. To produce a beam of coherent¹ light an inverse population has to be created. The creation of the inverse population can be demonstrated on a four-level energy diagram shown in Figure 4.1. In the diagram, the electron is first pumped into the upper level E_4 by an exciting mechanism. It decays to E_3 , then to E_2 , and finally to E_1 with the corresponding time constants. If the time to decay from E_2 to E_1 is much longer than the time to decay from E_3 to E_2 , a large amount of electrons (the inverse population) occurs between the levels E_3 and E_2 . With the inverse population there is a possibility to amplify the signal through the stimulated emission, however, the total amount of the coherent radiation is small and most of the electrons emit spontaneously. In order to force the major part of the photons to contribute to the coherent light, a positive feedback is needed. This is done in the optical resonator, a system of mirrors that reflects undesirable photons out of the system and reflexes the desirable photons back into the excited population, where they can assist the amplification.

According to the lasing medium, three basic types of lasers are distinguished: gas, solid state and semiconductor lasers. The most frequently used solid-state laser is the Nd-Yag laser, whose lasing medium is formed by an Nd-Yag crystal. The solid-state laser can work in two working modes; in the *free running mode* and in the *Q-switched mode*. In the free running mode the laser light emission starts, when the pumping energy exceeds the energy losses in the optical resonator. In the free running mode the population inversion is accelerated gradually, whilst the pumping energy increases. The losses in the resonator are almost constant in this mode. The generation starts at a low level of inverse population and proceeds irregularly. The length of the outcome pulse is high and the top power level is low. In the Q-switch mode (the mode with the changing

1. Coherent wave has the frequency and the phase difference uniform in time and space.

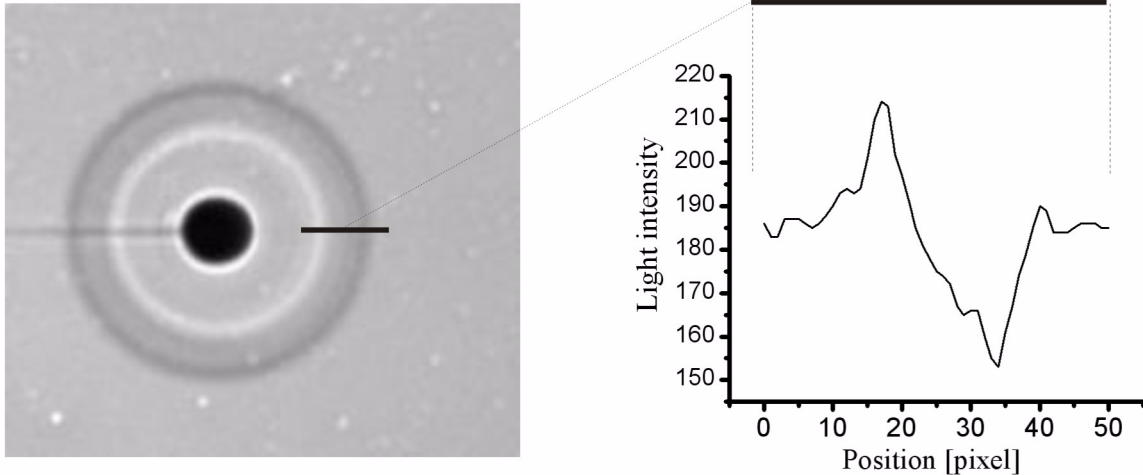


Fig.4.2 Intensity distribution in shadow photography along a line.

quality of optical resonator) energy losses of the resonator are set up at a high level not to allow any emission, until the population inversion level reaches a higher value. At this instance the resonator losses are reduced quickly. The generation of population is speeded up in a very short time interval and the laser gives a pulse of high power.

The laser energy can be deposited into the required place using various kinds of lens systems or using an optical fiber, which is frequently applied in medicine. In this work, both methods are used. For more information concerning lasers, see e.g. Saleh [6] or <http://www.mellesgriot.com/>.

4.1.2 Principles of optical methods used in measurements

Optical methods used for visualization of fluid flow utilize the natural changes in the optical properties occurring in the liquid during the flux. These methods are based on two physical principles:

- a) The speed of light in a given material depends on the refractive index of this material and the refractive index depends on the density of the material.
- b) The light is being diffracted or refracted during the passing through a region of density change.

The basic method for visualization used in this work is the shadowing method, which is based on the principle b. The method measures the second derivative of density, i.e. the first derivative of the density change. According to the method, the positive change of the density gradient (increase of density) corresponds to darker places and the negative change of the density gradient (decrease of density) corresponds to lighter places. Intensity distribution in shadow photography along a line of a shock wave recorded by this method shows two dark bands in the front part of the wave and one lighter band in the back part of the wave (Figure 4.2). The detailed description of the method is given e.g. in Řezníček [21].

4.1.3 Methods of the shock wave and bubble measurements

The experimental investigation of plasma dynamics, shock wave propagation and time evolution of a cavitation bubble is restricted to the measurement of only some quantities describing the phenomena.

The parameters characterising the plasma creation are given by the laser beam parameters such as the wavelength λ , pulse width τ_{La} , beam waist radius w and laser pulse energy E_{La} or laser pulse power P_{La} . These parameters are described in detail in Chapter 3.2.2.

The shock wave can be fully described by measuring its velocity or pressure distribution in space and time. The shock wave velocity is usually measured by the pump-probe technique. The shock wave position is photographed at various distances with different time delays. The shock front velocity $u_s(r)$ is deduced from the slope of the $r(t)$ curve of the shock wave position. This velocity and the quantities behind the shock front are related to each other by the Rankine-Hugoniot equations introduced in Chapter 3.4. The peak pressure $p_s(r)$ corresponding to the shock wave velocity can be obtained using an appropriate equation of state. In order to determine the temporal evaluation of the shock wave pressure $p(r=const, t)$, one has to use a sensor fixed at one place, which will record the pressure increment at this place. It is easy to find out that the peak of the temporal pressure profile is one point on the shock wave pressure-position curve. Usually, the measurement of the shock wave is divided into a near and a far field measurement. The measurement of the shock wave propagation in the near field can be accomplished by several different optical techniques. In the optical pump-probe technique the laser beam is divided into two beams. The beam of higher intensity is used to generate the optical breakdown and the beam of lower intensity, displaced at a distance, is focused on a diode. If a shock wave is generated the probe beam is deflected and a signal occurs on the diode. The shock wave velocity is then deduced by dividing the distance between the beams by time. The probe beam can be optically delayed in order to measure at some more distant position. Similarly, shadow photography uses a pump beam to generate LIB and the probe beam is used to illuminate the image. The temporal resolutions of these techniques are given by the duration of the laser pulse or camera exposure. In the measurement of shock waves in the far field, the shock wave velocity is already close to the sound velocity and the only information from this region is that on the temporal profile of the shock wave and the shock wave velocity. To obtain the temporal profile of the shock wave in the far field the PVDF (Polyvinylidenfluorid) hydrophone can be used. These hydrophones use the piezoelectric effect for the pressure/voltage conversion. This technique cannot be used in the near field because of a possible hydrophone damaging. The technique that can also be used in the near field measurements is the Laser differential interferometry. This technique was used e.g. by Garen [22] for investigation of the shock wave propagation in isooctane. However, the most measurements focused on the mechanical effect of LIB used in medical applications were provided by Vogel [23] and his co-authors.

The cavitation bubble phenomena produced by LIB is usually characterised by the bubble wall velocity dR/dt , the maximum bubble radius R_{max} for each oscillation or the life time of the bubble τ_{Ra} . The maximum bubble radius and the oscillation time for a spherical bubble are connected by

Eq. (3.50). The parameters measured usually during the bubble collapse, described in Chapter 3.3.6, are the ratio between the bubble distance from the solid wall d divided by the maximum bubble radius $\sigma_B = d/R_{max}$ or by elongation in the direction to the wall $\sigma_B = d/R_{ver}$.

It is necessary to understand that the time scale for the measurement of the shock waves differs from that used for the measurement of cavitation bubbles by more than one order, and the recording requirements are different. Let us assume a cavitation bubble in water of a maximum radius smaller than 2.5 mm. Such a bubble has a collapse time of about 60 μ s, which corresponds to the half of the time of the bubble growth-collapse period. If a plot of the period of the bubble time evolution has to be recorded, the time resolution of the recording of the order of μ s is required. Let us speculate in the same way about a shock wave in water, with the velocity three times higher than the speed of sound in the liquid. The shock wave velocity usually drops to the value close to the sound velocity within the region of about 1 mm. The shock wave will pass through this region approximately in 225 ns. In this case the time resolution of the order of ns is required. As a result it is not possible to record both the shock wave and bubble time evolution in one continual recording. The experimental arrangements and the measurement methodology were mildly different for the shock waves and for the cavitation bubbles, but all the measurements were basically realized on the same standard setup, which was customized.

4.1.4 Single and multi-exposure recording

The CCD camera used in the experiments allows two different kinds of recording, a single-exposure and a multi-exposure record. The camera was able to take 100 frames per second in the single-exposure mode, but it could take 10 fast exposures with the minimum time delay of 100 ns

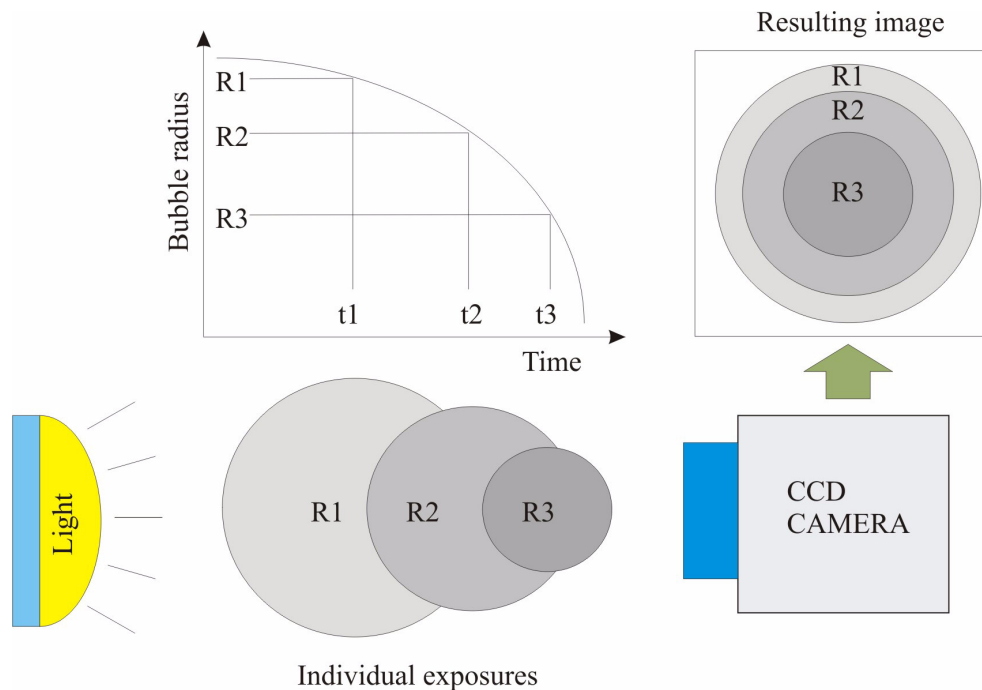


Fig.4.3 Explanation of the multi-exposure record.

and the exposure time of 100 ns in the multi-exposure mode. The principle of the multi-exposure method can be explained using the example of a bubble collapse from its maximum radius, as shown in Figure 4.3. The bubble was generated at the time t_0 by LIB. When the single exposure method is used, the first exposure of the bubble of the radius R_1 is taken at the time t_1 and this figure is saved to the computer. To make the exposure at the position R_2 at the time t_2 , the second LIB has to be produced and the triggering of the camera and the light source has to be shifted to the time t_2 . In the same way the exposure for the radius R_3 at the time t_3 is recorded. Now three single exposures are recorded, but each for a different bubble (a different physical event). However, when the reproducibility of the bubble creation is fulfilled, it can be supposed that the bubble represents the same physical event. The reproducibility can be verified by the measurement of the energy entering the liquid. For the single-exposure recording many figures have to be recorded for each time position.

The basis of the multi-exposure recording method is the camera mode, which allows to save one or more exposures into one picture. The exposures overlap each other as shown in Figure 4.3. The first exposure is taken in the same way as for the single-exposure mode at the time t_0 , but the next exposure times are not changed by shifting the camera and the light trigger signal, but they are set directly using camera control software. No other LIB is produced. The advantage of this method is that the time evolution of one bubble (physical event) is recorded and it is easier to maintain the reproducibility. The disadvantage of the method is that an intensive light source upon

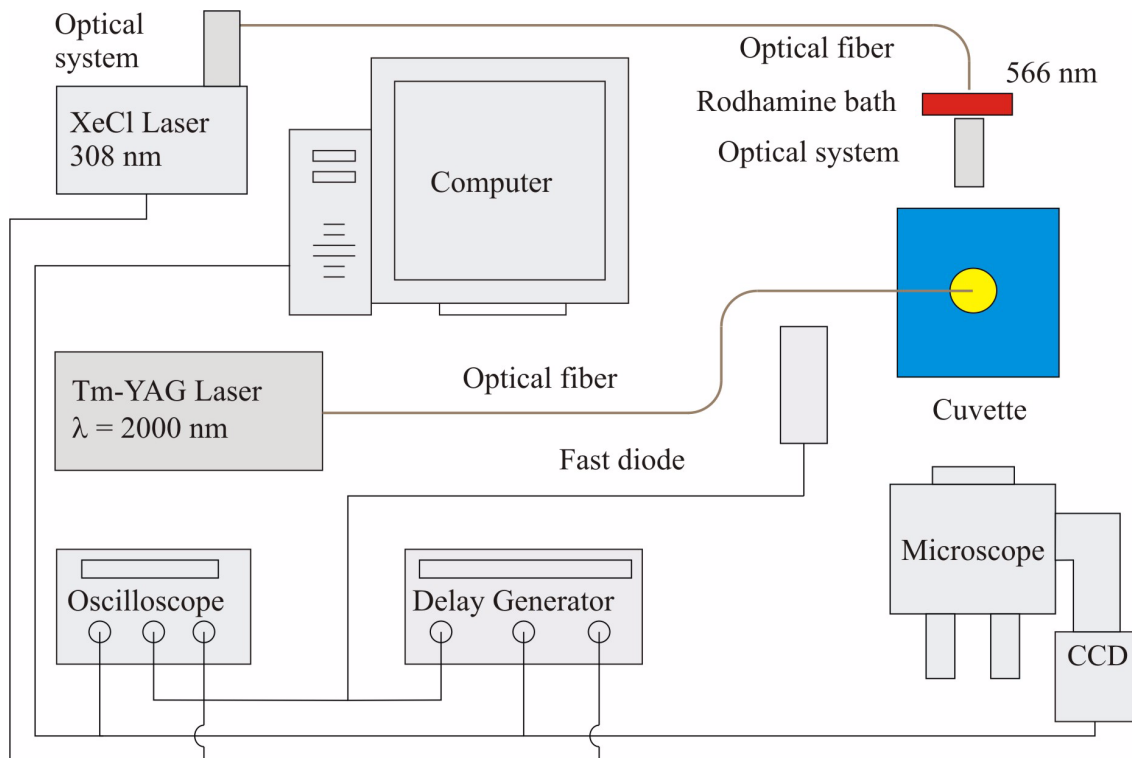


Fig.4.4 Schematic illustration of experimental setup using Tm-Yag laser.

4.2 EXPERIMENT AND MEASUREMENT - EXPERIMENTAL SETUPS

a relatively long time is required, which is not available from the flash light source. The recordings are thus limited by the duration of the flash lamp pulse of 400 ns and by the intensity of the continual light source. This method is also restricted to events, where it is possible to recognize the individual exposures, which is the case of shock waves and cavitation bubbles.

4.2 Experimental setups

4.2.1 Experimental setup using Tm-Yag laser

The assemblies of experimental setups using the Tm-Yag laser are showed in Figure 4.4 and in Figure 4.5. The Tm-YAG BAASEL Lasertech BML 800 laser in the free running mode and in the Q-switched mode is used to produce pulses at the wavelength of 2000 nm and width from nano-seconds in the Q-switched mode to milliseconds in the free running mode. Using an optical setup, the laser pulses are focused into the optical fiber, which conducts them into the cuvette, where LIB is produced. The figures were recorded by the CCD camera Imager mounted on a microscope. The exposure lighting is provided by continual and pulse light sources. For the continual lighting the halogen lamp KL 1500 Electronic is used and the pulse lighting is provided by the excimer laser XeCl LPX 100 at wavelength 308 nm and pulse length 30 ns. The wavelength of the excimer laser is transformed into the visible range of 566 nm using the rodhamine bath.

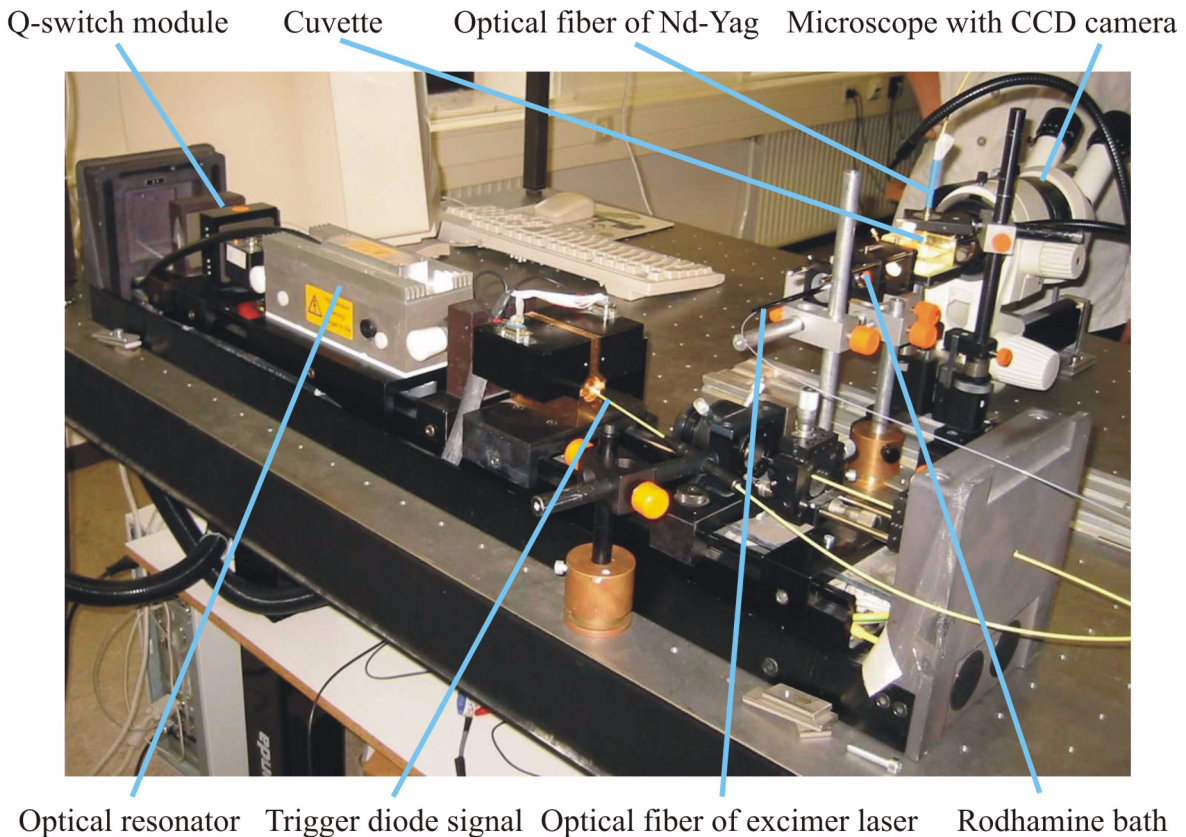


Fig.4.5 Experimental setup for Tm-Yag laser

passing through the bath the scattered light is concentrated into a beam and focused onto the microscope. To trigger the system, an ultra fast photodiode is placed in front of the exit of the Tm-Yag laser resonator, where the laser light is first visible. The synchronization of the system is controlled by the delay generator and the oscilloscope TECTRONIC TDS 684A. The laser energy is measured by internal energy meters, which had to be calibrated before each measurement.

Generation of shock waves and cavitation bubbles is initiated at the top of the optical fiber, which is placed perpendicularly to the optical axis of the system and perpendicularly to the liquid layer. The whole process is triggered by an optical signal produced by the light coming out of the laser flash lamp (pumping source). Because the flash lamp initialized the flash pulses before the laser light is emitted, a time delay occurs, which is used to start other system components such as the light laser and the camera. The diode signal is linked to the delay generator as its trigger signal. After being triggered the delay generator sends a signal to the camera card to activate the CCD array. The second signal is emitted to start the excimer laser. Each signal is connected to the oscilloscope, which allows to control the start times of the laser and the camera.

4.2.2 Experimental setup using Nd-Yag laser

The experimental setups used for the investigation of cavitation bubbles and shock waves using the Nd-Yag (New WaveResearch, Tempest) laser are illustrated in Figure 4.6 and in Figure 4.7. For the experiment the laser was used in the Q-switched mode with the wavelength 1064 nm and pulse duration 6 nanoseconds. A beam of light 1 cm in diameter produced by the

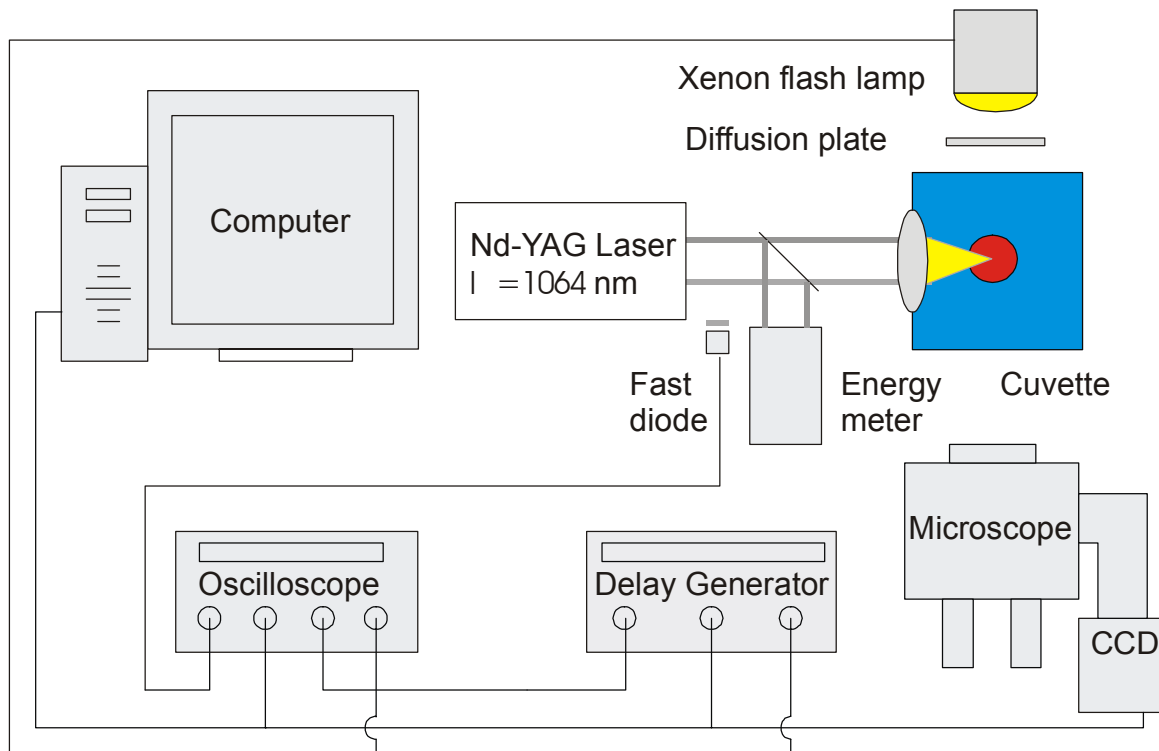


Fig.4.6 Schematic illustration of experimental setup for the measurements using Nd-Yag laser.

4.2 EXPERIMENT AND MEASUREMENT - EXPERIMENTAL SETUPS

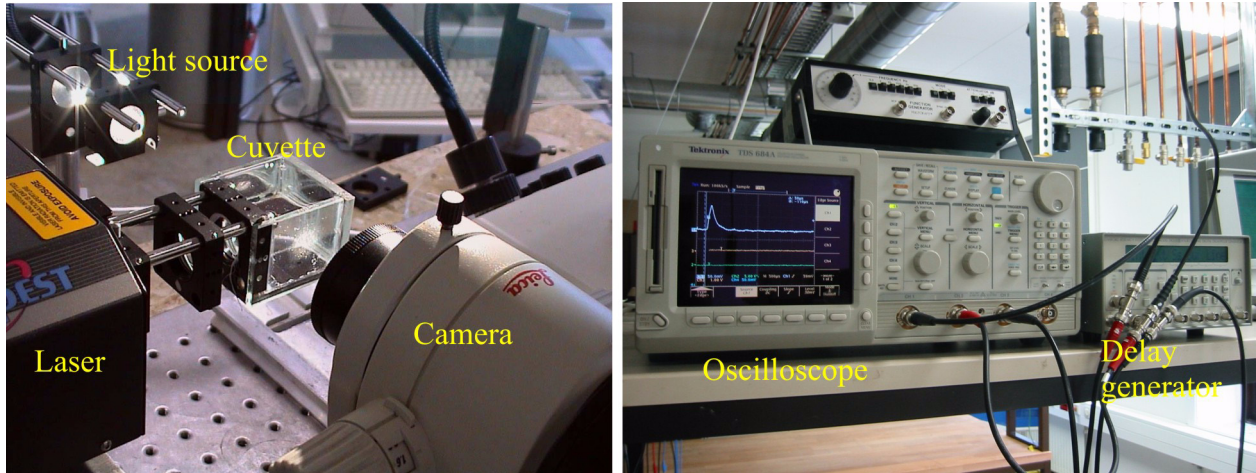


Fig.4.7 The experimental setup for the measurements using Nd-Yag laser.

laser was focused into the cuvette through an achromatic doublet lens, which was built in one of the cuvette walls. The figures were taken by Imager CCD camera mounted on the microscope. Continual lighting was provided by the halogen lamp KL 1500 Electronic. The light from the lamp was transformed through a two-lens optical system to a parallel beam of light. Flash lighting was provided by a xenon flash lamp (Drelo Bal 1507) with the pulse duration 400 ns. To homogenize the flash light, a diffusion plate of glass was placed between the cuvette wall and the light source. The total amount of energy brought into the liquid was calculated from the energy reflected on the glass plate placed at 45 degrees against the laser beam measured by an energy meter placed perpendicularly to the beam direction. The fraction of the energy was then calibrated before or after the measurement using the second energy meter. The measurements were performed for the low energy level of about 1 mJ, which ensured that no hot spots occurred outside the focal region before the plasma initiation. To improve the accuracy of determining the time when the laser pulse is produced, an ultra-fast diode with the time response less than 200 picoseconds was used. The trigger signals to run the laser, the camera and eventually the flash light were generated by the delay generator. The synchronization of all signals was controlled by an oscilloscope.

For the measurement using the multi-exposure method a test measurement using the single-exposure method was performed to map the bubble evolution in order to adjust the camera exposures and the delay times. Each bubble evolution was divided into expansions and compressions. The first exposure (bubble size) from the bubble expansion had to be the same as the last exposure (bubble size) from the previous one. Also the same size of the first maximum bubble was required in each measurement set. This ensured that the delivered energy was approximately the same during all the measurements. It is possible to assume that the bubbles with the same maximum radii were produced by the same amount of energy, because the mechanical energy necessary for the bubble to grow to its maximum radius is roughly determined by the radius value and the liquid properties.

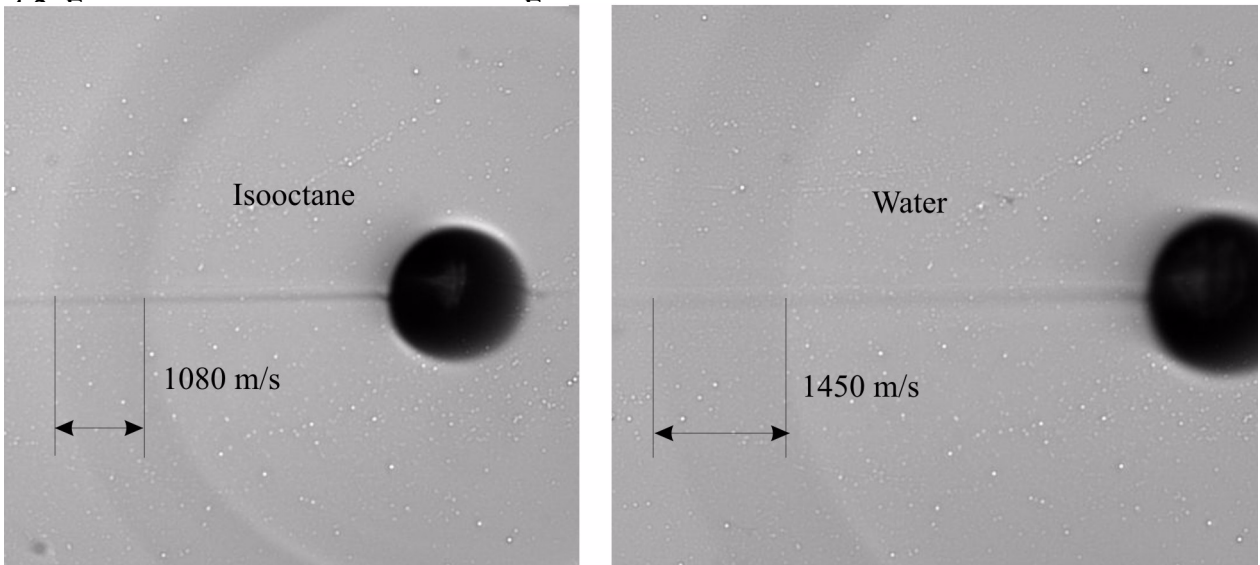


Fig.4.8 Interpretation of the shock wave velocity from circumscribed circle.

The measurement of the shock wave propagation was performed by the single-exposure and the multi-exposure methods. However, the accuracy of the results obtained by the multi-exposure method, especially close to plasma, was very poor, because the exposure time of 100 ns captured the main part of the shock wave velocity changes. Due to this reason, only the results obtained by the single-exposure method were used for the shock wave velocity evaluation. The results obtained by the multi exposure method were used only for visualization. An example of the shock wave propagation recorded by the multi-exposure method is shown in Appendix E Figure E1. The shock wave velocity was calculated from the slope of the curve of the shock wave position in the near field and directly from the path written by the shock wave during the exposure time in the far field (Figure 4.8).

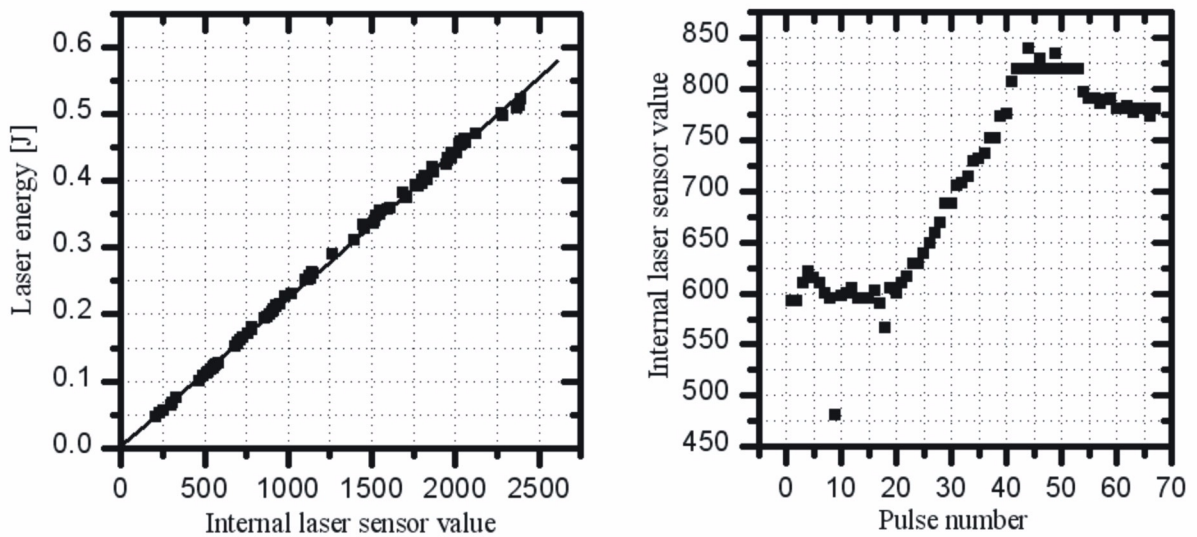


Fig.4.9 Calibration curve for internal sensors of Tm-Yag Laser.

4.3 Measurement results

4.3.1 Results of measurements using the Tm-Yag laser

The measurements using the Tm-Yag laser were carried out only with distilled water. The cavitation bubbles were recorded using a single and multi exposure modes and the shock waves were recorded only by the single-exposure method. Before the measurement an energy meter was used to calibrate the internal laser sensors value with real delivered energy. An example of such a measurement is shown in Figure 4.9 (left). The dependence of the laser energy on the internal sensor value was almost linear, but it varied strongly with time (number of pulses), which destroyed the measurements data. The laser energy oscillated in the wide range of energies, as it is evident from Figure 4.9 (right). The jump on the curve is caused by the cooling process on the flash lamp.

Figure 4.10 shows the measurement using the single-exposure method with the laser energy of about 0.1 J. The step of the camera triggering time was 10 μs , which means that the figures were taken at times 0, 10, 20 μs etc. For each time, 5 figures were recorded. The exposure time was given by the duration of the excimer laser pulse, which was about 40 ns. In Figure 4.10 and Figure 4.12 the bubble expansion and compression in the single-exposure mode are presented. It is obvious from Figure 4.10 that the first bubble expansion is slightly slower than the bubble compression. The values of the bubble radius are strongly influenced by the instability of the laser energy. It causes a considerable difference in the values of the maximum bubble radius and also in the bubble collapse time. At the end of the first bubble collapse a shock wave is produced as shown in Figure 4.11, but the time evolution of this wave is hardly recordable, because of the instable laser energy output. The bubble shape is strongly influenced by the presence of the opti-

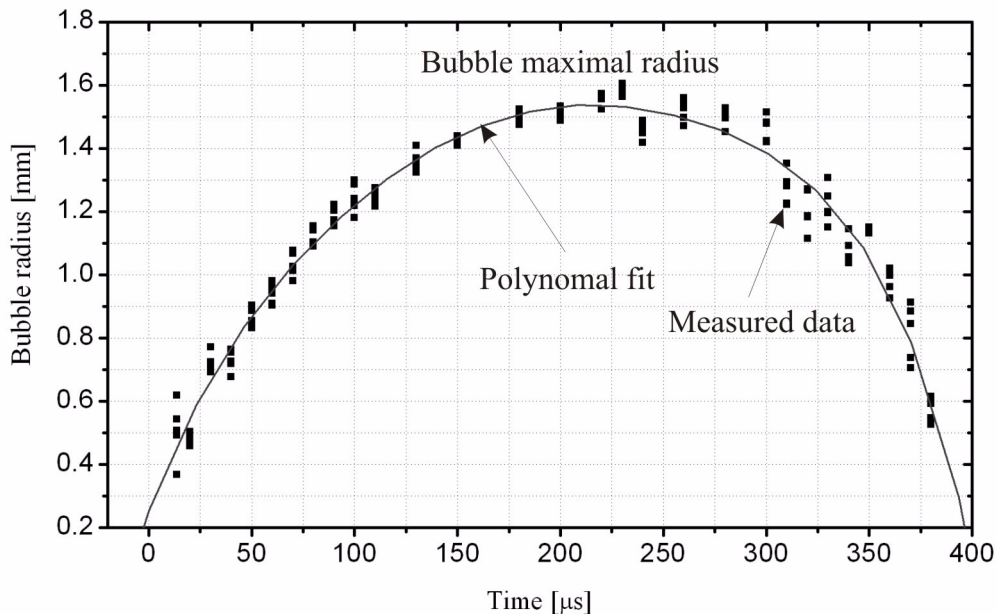


Fig.4.10 Time history of bubble radius produced by Tm-Yag laser recorded using the single-exposure mode.

4.3 EXPERIMENT AND MEASUREMENT - MEASUREMENT RESULTS

cal fiber. The bubble partially envelopes the optical fiber, which results in the typical bubble elongation in the fiber direction. It can be seen from Figure 4.11 and also from the last frame in Figure 4.12 that during the bubble collapse near the solid wall presented by the optical fiber, a jet is generated striking the wall. The most likely mechanism for the damage of the fiber is the cavitation erosion. In Figure 4.13 the results of the experimental measurement of the bubble evolution in time using the multi-exposure mode are shown. The corresponding radius-time curves are shown in Figure 4.14. As the lighting for the multi-exposure mode had to be provided by the continual halogen lamp of poor intensity, the exposure time of $1 \mu\text{s}$ was used, which did not

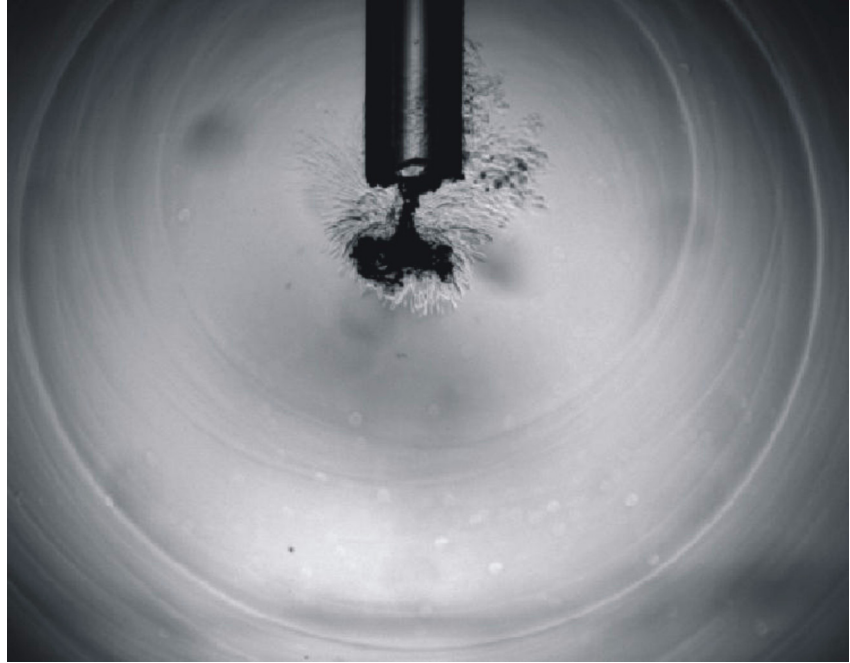


Fig.4.11 Cavitation bubble compression and expansion at the end of the optical fiber and the following shock wave propagation. In the centre of the figure, a jet damaging the fiber is also visible.

As the lighting for the multi-exposure mode had to be provided by the continual halogen lamp of poor intensity, the exposure time of $1 \mu\text{s}$ was used, which did not

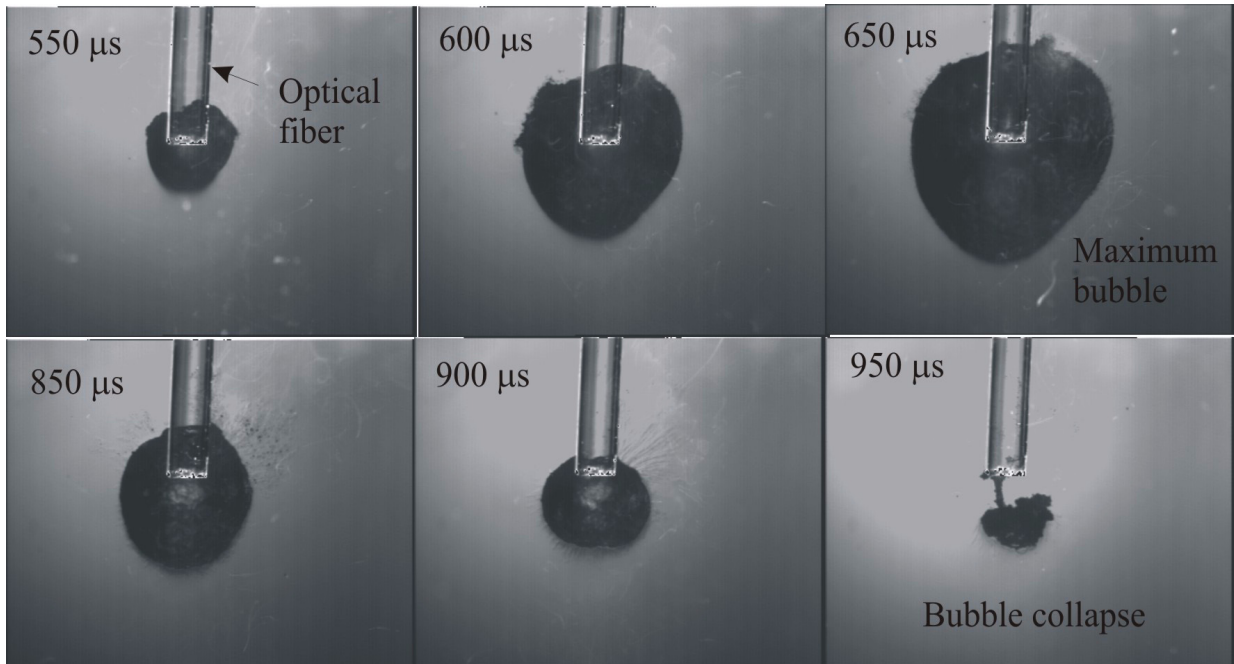


Fig.4.12 Compression and expansion of the cavitation bubble produced by the Tm-Yag laser recorded using the single-exposure mode.

4.3 EXPERIMENT AND MEASUREMENT - MEASUREMENT RESULTS

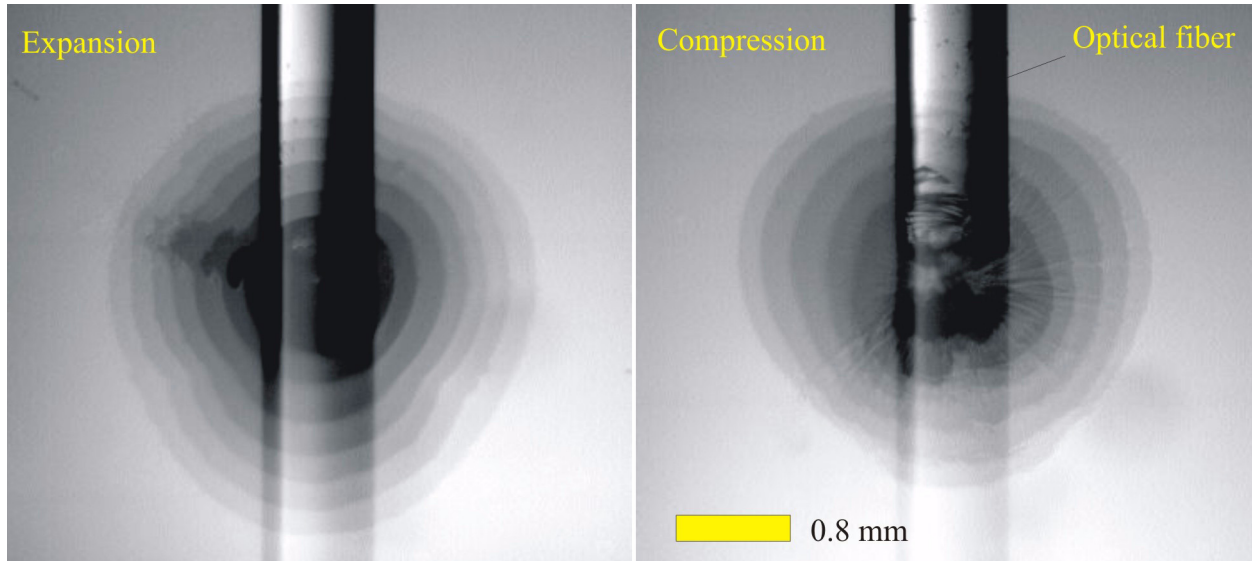


Fig.4.13 Compression and expansion of the cavitation bubble produced by the Tm-Yag laser recorded using the single-exposure mode.

allow to detect the shock wave produced at the end of the bubble collapse. The individual time curves of the bubble radius in Figure 4.14 show also the non-symmetry between the expansion and the compression. The shadow in the lower part of the Figure 4.13 is caused by reflection of the optical fiber.

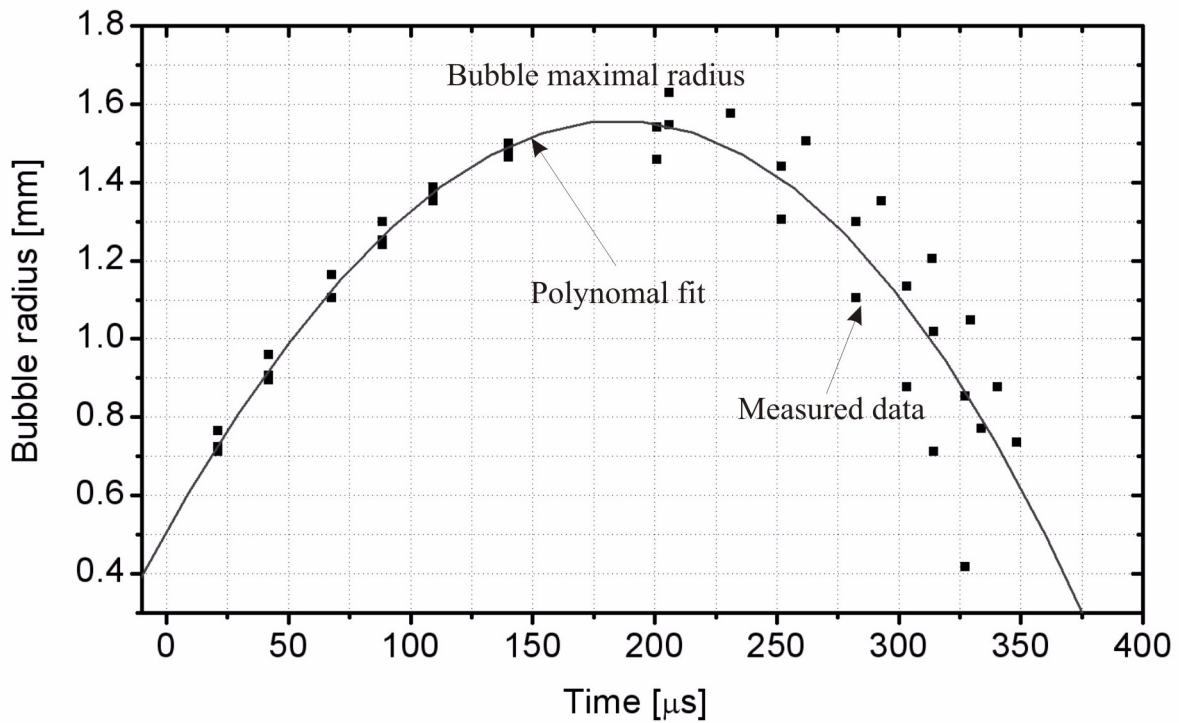


Fig.4.14 Time history of bubble radius produced by Tm-Yag laser recorded using the multi-exposure mode (The measurement presented in Figure 4.13).

4.3.2 Results of measurements using the Nd-Yag laser

Measurement of the cavitation bubble in water corresponding to the curve shown in Figure 4.15 shows the evolution of the radius of the cavitation bubble in water obtained using the multi-exposure mode. Figure 4.16 shows the corresponding development of the bubble radius in time. The bubble recording was divided into four phases representing separate expansions and compressions. The values presented in Figure 4.16 are the average values of three different measurements. The first exposure in Figure 4.15 (Phase I) shows, in fact, two very fast events - the maximum size of the plasma shape and the path of the ring, which originally enveloped the plasma shape. After the plasma expansion the bubble expands with a high velocity. This is evident from the steep slope of the bubble radius-time curve near the time 0 s. The high pressure caused by the high plasma temperatures allows the bubble to expand to its first maximum radius. For some measurements, there was a small fall in the values on the bubble radius-time curve before the bubble reached the maximum radius, however, due to data averaging the defect is not clear in Figure 4.16. This point might be the division point between the laser-induced cavitation and the classical bubble behaviour. During the compression (Phase II in Figure 4.15) the bubble shape is strongly deformed. The deformed shape consequently expands to the second maximum radius

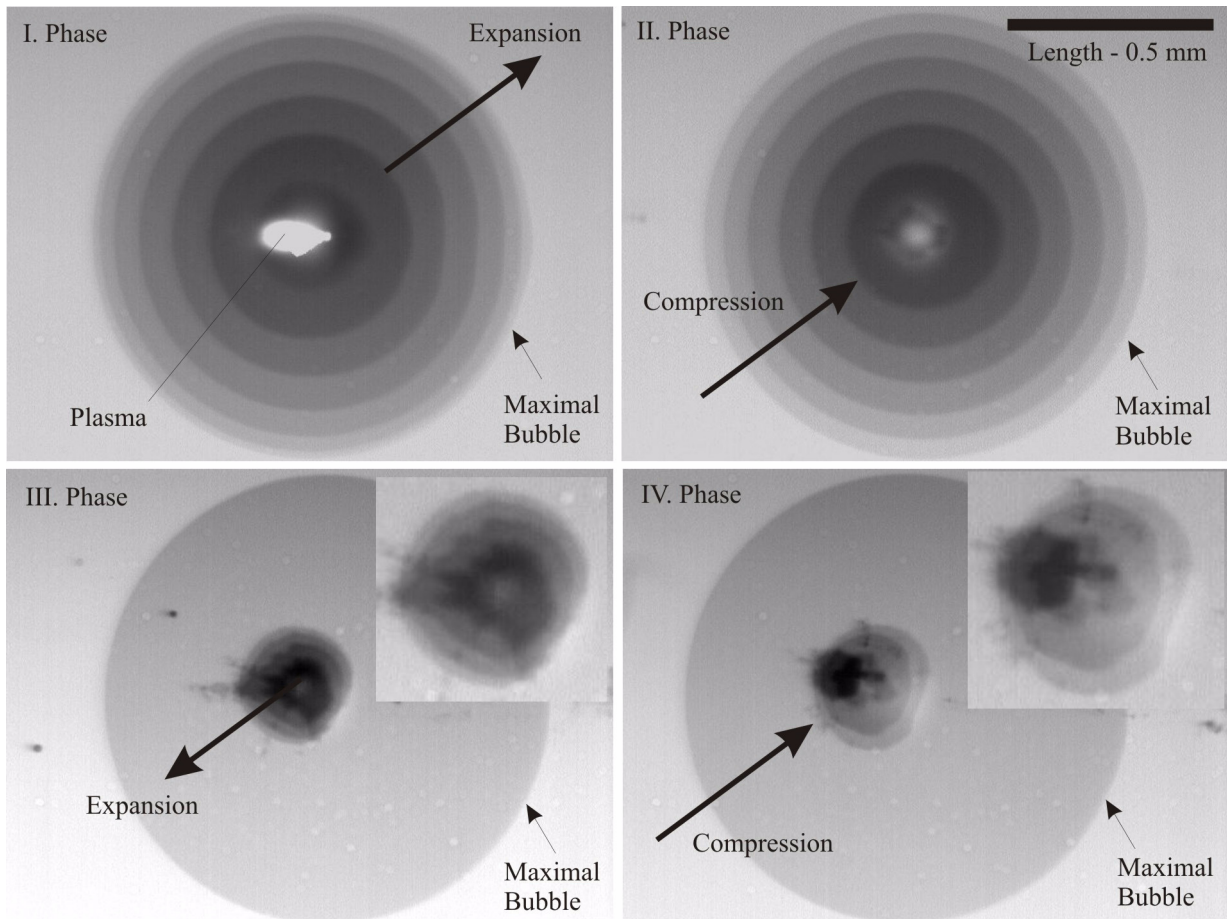


Fig.4.15 Measurement of the cavitation bubble in water corresponding to the curve shown in Figure 4.16.

(Phase III in Figure 4.15). From the figure of the third phase the elongation of the deformed bubble shape is apparent. From the figure detail it is also obvious that the bubble shape is striving to copy the initial plasma shape, which is the best visible in the detail of the figure of the fourth phase (Phase IV in Figure 4.15). The deformed shape of the bubble surface can indicate that the bubble represents a cloud of small bubbles, which behaves as the single bubble. From the bubble oscillations, it can be also deduced that the bubble contains certain amount of gas, which pressure satisfies the stability condition $p_g > p_{g_{crit}}$ given by Eq. (3.34).

The measurement of cavitation bubble dynamics in isooctane, which is presented in Figure 4.17 and in Figure 4.18 shows an apparent difference in the bubble oscillation in comparison with the case of water (compare with Figure 4.16). In the initial stage, the bubble is strongly accelerated as in the case of water and then expands up to the first maximum radius. After the first expansion (Phase I in Figure 4.17), a violent compression (Phase II in Figure 4.17) and first bubble collapse follows, which causes the bubble movement in the direction perpendicular to the optical axis. During the second (Phase III in Figure 4.17) and the third expansion (Phase V in Figure 4.17) the bubble shape is almost spherical. In some pictures a path of light is visible across the centre of the bubble, which is probably caused by the light reflection on the bubble surface. In the figure of the fifth phase (Phase V in Figure 4.17), small bubble parts resulting from the previous collapses are also visible. The bubble surface for isooctane is not deformed as apparently as for water. The explanation of this behaviour can be found in the theory of the spherical surface stability. From the comparison of the second maximum radii in water and in isooctane it is obvious that the pressure inside the bubble in isooctane is higher than in water. The stability condition for the spherical surface says that the bubble becomes more unstable with the increasing compression. If the gas pressure inside the bubble prevents the violent collapse, the bubble surface in isooctane will stay more stable than in water. At this point it is necessary to note that it is not possible to compare the maximum bubble radii in water and in isooctane, as in the previous cases, because the laser energies were not measured very accurately. The measurements presented in Figure 4.14 -Figure 4.18 were used because they represent the most illustrative differences in the bubble behaviour in both liquids. The time histories of the bubble radii in water and isooctane from the measurements where the laser energy was measured accurately are presented in Figure 4.19. The results show that the first maximum bubble radius is about 15 percent higher in

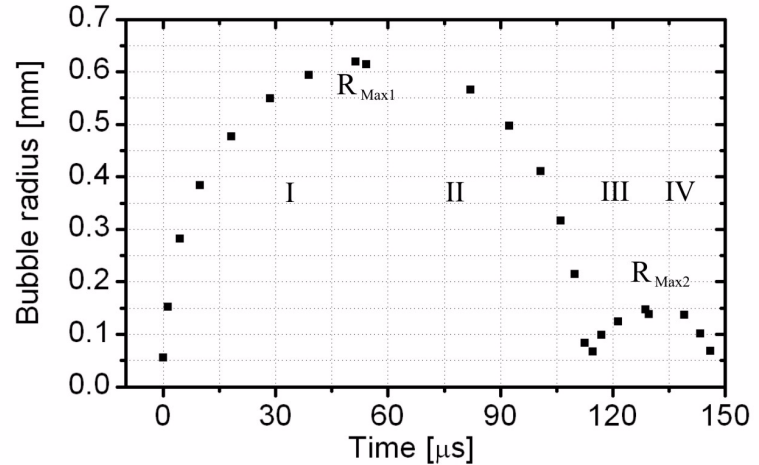


Fig.4.16 Time history of the bubble radius produced by Nd-Yag laser corresponding to the experimental data shown in Figure 4.15.

4.3 EXPERIMENT AND MEASUREMENT - MEASUREMENT RESULTS

isooctane than in water for the same laser energy and the second maximum radius is more than three times higher in isooctane than in water. The disproportion in the bubble behaviour in both liquids cannot be explained by different viscosity or surface tension. Although they differ, the difference is small. The results presented in Figure 4.19 will serve as a data model for the numerical simulations.

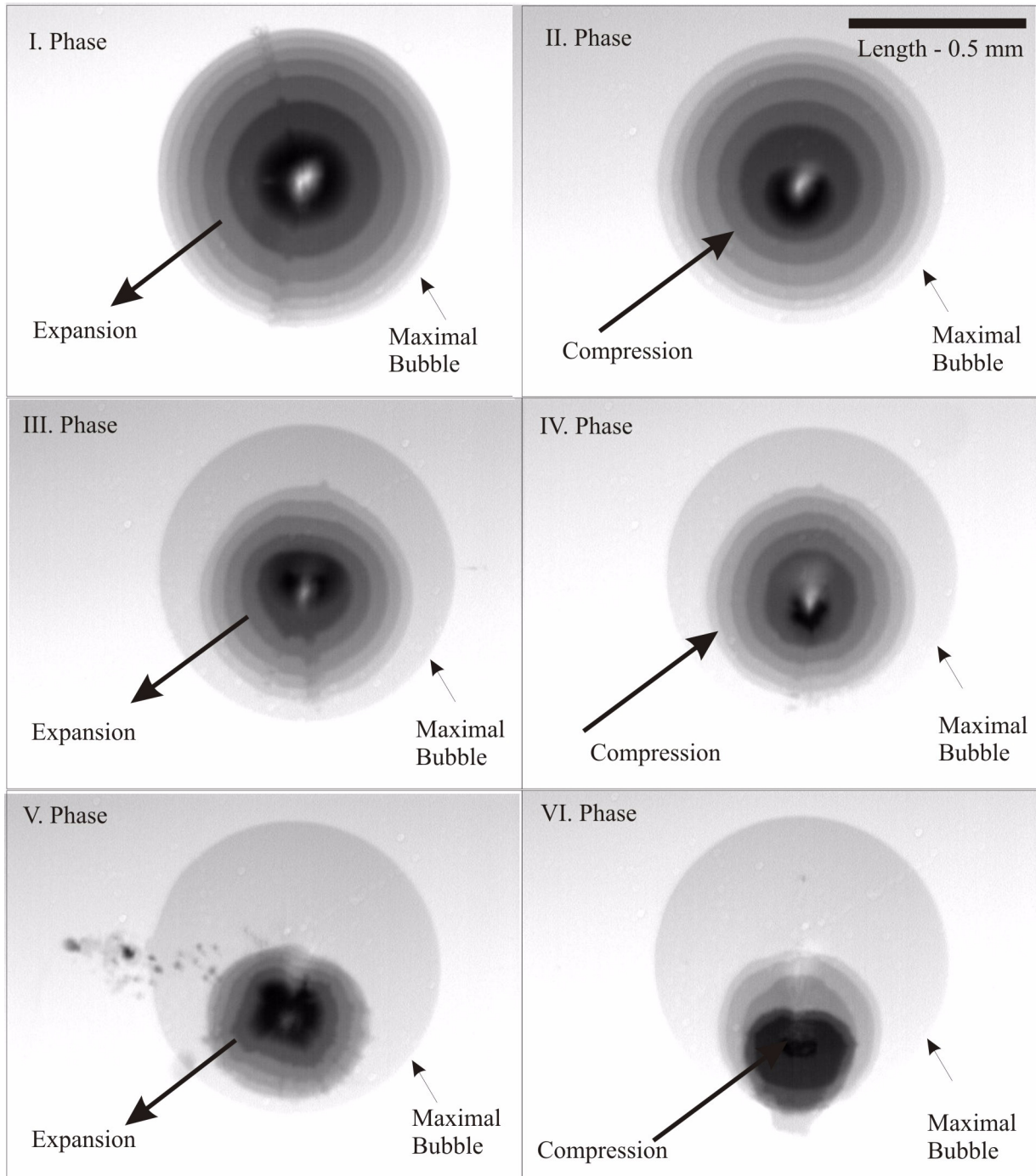


Fig.4.17 Measurement of the cavitation bubble in isooctane corresponding to the curve shown in Figure 4.18.

4.3 EXPERIMENT AND MEASUREMENT - MEASUREMENT RESULTS

The results obtained from the shock wave measurement in its initial stage in water and isooctane are presented in Figure 4.20. The line crossing the figures, coming from the left, represents the laser beam path. From the annulus traced by the shock waves it is obvious that the shock waves generated in isooctane are considerably slower than in water, as the shock wave writes a wider ring in water during the exposure time of 100 ns. The initial shapes of the shock wave and bubble are strongly influenced by the plasma deformation. The deformation is caused by the distributed plasma shielding and the plasma expansion back towards the laser side; these

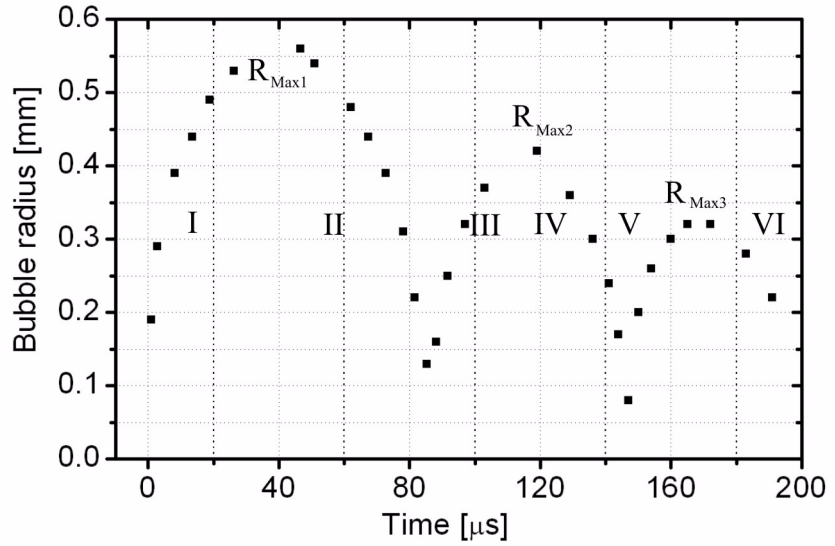


Fig.4.18 Time history of the bubble radius produced by Nd-Yag laser corresponding to the experimental data shown in Figure 4.17.

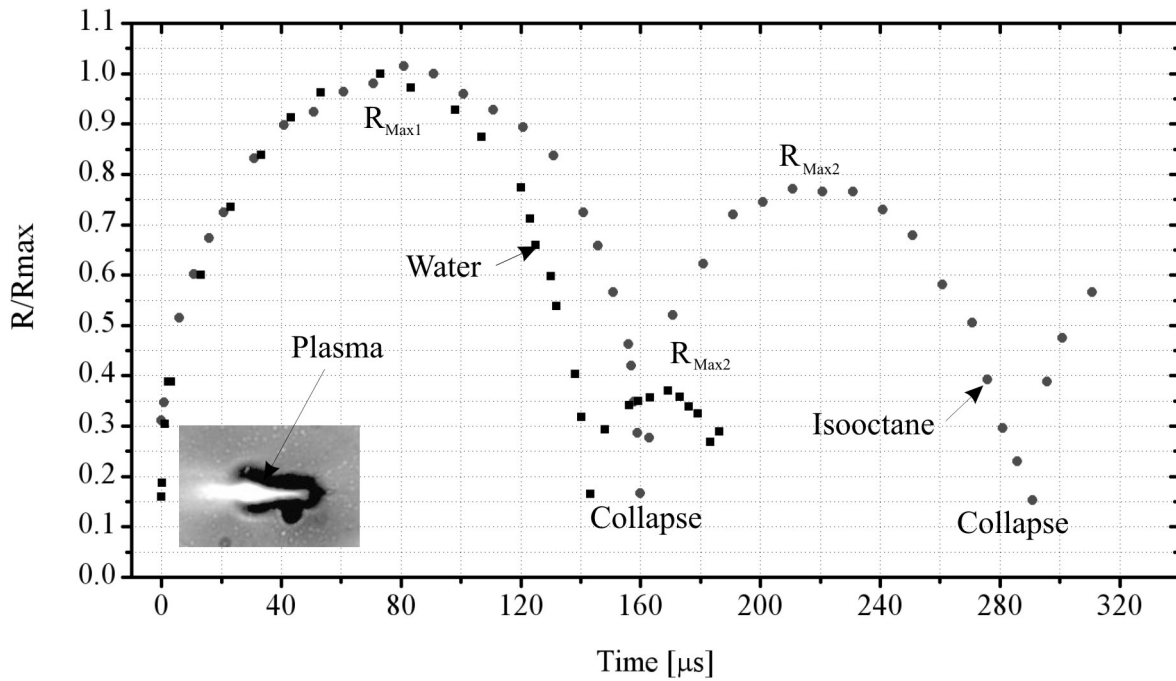


Fig.4.19 Time history of the bubble radius produced by Nd-Yag laser in water and isooctane after 1 mJ - 6ns laser pulse.

4.3 EXPERIMENT AND MEASUREMENT - MEASUREMENT RESULTS

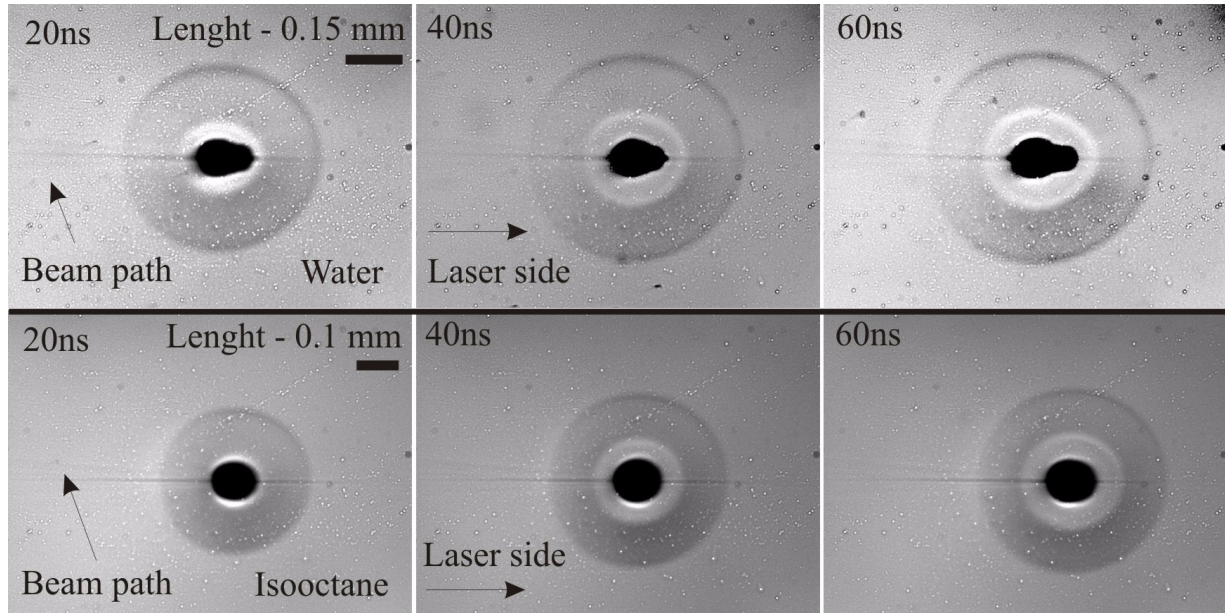


Fig.4.20 Initial stage of the shock wave propagation in water and in isoctane after 1 mJ - 6ns laser pulse.

phenomena were discussed in Chapter 3.2.2. The time history curves of the shock wave velocity and the shock wave position, corresponding to the measurement presented in Figure 4.20, are given in Figure 4.21. The curves are of the same character and both can be approximated by the function of the type

$$u_s = K_a \exp \frac{K_b}{t}, \quad (4.1)$$

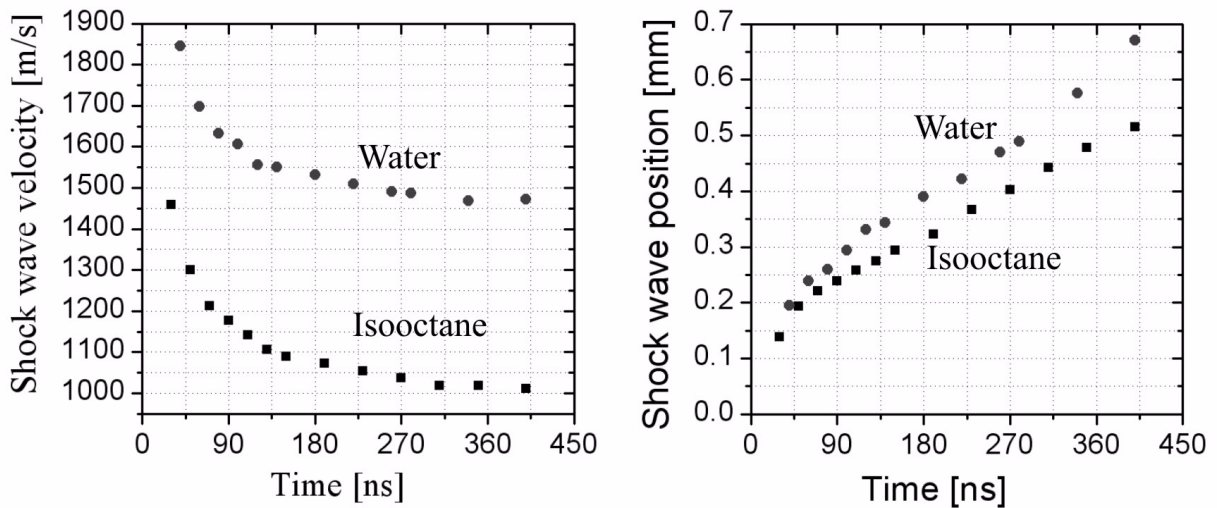


Fig.4.21 Shock wave velocity and shock wave position in water and in isoctane after 1 mJ - 6ns laser pulse.

where K_a and K_b are constants. The shock wave velocities tend to the speed of sound in the liquid due to the dissipation process and the spherical divergence $1/r$. More examples of the shock wave propagation are shown in Appendix E in Figure E1, Figure E2 and Figure E3.

4.3.3 Cavitation bubble collapse near a solid wall and in free liquid

The basic arrangement for the investigation of the bubble collapse was identical to the one described in Chapter 4.2.2, the schema of which is presented in Figure 4.6. The laser beam was focused close to an L-shaped profile representing a solid wall. The positioning of the bubble against the profile is shown in Figure 4.22. The bubble behaviour was recorded by the single-exposure method in the case of the solid wall and by the multi-exposure method in the case of free liquid.

In Figure 4.23 (right), the deformation of the bubble shape during the collapse from its maximum radius (Figure 4.23 - left) is presented. At the maximum radius the axis of symmetry of the bubble is parallel to the optical axis (horizontal) and there is no significant bubble behaviour, which could indicate the presence of the solid wall. However, when the bubble starts to contract the axis of symmetry of the bubble is reoriented perpendicularly to the solid wall. After that, a jet of liquid against the wall is formed and the bubble is accelerated towards the wall. When the bubble is fully attached to the wall, probably the jet reaction causes that the bubble is broken up. The time histories of the bubble radius with and without the solid wall are shown in Figure 4.24. Although the data quality is poor because of the bubble deformation, it shows no significant change in the bubble behaviour until the bubble collapse starts. After this point the behaviour is strongly different. All the figures of the measurement are presented in Appendix E in Figure E4.

The bubble collapse in the free liquid has already been presented in Figure 4.15 and in Figure 4.17. The measurements presented in Figure 4.25 were performed in order to show some other aspects of the bubble behaviour. The laser was set up to generate bubbles with the repeating frequency of 1Hz and at the energy level of about 1.5 mJ. These parameters were adjusted before

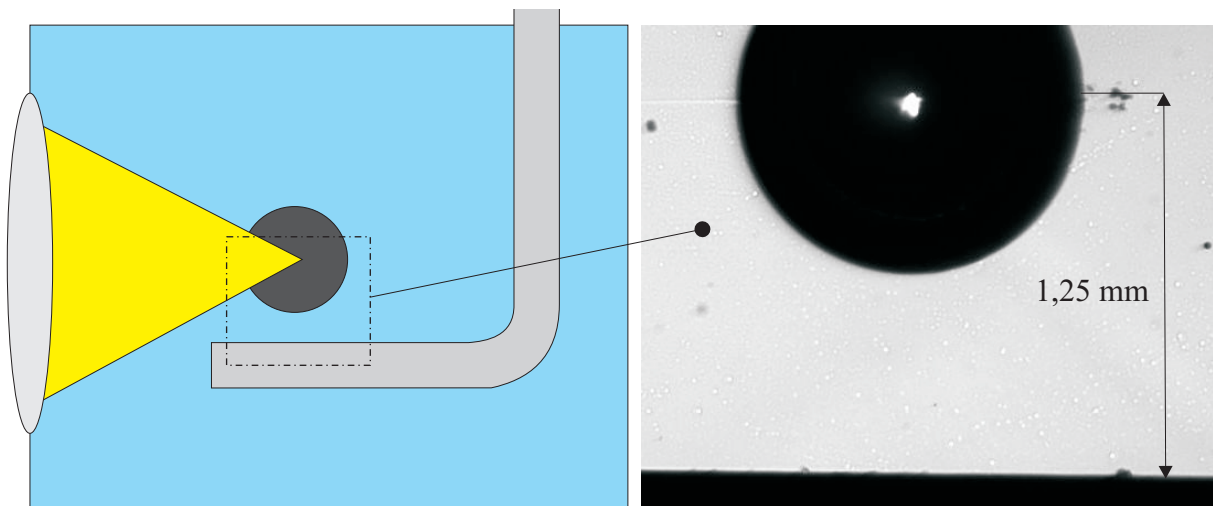


Fig.4.22 Experimental setup for investigation of cavitation bubble collapse near the solid wall.

4.3 EXPERIMENT AND MEASUREMENT - MEASUREMENT RESULTS

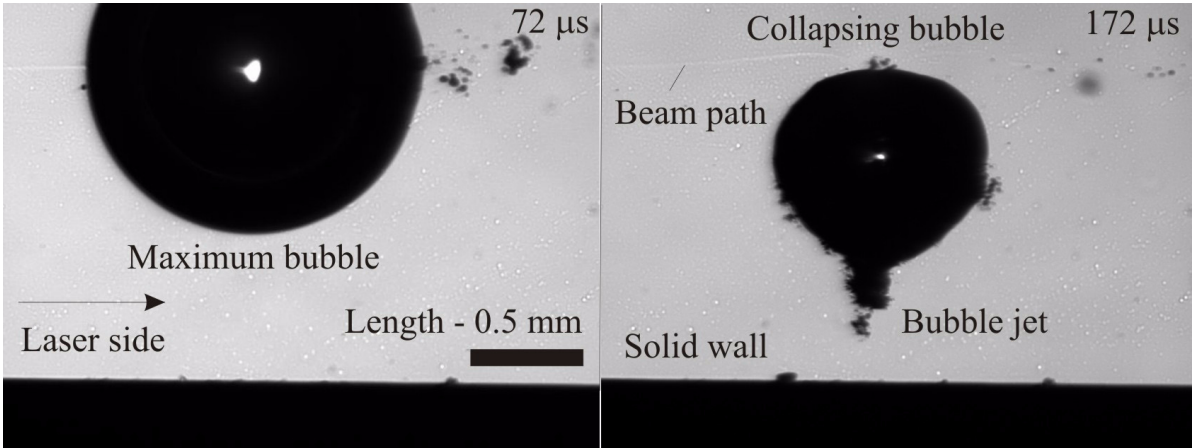


Fig.4.23 Cavitation bubble collapsing near the solid wall in water.

the measurements. Each bubble was photographed in three different positions; at the first maximum radius, at the second maximum radius and after the second collapse. During the collapse, the bubble surface was strongly deformed but the bubble was able to withstand some rebounds; then it broke up. This suggests that the bubble breakup against the solid wall during the first collapse is caused by the jet reaction. The axis of symmetry in the case of the bubble collapse in the free liquid has no preferable direction.

4.3.4 Cavitation bubble rising in glycerine

These measurements were realized in order to perform a simple test regarding the bubble content. The evaluation of the results is given in Chapter 5.2.5. It was found in the previous experiments that for a bubble in glycerine the bubble will not collapse after the first rebound but instead it will rise to the free surface. It is possible to calculate the density inside the bubble from the rising velocity using the balance of momentum.

The experimental setup was identical to the one presented in Chapter 4.2.2, the schema of which is shown in Figure 4.6. The temperature of glycerine was equal to the ambient temperature (21°C) and the energy output of the laser was approximately

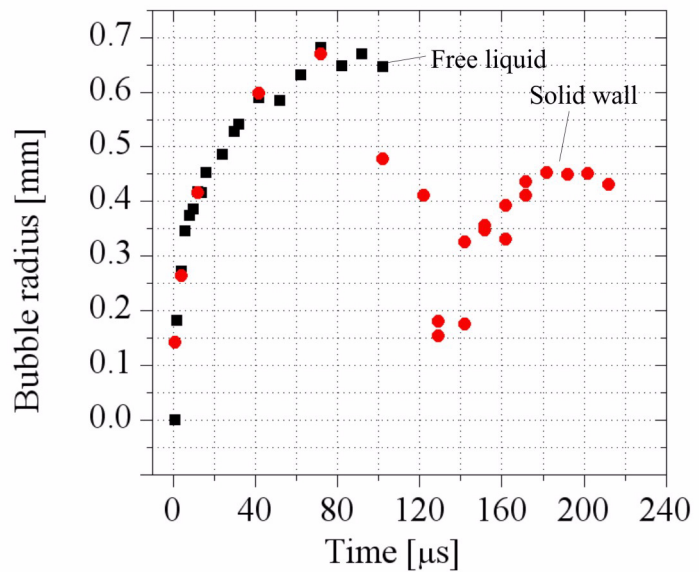


Fig.4.24 Time history of cavitation bubble radius in the free liquid and in the presence of solid wall in water.

4.3 EXPERIMENT AND MEASUREMENT - MEASUREMENT RESULTS

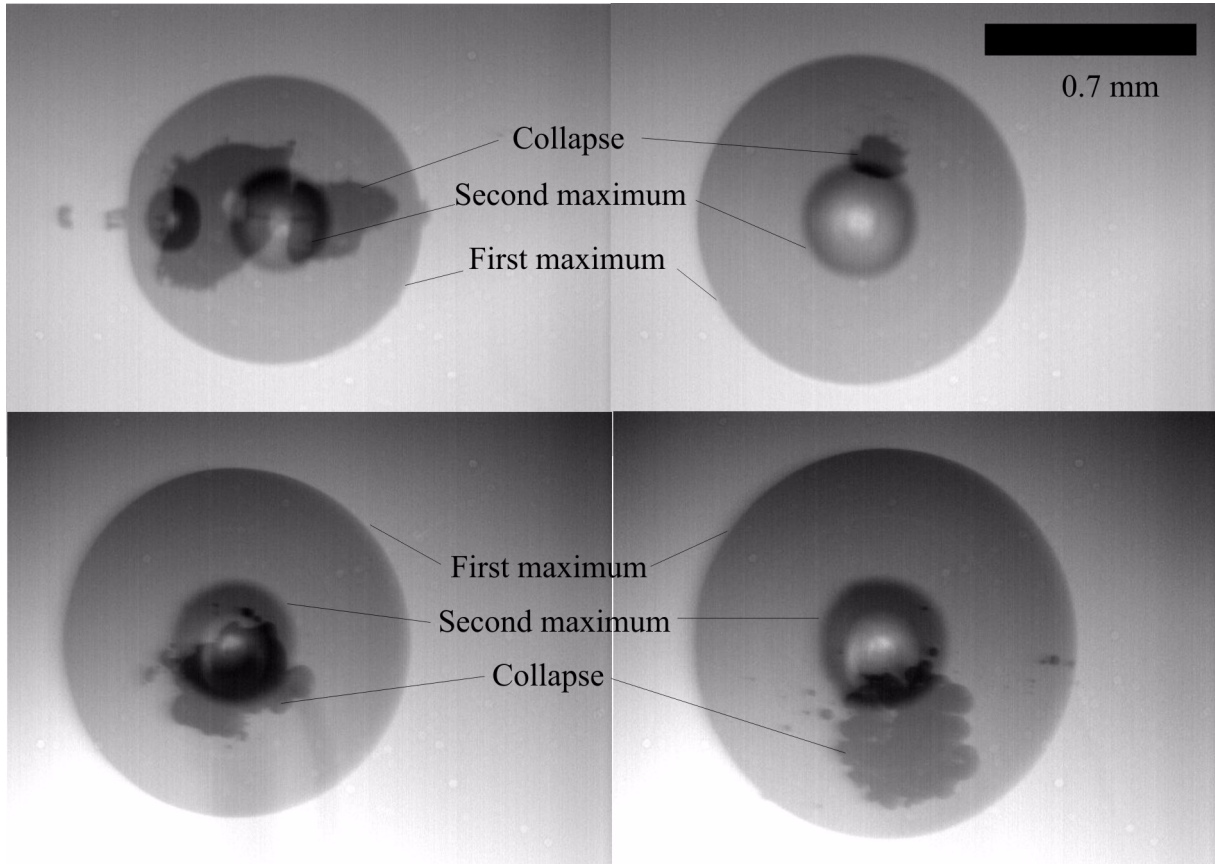


Fig.4.25 Cavitation bubble collapse in the free liquid.

3.8 mJ. The values of the bubble radius and the bubble velocity are the average values of three measurements. The bubble rising to the free surface is presented in Figure 4.27. The frames were recorded with the frequency 1Hz until the bubble was in the field of view of the camera. The radius of the bubble and the rising velocity changed in the first three seconds and then converged to constant values. The time histories of the bubble position and the bubble rising velocity are shown in Figure 4.27.

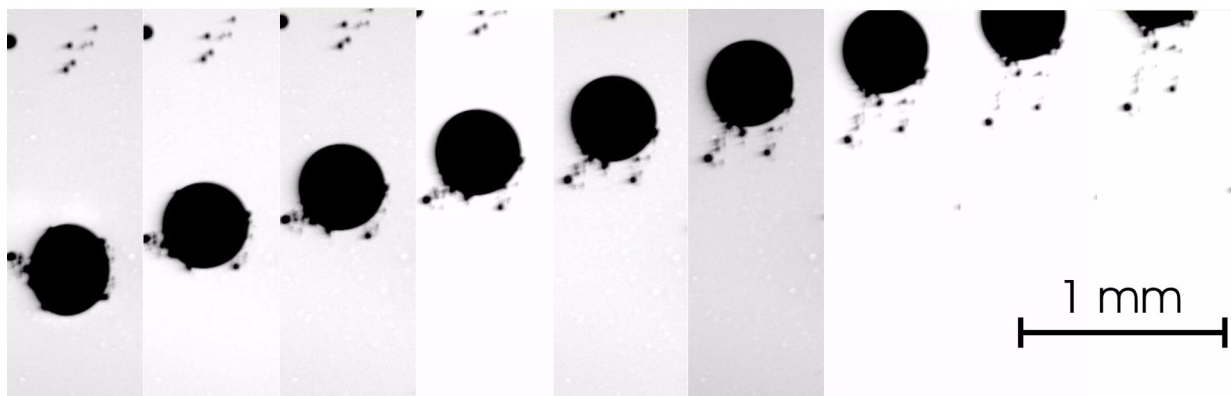


Fig.4.26 Bubble rising to the free boundary in glycerine.

4.4 Summary of the measurement results

This chapter summarizes the main results of the experimental measurements, some of which will be used as the basis for the creation of the physical model that will be used to determine the energy distribution during the oscillations of the bubble generated by the laser in water and in isooctane. The analysis of the results should also show the parameters that were not possible to obtain from the measurements and had to be calculated using a numerical method. The detail analyses of the results were given in the previous chapters.

The results of the measurements performed by the Tm-Yag laser, which are presented in Chapter 4.3.1, show that the bubble produced by this type of laser is strongly influenced by the presence of the optical fiber, which acts in principle like a solid wall. The bubble, generated by this way, is usually of oblong shape.

The results of the measurements performed by the Nd-Yag laser can be summarized as follows:

1) The measurements of the bubble oscillation and the shock wave propagation in water and isooctane, which are presented in Chapter 4.3.2, show strongly different oscillations of the bubble radii in the two liquids. The time histories of the bubble radii $R(t)$ in the liquids are shown in Figure 4.19, the main parameters of which are presented in Table 4.1. It is obvious that for the same level of laser energy, the first maximum bubble radius in water is smaller than the one in isooctane and also that the second maximum bubble radius is bigger in isooctane than in water.

The curves of the shock wave propagation in both liquids show no significant differences. The time histories of the shock wave velocity $u_s(t)$ and the shock wave position $r_s(t)$ in both liquids are shown in Figure 4.21.

These results provide all the parameters necessary for the calculation of the energy distribution of the laser pulse, except that the pressure-time profile at a fixed position $p(t)_{R=konst}$, which is required for the calculation of the shock wave energy, has to be calculated using an appropriate numerical model.

2) The investigation of the cavitation bubble collapse in water described in Chapter 4.3.3 shows that the presence of the solid wall strongly influences the bubble behaviour. The presence of the solid wall has no influence on the bubble behaviour during the first expansion but it influences the bubble dynamics when the bubble collapses. From this measurement, which is represented in Appendix E in Figure E4, the values of the maximum bubble radius and the distance of the bubble from the solid wall are obtained. These parameters are used in the numerical simula-

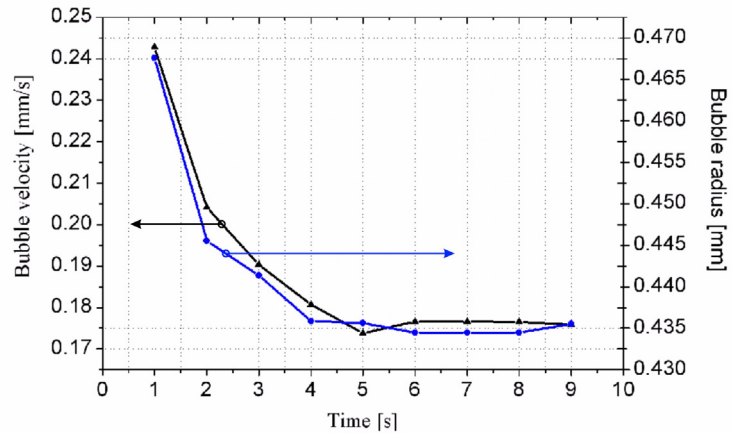


Fig.4.27 Time history of radius and rising velocity of the bubble rising to the free boundary in glycerine.

4.4 EXPERIMENT AND MEASUREMENT - SUMMARY OF THE MEASUREMENT RESULTS

tion of the bubble deformations during the collapse using the CFD code Fluent.

3) From the measurement of the cavitation bubble rising in glycerine, which is presented in Figure 4.27, it follows that the bubble oscillations in glycerine are damped by the liquid viscosity in the very early stage and the bubble rises to the free surface without a collapse. This measurement gives the value of the ultimate rising velocity, which is used for the calculation of the density inside the bubble.

Medium	Water	Isooctane
Maximum plasma size	0.021 mm	0.019 mm
First maximum bubble radius	0.75 mm	1 mm
Second maximum bubble radius	0.27 mm	0.77 mm
Laser input energy	1 mJ	1 mJ
Pulse duration	6 ns	6 ns

Table 4.1 Summary of experimental results required for numerical simulation.

5. PROBLEM SOLUTION

In this chapter, the model of behaviour of a laser-induced cavitation bubble and the models describing the propagation of the shock waves produced during the bubble growth and collapse in liquid are introduced. In the first section, a procedure, which enables the integration of the plasma dynamics into the cavitation bubble model as the initial and boundary condition, is introduced. The bubble radius in the initial stages is modelled as an envelope of plasma, which is produced by a beam with \sin^2 intensity profile. The used differential equation of the bubble dynamics considers viscous compressible liquid with the influence of surface tension and with boundary conditions respecting the absorption of laser energy by the liquid. For the calculation of the pressure and the velocity fields in the liquid around the bubble, a modified method of characteristics is derived, which is required for the evaluation of the shock wave propagation. Note that the derived method of characteristics does not take into account dissipation processes. In order to relieve the shortage, the dissipation effects are introduced using another model. This semi-empirical model uses the initial conditions from the solution of the shock wave propagation without dissipation (the method of characteristics). The models should enable the calculation of the energy distribution of the laser pulse energy.

5.1 General strategy

In order to determine the fractions, into which the energy E_{La0} of the laser pulse is divided, estimation from the data obtained from the experiment has to be made. Some hypothetical curves of the bubble radius evolution and the shock wave propagation, which will be used in the follow-

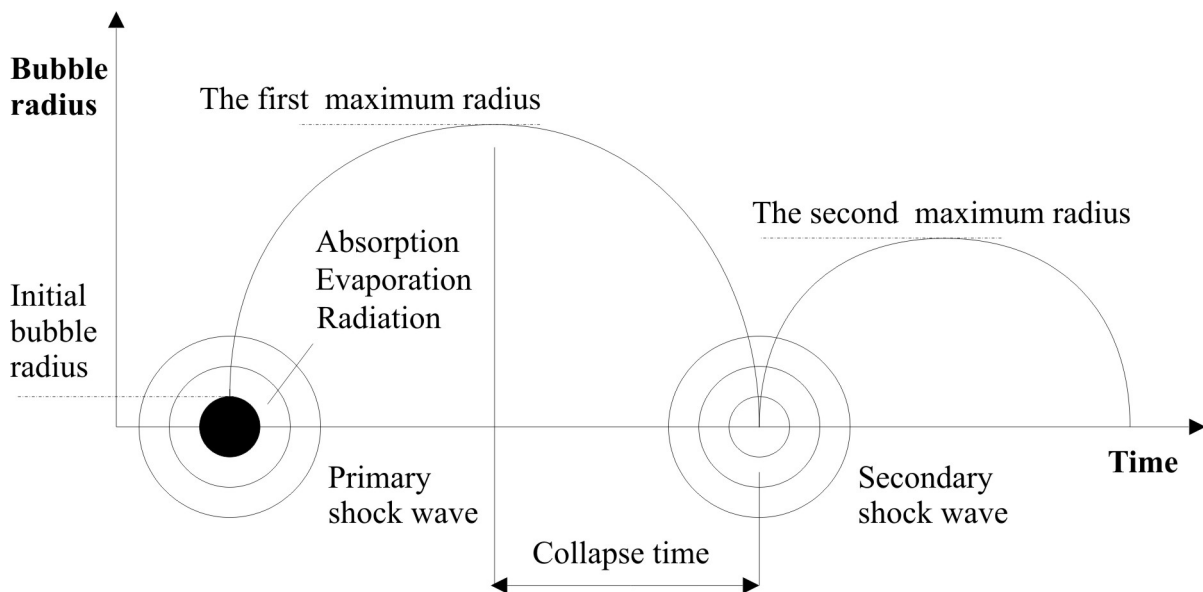


Fig.5.1 Typical curve of the bubble radius evolution.

5.1 PROBLEM SOLUTION - GENERAL STRATEGY

ing considerations, are shown in Figure 5.1 and Figure 5.2. At the beginning, when the laser light is focused into the liquid, the absorbed part of the laser energy is consumed for plasma creation and another part of the energy goes through the focal region and does not influence the process in the following time. When the plasma is created in the focal region, it causes the rapture of the liquid and its evaporation. During the plasma growth, a part of the laser energy is also radiated. The initial bubble behaviour during this time is determined by the plasma dynamics described in Chapter 3.2.2. The bubble in these initial states could be illustrated as the plasma envelope formed by the evaporated layer of liquid around it. When the plasma increases to its maximum radius and starts to contract, the value of this maximum radius can be used as the initial bubble radius in the bubble dynamics model, which is then used for the subsequent calculation. Because the plasma attains very high velocities, a primary shock wave is generated. A hypothetical velocity profile of the shock wave is shown in Figure 5.2. It is necessary to note that the profile represents the velocity of movement of the pressure peak but not the time profile of the shock wave, which is needed for the shock wave energy evolution. Such a profile can be visualized by a sensor fixed at one place in the liquid while the shock wave is passing. In the very early stage the plasma is closely enveloped by the evaporated liquid (bubble) and the bubble is enveloped by the shock wave. The calculation in this stage is thus divided into three processes; the plasma dynamics cal-

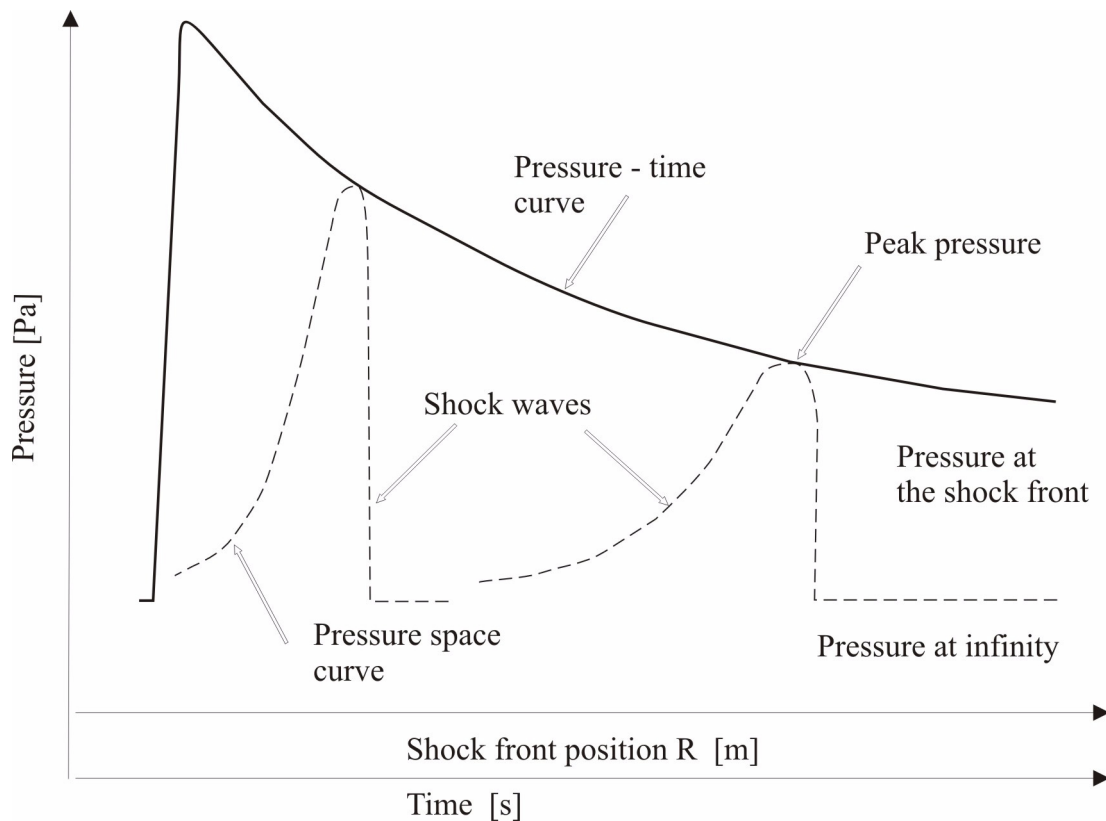


Fig.5.2 Typical curve of the shock wave propagation. The solid line represents the time propagation of pressure at the head of the shock front. The dashed lines are the space profiles of the shock wave at two different time positions.

ulation, which gives the initial values for the bubble dynamics calculation, which further provides initial conditions for the shock wave calculation. The pressure and velocity fields in the liquid surrounding the bubble would have to be solved at every position of the bubble wall in order to obtain the shock wave profile in the whole region. Collecting the data for one fixed place, one can obtain the time profile of the shock wave, which is necessary for the shock wave energy determination. After leaving the plasma state, the bubble grows to its maximal radius and a violent contraction follows. Due to the high temperatures and pressures during the collapse, a secondary shock wave is produced. The initial conditions for the calculation of the shock wave propagation are given by the solution of the bubble dynamics as in the case of the primary shock wave. After that the bubble expands to the second maximal radius. Note that in an ideal case the energy lost between the first bubble compression and the second bubble expansion could be consumed purely for the shock wave generation.

5.2 Physical model

5.2.1 Plasma growth modelling

A direct modelling of temporal and spatial distribution of plasma is complicated and depends strongly on the pulse duration. To avoid this, the plasma has to be simulated indirectly by the growing equilibrium bubble radius, as used e.g. by Vogel [23]. First, the restriction introduced in Chapter 3.2.2 is considered, i.e. the plasma growth is only time-dependent, because the pulse length is much longer than the focal region. The simulation will start at an initial equilibrium bubble radius $R_0 = R_{0a}$, which will be identical to the maximum plasma size detected from the experiment. During the pulse, this equilibrium radius will grow to a final value R_{0b} , which will be obtained by a test simulation, in which the first maximum bubble radius detected from the experiment will be reached. The power deposited by laser into the liquid for the Gaussian beam is given by Eqs. (3.26) and (3.27). Suppose that the laser power during the pulse can be simulated by \sin^2 instead of the Gaussian function:

$$P_{La}(t) = P_{La0} \sin\left(\frac{\pi}{2\tau_{La}}t\right)^2, \quad 0 < t < 2\tau_{La}, \quad (5.1)$$

where P_{La0} is the initial laser power and τ_{La} is the full width at half of the pulse maximum. The laser energy during the pulse can be obtained by integration of P_{La0} as

$$E_{La}(t) = \int_0^t P_{La0} \sin\left(\frac{\pi}{2\tau_{La}}t\right)^2 dt = P_{La0} \left(\frac{t}{2} + \frac{\tau_{La}}{2\pi} \sin\left(\frac{\pi}{2\tau_{La}}t\right) \right). \quad (5.2)$$

The value of P_{L0} is obtained from Eq. (5.2) by replacing t by $2\tau_p$ as

$$E_{La0} = P_{La0} \tau_{La}, \quad (5.3)$$

5.2 PROBLEM SOLUTION - PHYSICAL MODEL

where E_{L0} is the total energy delivered by laser. Suppose that the bubble equilibrium volume during the laser pulse is proportional to the laser energy as

$$V_0(t) = kE_{La}(t) = \frac{4}{3}\pi(R_0^3(t) + R_{0a}^3). \quad (5.4)$$

For the total laser energy delivered by laser the volume then follows the relation

$$V_0 = kE_{La0} = \frac{4}{3}\pi(R_{0b}^3(t) + R_{0a}^3). \quad (5.5)$$

By combining Eqs. (5.3) and (5.4) and having imposed the resulting term into Eq. (5.2) together with Eq. (5.5), the expression for the evolution of the equilibrium bubble radius during the laser pulse is obtained as

$$R_0(t) = \left(R_{0a}^3 + \frac{R_{0b}^3(t) - R_{0a}^3}{2\tau_{La}} \left[t + \frac{\tau_{La}}{\pi} \sin\left(\frac{\pi}{\tau_{La}}t\right) \right] \right)^{\frac{1}{3}}, \quad (5.6)$$

which can be directly used in the equation of the cavitation bubble dynamics.

5.2.2 Application of the compressible model of the bubble dynamics

As it was introduced in Chapter 3.3 and derived in Appendix B, the Gilmore cavitation bubble model has the following form

$$\frac{R}{C} \frac{dH}{dt} \left(1 - \frac{\dot{R}}{C}\right) + H \left(1 - \frac{\dot{R}}{C}\right) - r \frac{d\dot{R}}{dt} \left(1 - \frac{\dot{R}}{C}\right) - \frac{3\dot{R}^2}{2} \left(1 - \frac{\dot{R}}{C}\right) = 0, \quad (5.7)$$

The capital letters were used instead of $r = R$, $u = dR/dt$, $h = H$ and $c = C$ to denote the values of the quantities at the bubble wall. The values of C and H can be evaluated by using an appropriate state equation. For liquids, Tait's equation (see Appendix D) is the most used and takes the form

$$\frac{p + B}{p_\infty + B} = \left(\frac{\rho}{\rho_\infty} \right)^n, \quad (5.8)$$

where n and B are the equation parameters. The value of B depends on temperature and neglecting this factor leads to neglecting dissipation in the equation. If this equation is introduced into Eq. (3.57) and the resulting equation is integrated in the limits from p_∞ to p_R , the explicit relation for enthalpy at the bubble wall is obtained as

5.2 PROBLEM SOLUTION - PHYSICAL MODEL

$$H = \int_{p_\infty}^{p_R} \left(\frac{p+B}{p_\infty+B} \right)^{\frac{-1}{n}} \frac{1}{\rho_\infty} dp = \frac{n(p_\infty+B)}{(n-1)\rho_\infty} \left[\left(\frac{p_R+B}{p_\infty+B} \right)^{\frac{n-1}{n}} - 1 \right]. \quad (5.9)$$

The local speed of sound at the bubble wall is obtained from the definition (3.52) by introducing (5.8) as

$$C = c_\infty^2 \left(\frac{p_R+B}{p_\infty+B} \right)^{\frac{n-1}{n}}. \quad (5.10)$$

The pressure at the bubble wall can be obtained from the momentum flux across the bubble surface given by Eqs. (A.6) and (A.7), which results in relation

$$p_R = p_B - \frac{2\sigma}{R} + 2\mu \left. \frac{\partial v}{\partial r} \right|_R, \quad (5.11)$$

where p_B is the pressure inside the bubble, σ is surface tension and μ is dynamic viscosity. The derivative introduced in Eq. (5.11) can be evaluated from Eqs. (B.1) and (B.8) as

$$p_R = p_B - \frac{2\sigma}{R} - \frac{4\mu\dot{R}}{R} - \frac{4\mu\dot{R}dH}{3C^2 dR}. \quad (5.12)$$

The last term on the left-hand side of Eq. (5.12) is usually of small importance and can be neglected. To complete the system of equations for bubble dynamics it is necessary to express explicitly the pressure p_B of the bubble contents. It is assumed that the mixture of gas and vapour inside the bubble can be treated as an ideal gas and the vapour pressure is constant for the given liquid temperature. The pressure inside the bubble can be expressed as

$$p_B = p_v + p_{g0} \left(\frac{R_0}{R} \right)^{3\gamma}. \quad (5.13)$$

The solution of the differential equation for the bubble radius (5.7) requires two initial conditions. The first initial condition is the initial bubble radius at time $t = 0$ and the second condition is the bubble wall velocity at the same time. However, these conditions are already given by Eq. (5.6), which represents the evaluation of the equilibrium bubble radius R_0 in Eq. (5.13). From this point of view, the initial bubble radius for the solution of Eq. (5.7) is R_{ba} introduced by Eq. (5.4). Since the initial plasma velocity is considered to be zero, the initial conditions can be used in the form $R(0) = R_{ba}$ and $dR(0)/dt = 0$.

5.2.3 Pressure and velocity fields in the liquid surrounding the bubble

The equations describing the pressure and velocity fields in the liquid surrounding the bubble can be obtained from the continuity (A.8) and momentum equation (A.10) as follows: The Kirkwood-Bethe hypothesis introduced in Chapter 3.4 states that the kinetic enthalpy $Y(r;t)$ defined by Eq. (3.79) is constant along any path moving with the velocity $c + v$. If the dissipative effects can be neglected, the relations introduced in Eqs. (B.7) and (B.8) can be used to transform the system into the following form

$$\frac{1}{c} \frac{dh}{dt} = -c \frac{\partial v}{\partial r} - \frac{2vc}{r}, \quad (5.14)$$

$$\frac{dv}{dt} = -\frac{\partial h}{\partial r}. \quad (5.15)$$

This system of equations has the same characteristics as the system derived in Appendix C for the original Euler equations. Note that the solution of the system of partial differential Eqs. (5.14) and (5.15) can be transformed into the solution along the characteristic line $Dr/Dt = c + v$, in order to obtain a system of ordinary differential equations. In this concept, the kinetic enthalpy $Y(r;t)$ represents the characteristic variable. The operator representing the derivative along the outgoing characteristic moving outwards with the velocity $c + u$ is

$$\frac{D}{Dt} = \frac{\partial}{\partial t} + (c + v) \frac{\partial}{\partial r}. \quad (5.16)$$

Note that the operator used in the previous derivatives

$$\frac{d}{dt} = \frac{\partial}{\partial t} + v \frac{\partial}{\partial r} \quad (5.17)$$

is associated with the coordinate frame moving with the particle velocity v . Multiplying Eq. (5.14) by c and introducing the operator (5.17) into this equation and after using Eq. (5.15) on the right side of Eq. (5.14) we obtain

$$-\frac{1}{c} \left(\frac{\partial h}{\partial t} + v \frac{\partial h}{\partial r} + c \frac{\partial h}{\partial r} \right) = \frac{2vc}{r} + \left(\frac{\partial v}{\partial t} + v \frac{\partial v}{\partial r} + c \frac{\partial v}{\partial r} \right). \quad (5.18)$$

If the operator (5.16) is used to express the derivatives Dh/Dt and Dv/Dt , the formula for integration along the outgoing characteristic can be obtained as

$$-\frac{1}{c} \frac{Dh}{Dt} = \frac{2vc}{r} + \frac{Dv}{Dt}. \quad (5.19)$$

5.2 PROBLEM SOLUTION - PHYSICAL MODEL

Applying the operator (5.16) to the quantity $Y(r,t)$ defined by Eq. (3.79) gives

$$\frac{Dh}{Dr} = -\frac{Y}{r^2} - v\frac{Dv}{Dr}. \quad (5.20)$$

Eq. (5.20) can be used to eliminate the derivative Dh/Dr from Eq. (5.19), which can be finally solved for the derivative Dv/Dr as

$$\frac{Dv}{Dr} = \frac{c+v}{c-v} \left[(c+v)\frac{Y}{r^2} - \frac{2vc^2}{r} \right]. \quad (5.21)$$

Note that the equation of the characteristic line is expressed by

$$\frac{Dr}{Dt} = c + v, \quad (5.22)$$

which also gives the relation between the differentials Dr and Dt . A similar equation for the pressure propagation along the outgoing characteristic can be obtained as

$$\frac{Dp}{Dr} = \frac{\rho_0(c+v)}{r(c-v)} \left(\frac{p+B}{p_\infty+B} \right)^{\frac{1}{n}} \left[2v^2c^2 - c(c+v)\frac{Y}{r} \right] \quad (5.23)$$

if the kinetic enthalpy definition (3.79) is used to eliminate the derivative Dv/Dr from Eq. (5.19) and the enthalpy h is expressed from Eq. (5.9), in which the pressure p_R at the bubble wall is replaced by the pressure p . The system of Eqs. (5.21), (5.22) and (5.23) represents the complete system of equations for the solution of the pressure and velocity at each point in the (r,t) space. The solution of Eqs. (5.21) and (5.23) gives the pressure and velocity distribution along each characteristic, whose time coordinate is given by Eq. (5.22). The system of Eqs. (5.21) and (5.22) or (5.22) and (5.23) requires two boundary conditions, which result from the solution of Eq. (5.7), because each outgoing characteristic starts at the bubble surface. At each position of the bubble radius in each time t_B , the values H , C , R , dR/dt and p_R are given. These values also determine the kinetic enthalpy $Y = R(0.5\dot{R}^2 + H)$, which represents a constant during the calculation. Note that the time t_B is used in Eq. (5.22). The knowledge of the pressure and velocity distribution in the liquid surrounding the bubble is used in the calculation of the shock wave energy and supports the experimental data especially close to the plasma centre, where no results have been obtained because of the experiment resolution.

5.3 Energy distribution

5.3.1 Shock wave energy

One way to express the shock wave energy is using the work done by the shock wave pressure on a surface fixed in the fluid at the position r_s . In a non-viscous liquid the work-energy principle can be written as

$$E_s = 4\pi \int_{t(r_s)}^{\infty} r^2 v(p(t) + p_0) dt, \quad (5.24)$$

where $p(t)$ is the pressure in excess of the hydrostatic pressure p_0 and vdt is the displacement of fluid in time dt . First, the particle velocity v has to be eliminated from the integral using the Rankine-Hugoniot conditions at the shock front, which is given by Equation (3.73). If the integral is evaluated for the constant radius $r = r_s$, the resulting expression for the shock wave energy can be written as

$$E_S = \frac{4\pi r_s^2}{\rho_0} \int_{t(r_s)}^{t_\infty} \frac{(p(t) - p_0)^2}{u_s} dt. \quad (5.25)$$

In the liquid far from the bubble, the term (3.66) can also be used to express the particle velocity in Equation (5.25), which results in

$$E_S = \frac{4\pi r_s^2}{\rho_0 c_0} \int_{t(r_s)}^{t_\infty} (p(t) - p_0)^2 dt, \quad (5.26)$$

where the after-flow term was neglected. The shock wave energy can also be expressed from the total energy flux across the surface r_s as

$$E_S = \frac{4\pi r_s^2}{\rho_0} \int_{t(r_s)}^{t_\infty} \rho v \Delta \left(\varepsilon + \frac{1}{2} v^2 + \frac{p}{\rho} \right) dt, \quad (5.27)$$

where $\Delta(\varepsilon + 0.5v^2)$ is the increase in internal and kinetic energy for unit mass of fluid over the values in undisturbed fluid. If the exact result of the integral (5.27) is evaluated using the Rankine-Hugoniot conditions (3.72)-(3.74) it gives

5.3 PROBLEM SOLUTION - ENERGY DISTRIBUTION

$$E_S = \frac{4\pi r_s^2}{\rho_0} \int_{t(r_s)u_s}^{t_\infty} \frac{(p(t) - p_0)^2}{u_s \rho_0} dt. \quad (5.28)$$

Note that except for very high pressures the difference between the integrals (5.25) and (5.28) is small. The pressure time curve $p(t)$ can be obtained from the solution of the pressure field by collecting the pressure data at the fixed position r_s , however, direct application of the calculated curve is not convenient. For this reason, the curve is approximated by the following function, which has the form suitable for calculation:

$$p(t) = (p_s(r_s) - p_\infty) \exp\left[\frac{-t \ln 2}{\tau_s}\right]. \quad (5.29)$$

The relation between the calculated profile and the pressure time profile given by Eq. (5.29) is the full width at half maximum of the pulse (FWAHM) τ_s .

5.3.2 Cavitation bubble energy

The energy for the bubble growth from the initial radius R_{a0} to its maximum radius R_{max} can be expressed from the work done by the pressure inside the bubble against the liquid pressure p_∞ as

$$E_{max} = \int_{R_0}^{R_{max}} 4\pi R^2 (p_\infty - p_v) dR = \frac{4\pi(p_\infty - p_v)}{3} [R_{max}^3 - R_0^3] \cong \frac{4\pi(p_\infty - p_v)}{3} R_{max}^3. \quad (5.30)$$

The equation was derived without considering the effects of liquid viscosity, compressibility and surface tension and the minimum and maximum bubble radii were obtained from the experimental measurements. Note that the maximum bubble radius R_{max} and the bubble collapse time $\tau_{collapse}$ are related by Eq. (3.50). The energy of the bubble growth to its maximum radius can also be utilized for the calculation of the energy of the secondary shock wave generated between the first bubble contraction and its secondary expansion. Using the last form of Eq. (5.30), the energy of the secondary shock wave can be expressed as

$$E_{1shock} = E_{1max} - E_{2max} = \frac{4\pi(p_\infty - p_v)}{3} (R_{1max}^3 - R_{2max}^3) \quad (5.31)$$

Although this equation neglects the dissipation effects, it can be used as the first estimation of the secondary shock wave energy.

5.3.3 Energy of evaporation of the bubble content

It is assumed that the liquid of the volume $4/3\pi R_{0a}^3\rho_\infty$ determined by the maximum plasma diameter R_{0a} is fully evaporated. The heat conduction and the bubble volume changes are not taken into account. The influence of heat conduction can be neglected due to short time duration of the plasma event, which is of the order of nanoseconds. As it has been shown e.g. by Franc[34], the characteristic time required for heat transfer in the case of a water-air system is several microseconds. The energy necessary for heating the liquid volume of the radius R_{0a} to the evaporation temperature T_{evap} , sequential evaporation and the heating to the final temperature of vapour T can be written in the following form:

$$E_{evap} = \frac{4}{3}\pi R_{0a}^3\rho_\infty(T_{evap} - T_L)c_{vL} + \frac{4}{3}\pi R_{0a}^3\rho_\infty h_v + \frac{4}{3}\pi R_{0a}^3\rho_\infty(T - T_{evap})c_{vV}, \quad (5.32)$$

where h_{Lv} is the evaporation heat for water, T_L is the initial liquid temperature and c_{vL} and c_{vV} are the specific heats at constant volume in water and in vapour. The evaporation heat generally depends on pressure but for the calculations it is sufficient to use its constant value $h_{Lv} = 1707 \text{ kJ.kg}^{-1}$.

5.3.4 Energy radiated by plasma

As it has been shown by several authors, e.g. Barnes [45], the radiation of plasma in the wavelength range from 300 to 900 nm can be calculated using actuation of a grey body radiator. According to the model, the radiated energy depends on the plasma temperature T_p , plasma surface S_p and duration of plasma radiation τ_p as

$$E_p = \varepsilon\sigma S_p T_p^4 \tau_p, \quad (5.33)$$

where $\sigma = 5.67 \times 10^{-8} \text{ Wm}^{-2}\text{K}^{-4}$ is the Stefan-Boltzman constant and ε is emissivity. The value $\varepsilon = 1$ corresponds to a blackbody radiator, which represents maximal energy, which could be radiated. The plasma temperature can be calculated using Wien's displacement law as

$$T_p = 1.7 \times 10^{-9} \vartheta_{max}, \quad (5.34)$$

if the spectral distribution is known from the measurement. Because no such data have been obtained from the performed measurements, the value of the plasma temperature will be taken from the literature [9] to be 6500 K.

5.4 Semi-empirical solution of the shock wave propagation

The semi-empirical model of the shock wave propagation, which will be presented in this chapter, was originally developed by Brinkley and Kirkwood [40] for the investigation of the underwater explosions. In the following paragraphs the model will be rederived and supple-

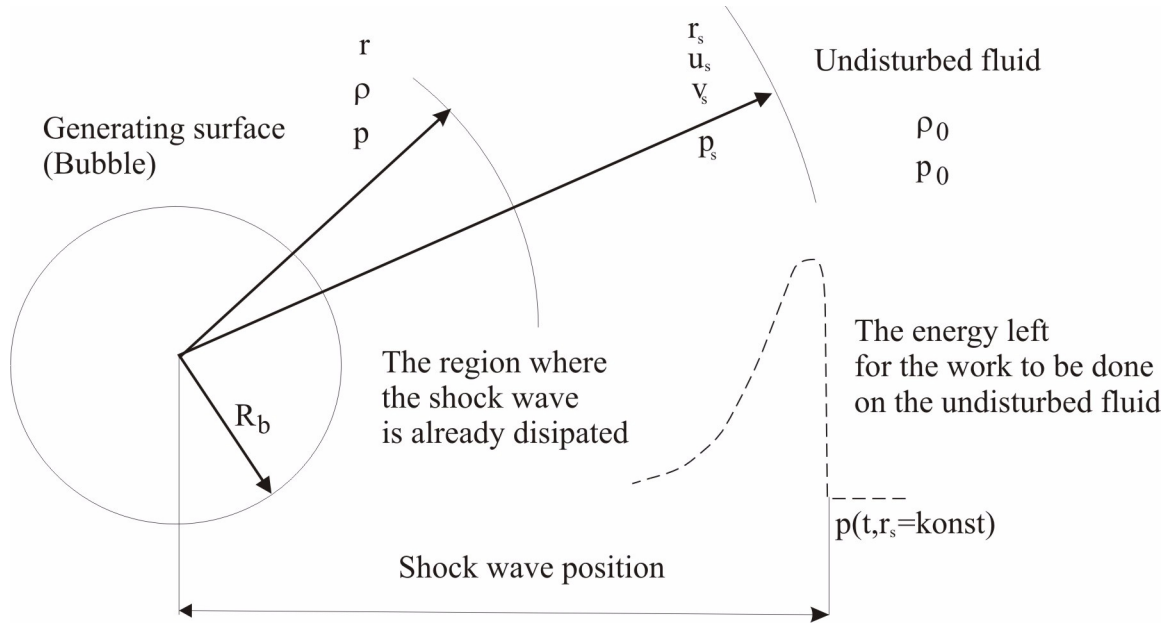


Fig.5.3 The shock wave generated by the bubble surface.

mented by an explicit formulation of the energy dissipated at the shock wave. The aim of the derivation is to find out how the pressure peak p_s varies with the shock wave position r_s . The considered problem, which is illustrated in Figure 5.3, can be described using the continuity and momentum equations (A.8) and (A.10). For the application of the equations for the case of the shock wave it is more convenient to transform the equations into the coordinate frame associated with the shock wave at the position r_s . After elaborating the transformations (see e.g. [41]) the equations take the form

$$\frac{\rho r^2}{\rho_0 r_s^2} \left(\frac{dv}{dr_s} \right) + \frac{1}{\rho c^2} \left(\frac{\partial p}{\partial t} \right) + \frac{2v}{r} = 0, \quad (5.35)$$

$$\frac{r_s^2}{r^2} \frac{dv}{dt} - \frac{1}{\rho_0} \left(\frac{\partial p}{\partial r_s} \right) = 0. \quad (5.36)$$

If the system of equations is specialized for the shock wave, it results in

$$\frac{\rho}{\rho_0} \left(\frac{dv_s}{dr_s} \right) + \frac{1}{\rho c^2} \left(\frac{\partial p_s}{\partial t} \right) + \frac{2v_s}{r_s} = 0 \quad (5.37)$$

$$\frac{dv_s}{dt} - \frac{1}{\rho_0} \left(\frac{\partial p_s}{\partial r_s} \right) = 0. \quad (5.38)$$

5.4 PROBLEM SOLUTION - SEMI-EMPIRICAL SOLUTION OF THE SHOCK WAVE PROPAGATION

Eqs. (5.37) and (5.38) together with the Rankine-Hugoniot conditions (3.72)-(3.74) may be regarded as a system of partial differential equations and boundary conditions for the derivatives $\partial p_s/\partial t$, $\partial p_s/\partial r_s$, $\partial v_s/\partial t$ and $\partial v_s/\partial r_s$. If it is possible to find two more equations to supplement the system, each of the derivatives can be expressed as a function of the pressure p_s and the position r_s . The third equation can be obtained from the Rankine-Hugoniot conditions by applying the operator

$$\frac{d}{dt} = \frac{\partial}{\partial t} + u_s \frac{\partial}{\partial r_s}, \quad (5.39)$$

in which the shock wave is stationary. At the shock wave, using the operator (5.39), the following expression is valid

$$\frac{dv_s}{dt} = \frac{dv_s dp_s}{dp_s dt} = \frac{\partial v_s}{\partial t} + u_s \frac{\partial v_s}{\partial r_s} = \frac{dv_s}{dp_s} \left(\frac{\partial p_s}{\partial t} + u_s \frac{\partial p_s}{\partial r_s} \right). \quad (5.40)$$

The derivative $\partial v_s/\partial p_s$ can be expressed from the principle of momentum conservation at the shock wave $p_s = \rho_0 v_s u_s$ as

$$1 = \frac{p_s du_s}{u_s dp_s} + \rho_0 u_s \frac{dv_s}{dp_s}. \quad (5.41)$$

This formula can then be used to eliminate the mentioned derivative from Eq. (5.40) yielding

$$\frac{dv_s}{dt} + u_s \frac{\partial v_s}{\partial r_s} - \frac{g}{\rho_0} \frac{\partial p_s}{\partial r_s} - \frac{g}{u_s \rho_0} \frac{\partial p_s}{\partial t} = 0, \quad (5.42)$$

where

$$g = \rho_0 u_s \frac{dv_s}{dp_s} = 1 - \frac{p_s du_s}{u_s dp_s}. \quad (5.43)$$

As the solution should result in an equation for the peak pressure p_s varying with the distance r_s , another equation needed to close the system of Eqs. (5.37), (5.38) and (5.42) has been obtained by the authors from the energy decay at the shock wave along the coordinate r_s . The work done by the shock wave after it passes the position r_s is ultimately dissipated as heat increasing the internal energy. It means that a portion of the shock wave energy, before it has reached the position r_s , had already been dissipated as heat. This principle can be written as

5.4 PROBLEM SOLUTION - SEMI-EMPIRICAL SOLUTION OF THE SHOCK WAVE PROPAGATION

$$E_s = 4\pi \int_R^{r_s} \rho_0 r^2 \varepsilon[p_s(r)] dr + 4\pi \int_{t(r_s)}^{\infty} r^2 v(p(t) + p_0) dt, \quad (5.44)$$

where the first integral is the increase of the internal energy per unit mass and the second integral represents the work energy principle, where p is the pressure in excess of the hydrostatic pressure and is evaluated at a constant position. Using the enthalpy definition $h_{dis} = \varepsilon + p_0 \Delta(1/\rho)$, Eq. (5.44) can be transformed into the form (see e.g. [41])

$$E_s = 4\pi \int_R^{r_s} \rho_s r_s^2 h_{dis}(p_s(r_s)) dr_s + 4\pi \int_{t(r_s)}^{\infty} r^2 v p(t) dt + p_0 \Delta V_B, \quad (5.45)$$

where ΔV_B is the energy stored in the liquid by the bubble expansion. When the integration limits are changed, this equation gives two different formulations of the shock wave energy

$$E_s = 4\pi \int_R^{\infty} \rho_s r_s^2 h_{dis}(p_s(r_s)) dr_s = 4\pi \int_{t(R)}^{\infty} r^2 v p(t) dt, \quad (5.46)$$

which may be regarded simply as the expression of the principle of energy conservation for the shock wave. The reduction of the time integral in Eq. (5.46) provides the means for introducing an empirical approximation into the model. The energy position curves observed in the experiments usually have the form $p_s r_s^2 u_s \exp(-t/\mu)$. Having used the logarithmic slope of the curve, the fourth relation between the derivative is obtained in the form

$$\frac{1}{p_s} \frac{\partial p_s}{\partial t} + \frac{1}{v_s} \frac{\partial v_s}{\partial t} + \frac{2v_s}{r_s} = -\frac{1}{\mu}. \quad (5.47)$$

If the time integral in Eq. (5.43) is normalized over the reduced time including the value of μ , it represents the shape of the shock wave. The integral is normalized to the initial values of the energy curve as (see e.g. [41])

$$E(r_s) = r_s^2 p_s v_s v(r_s) \mu, \quad (5.48)$$

where

$$v(r_s) = \int_0^{\infty} f(r_s, \tau) d\tau, \quad f(r_s, \tau) = \frac{r_s^2 p v}{r_s^2 p_s v_s} \quad \text{and} \quad \tau = \frac{t - t_0(r_s)}{\mu}. \quad (5.49)$$

5.4 PROBLEM SOLUTION - SEMI-EMPIRICAL SOLUTION OF THE SHOCK WAVE PROPAGATION

Because the integral represents the shape of the shock wave, imposing a constant value on it is equivalent to introducing a similarity condition. Its value is 1 for an exponential decay and 2/3 for a linear pressure-position curve. If Eq. (5.48) is substituted into Eq. (5.47), it gives the last missing relation. The pressure decay along the shock wave position is given by

$$\frac{dp_s}{dr_s} = \frac{\partial p_s}{\partial r_s} + \frac{1}{u_s} \frac{\partial p_s}{\partial t}, \quad (5.50)$$

where the derivatives can be expressed from Eqs. (5.37), (5.38), (5.42) and (5.47) to yield

$$\frac{dp_s}{dr_s} = -\frac{r_s^2 p_s^3}{E_s(r_s) \rho_0 u_s^2} \frac{1 - \left(\frac{\rho_0 u_s}{\rho c}\right)}{2(1+g) - \left(1 - \left(\frac{\rho_0 u_s}{\rho c}\right)\right)} - \frac{p_s \left(\frac{4\rho}{\rho_0} + 2\left(1 - \frac{\rho}{\rho_0}\right)\left(1 - \left(\frac{\rho_0 u_s}{\rho c}\right)\right)\right)}{r_s \left(2(1+g) - \left(1 - \left(\frac{\rho_0 u_s}{\rho c}\right)\right)\right)}. \quad (5.51)$$

The variation of the shock wave energy with the position r_s is given by the first integral in the relation (5.46) as

$$\frac{dE_s(r_s)}{dr_s} = -\rho_0 r_s^2 h_{dis}(p_s(r_s)). \quad (5.52)$$

The final step of the derivation is to obtain a formulation of the enthalpy h_{dis} as a function of the peak pressure p_s . It can be done using the following consideration. If the shock wave reaches a position in liquid, which has the temperature T_0 and pressure p_0 , the temperature and pressure in that place is increased up to the values p and T as it can be seen in Figure 5.4. The specific enthalpy increment experienced by the fluid is Δh_s which is given in Eq. (3.75). Having passed the shock wave the pressure in the liquid reaches again the pressure p_0 along the adiabatic curve but the temperature returns to a higher value T_1 due to the dissipation process. Based on the consideration, the enthalpy increment Δh_s can be evaluated as a sum of the undissipated and dissipated enthalpy as

$$\Delta h_s = h + h_{dis}, \quad (5.53)$$

where the undissipated enthalpy h is given by

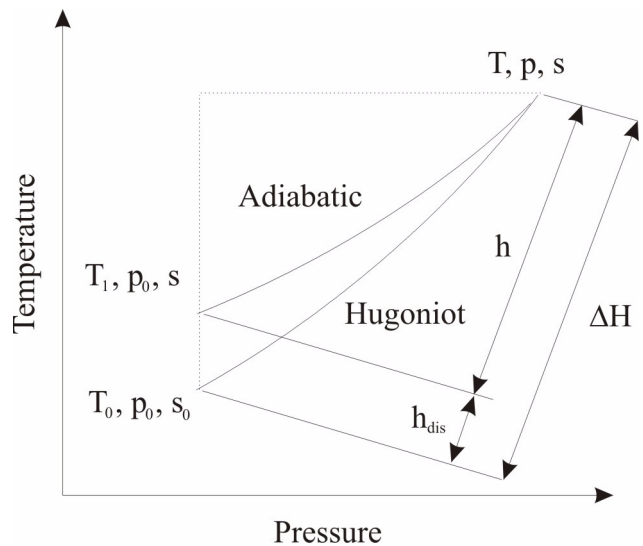


Fig.5.4 Adiabatic and Hugoniot contours in p-T plane.

$$h = \int_{p_0}^p \frac{1}{\rho} dp, \quad (5.54)$$

which can be expressed using the equation of state (D.2) according to the Figure 5.4 as

$$h = \frac{2c_1}{n-1} \left[\left(\frac{\rho}{\rho_1} \right)^{n-1} - 1 \right]. \quad (5.55)$$

The dissipated enthalpy can be evaluated from the specific heat data, which are known as the explicit function of the temperatures T_0 and T_1 as

$$h_{dis} = \int_{T_0}^{T_1} c_p(T_0, T_1) dT. \quad (5.56)$$

The resulting Eq. (5.53) can be then expressed using Eqs. (3.75) and (5.54) as

$$\frac{h_{dis}}{c_1^2} = -\frac{2}{n-1} \left(\left(\frac{\rho}{\rho_1} \right)^{n-1} - 1 \right) + \frac{p_s}{2\rho_1} \left(\frac{\rho_1}{\rho} + \frac{\rho_1}{\rho_0} \right), \quad (5.57)$$

where the density ρ can be eliminated using the equation of state in the form

$$p = B(T_1) \left[\left(\frac{\rho}{\rho_1} \right)^{n-1} - 1 \right] = \frac{c_1^2 \cdot \rho_1}{n} \left[\left(\frac{\rho}{\rho_1} \right)^{n-1} - 1 \right], \quad (5.58)$$

considering that $B(T_1) = (c_1^2 \cdot \rho_1)/n$. Using the specific heat data $c_p(T_1)$ given in Appendix D, the integral (5.53) can be evaluated as a function of the temperature T_1 . As all the variables ρ_1 , c_1 , B and c_p can also be obtained from the data given in Appendix D as explicit functions of the temperature T_1 , Eq. (5.58) gives the implicit relation between the pressure p_s and the temperature T_1 , which can be used in Eq. (5.56) to obtain the enthalpy h_{dis} . Note that the temperature can be obtained from the equation by an appropriate iterative method.

5.5 Cavitation bubble in glycerine

In order to estimate density inside the cavitation bubble generated by laser, the measurement described in Chapter 4.3.4 was performed. The idea is based on the fact that from the measured ultimate velocity of a particle floating in liquid, using the momentum balance on the particle (bubble), the density inside the particle can be obtained. The balance of forces acting on a particle of radius $R(t)$ is given e.g. according to Michaelides [46] or Brennen [16] as

5.5 PROBLEM SOLUTION - CAVITATION BUBBLE IN GLYCERINE

$$K_1 = \frac{9}{2} \frac{\eta}{R^2(0.5\rho_\infty + \rho_B)}, K_2 = \frac{(\rho_B - 0.5\rho_\infty)}{R^2(0.5\rho_\infty + \rho_B)}. \quad (5.63)$$

The time duration of the measurement was about 10 seconds. After this time, the second term in the parenthesis in Equation (5.63) becomes negligibly small in comparison to 1 and the velocity of the bubble will converge to a constant value v_∞ . From Equation (5.63) then follows the relation between the densities

$$\rho_B = \rho_\infty - \frac{9v_\infty\eta}{2R^2g}. \quad (5.64)$$

6. RESULTS

In the following paragraphs, the numerical calculations utilizing the models introduced in Chapter 5.2 will be performed in order to obtain the energy distribution of the laser pulse in water and isooctane. First, the numerical simulations of the bubble dynamics using the model (5.7) will be presented. The results are used in the modified method of characteristics for the calculations of the pressure and velocity field in the liquid around the bubble during its grow and first collapse. From the pressure and velocity field, the shock wave velocity and pressure profiles are obtained. By collecting the pressure data at the fixed position close to the plasma centre, the pressure-time profiles are determined. Based on the obtained data, the energy distribution of the laser pulse is calculated. The energy and the pressure peak calculated at the position close to the plasma centre are used as the boundary condition for the semi-empirical model introduced in Chapter 5.4, which considers dissipation of energy at the shock wave. Finally the cavitation bubble collapse at two distances from the solid wall is simulated using the commercial code Fluent.

6.1 Numerical simulation of the laser induced bubble dynamics

The numerical calculations of the bubble radius evaluation were based on the measurements presented in Chapter 4.3.2 (Figure 4.19), which provided the boundary and the initial conditions for the simulations. The values of the maximum plasma size, the first and the second maximum bubble radii and the laser pulse energy used in the simulations are given in Table 4.1. The material data required for the simulations, which are given in Table 6.1, were obtained from the NIST Webbook (<http://webbook.nist.gov/chemistry/>) for water and for isooctane from the data published by Malthorta [53]. All the processes experienced by the gas inside the bubble during the simulation were considered adiabatic with constant $\gamma = 1.4$. The simulations start at the bubble radius R_{0a} , which was identical to the maximum plasma size. The value of R_{0b} was adjusted during a test simulation in which the first maximum radius had to be reached. The radii R_{0a} and R_{0b} had a marginal influence on the initial bubble wall velocity. The influence of the laser pulse duration was much weaker. The numerical simulation presented in Figure 6.1 was divided into two steps; the simulation from the initial bubble radius R_{0a} to the first maximum radius and then the simulation from the first maximum radius to the following compressions and expansions. This step was introduced because it was not possible to reach the same second maximum radius as obtained from the experiment. This disproportion could be caused by the cooling effect of the bubble contents during the first bubble expansion, which could break the assumption of adiabatic behaviour of the bubble contents. Note that the initial bubble temperature is close to plasma temperature. At this point, it is important to remind that in the measurement results a small decrease of the radius was observed at the end of the first expansion. The results of the time history of the initial bubble wall velocity both for water and isooctane are shown at the bottom lines in Figure 6.1. The velocities reach very high values in the interval of several nanoseconds and then

6.1 RESULTS - NUMERICAL SIMULATION OF THE LASER INDUCED BUBBLE DYNAMICS

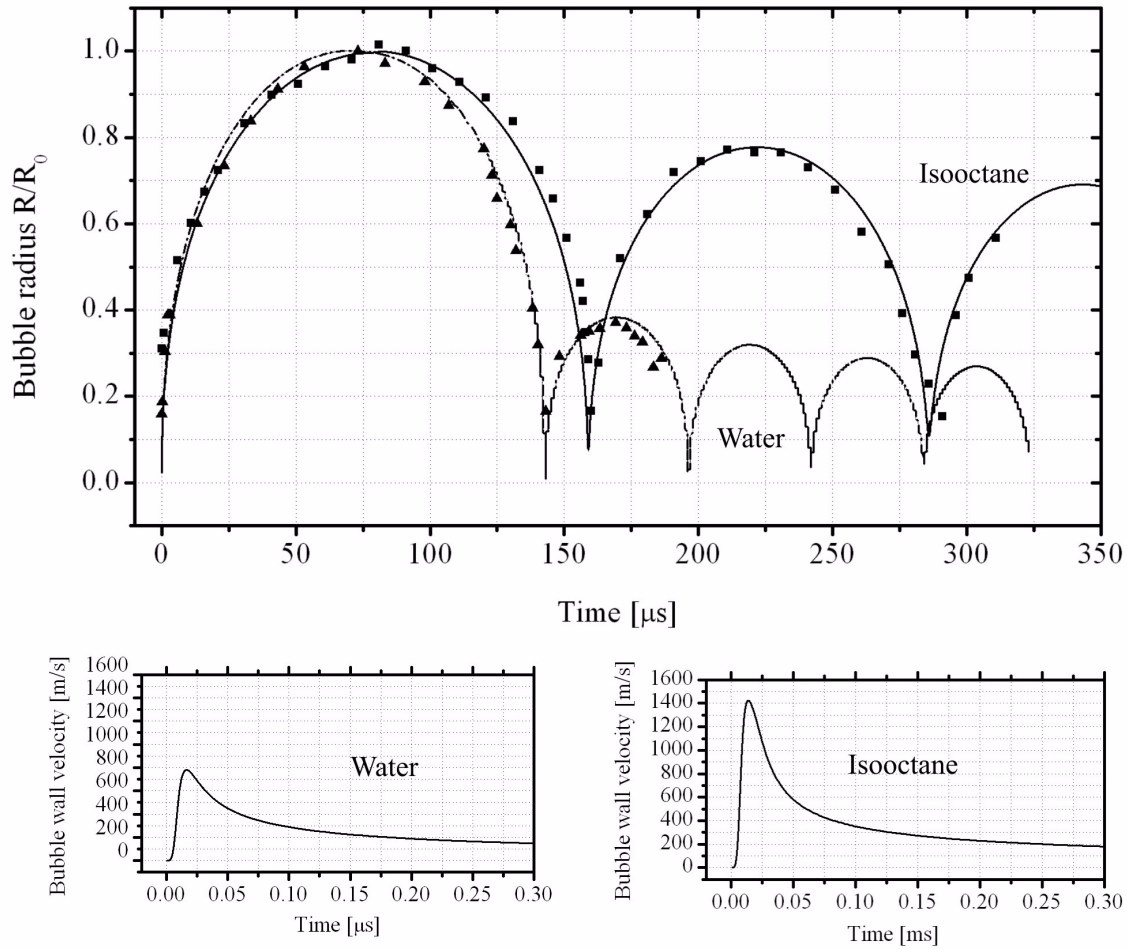


Fig.6.1 Numerical simulations of the time history of the bubble radius compared with the experimental data in water (triangles) and isoctane (bricks). The bottom figures represent the initial velocity of the bubble radius.

decrease to a much smaller value. The maximum velocities reached by the bubble wall were about 800 m/s in water and 1400 m/s in isoctane. The violent bubble expansion in the case of isoctane indicates the presence of a strong shock wave in the region close to LIB. During the simulations of the bubble compression from the first maximum radius the initial velocity of the bubble wall was set to zero and the initial gas pressure inside the bub-

Quantity	Water	Isooctane	Units
Density	998	691	$m^3 \cdot kg^{-1}$
Speed of sound	1483	1150	$m \cdot s^{-1}$
Surface tension	0.0727	0.0200	N/m
Viscosity	0.0010	0.0005	Pa.s
Far field pressure	0.1	0.1	MPa
Tait equation coefficient B	314	70	MPa
Tait equation coefficient n	7	9.8	
Vapour pressure	2291	5112	Pa

Table6.1 Liquid properties for numerical solution for temperature 293 K.

6.2 RESULTS - NUMERICAL SIMULATION OF THE PRESSURE AND VELOCITY FIELD

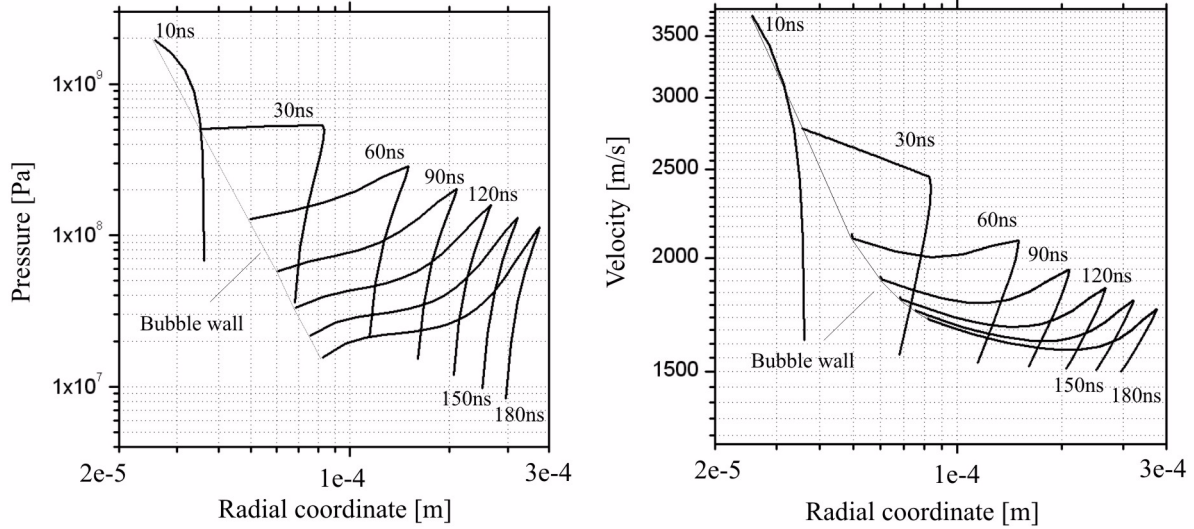


Fig.6.2 Pressure and velocity field in liquid surrounding cavitation bubble during its growth in water.

ble was adjusted according to the test to reach the second maximum radius.

6.2 Numerical simulation of the pressure and velocity field

The pressure and the velocity fields calculated during the initial expansion of the bubble in water and isoctane are shown in Figure 6.2 and in Figure 6.3. The lines in the figures represent the pressure and the velocity distributions at different time instants of the bubble expansion. Each line originates at the bubble wall, which is indicated by the dotted line in the figure. As the simu-

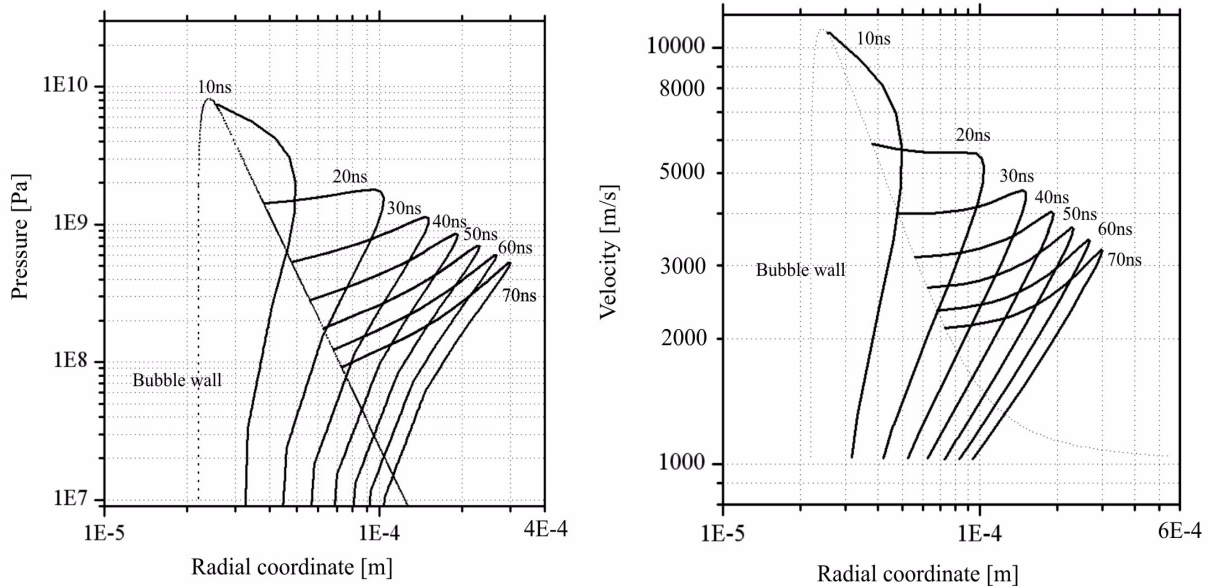


Fig.6.3 Pressure and velocity field in liquid surrounding cavitation bubble during its growth in isoctane.

6.2 RESULTS - NUMERICAL SIMULATION OF THE PRESSURE AND VELOCITY FIELD

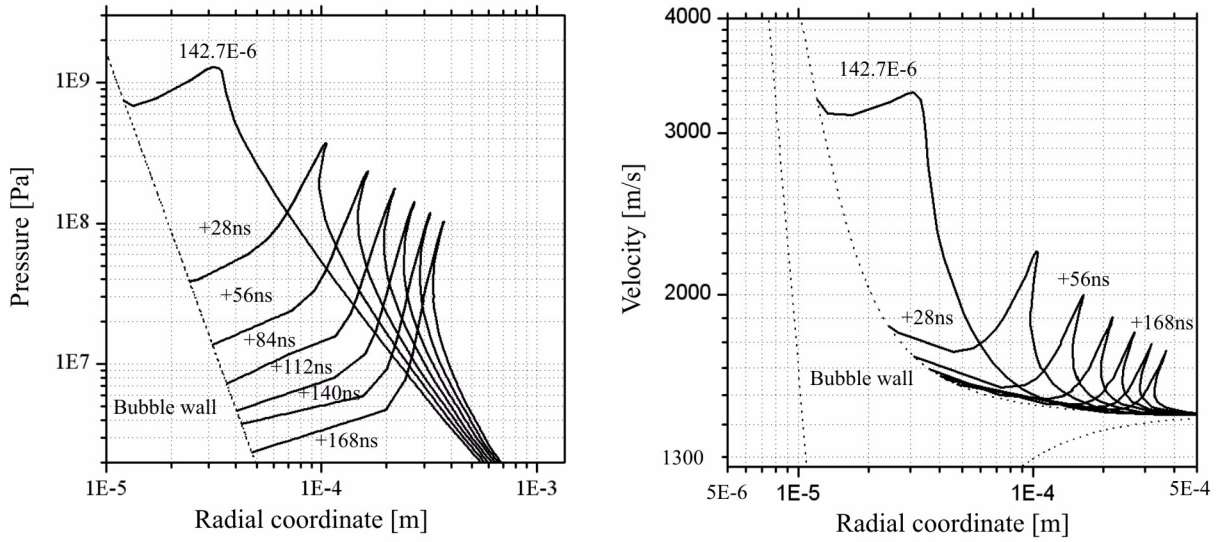


Fig.6.4 Pressure and velocity field in liquid surrounding cavitation bubble during its collapse in water.

lations directly follow the calculations of the bubble dynamics during the initial bubble expansion and after the first collapse, the same material data as for the bubble dynamics calculation were used. It can be seen that the shock wave in water is developed from the sound wave at the radius about 7×10^{-5} mm and in isoctane 2×10^{-5} mm. The functions represented by the lines have only one value when no shock wave is present and two values in the region, where the shock wave is

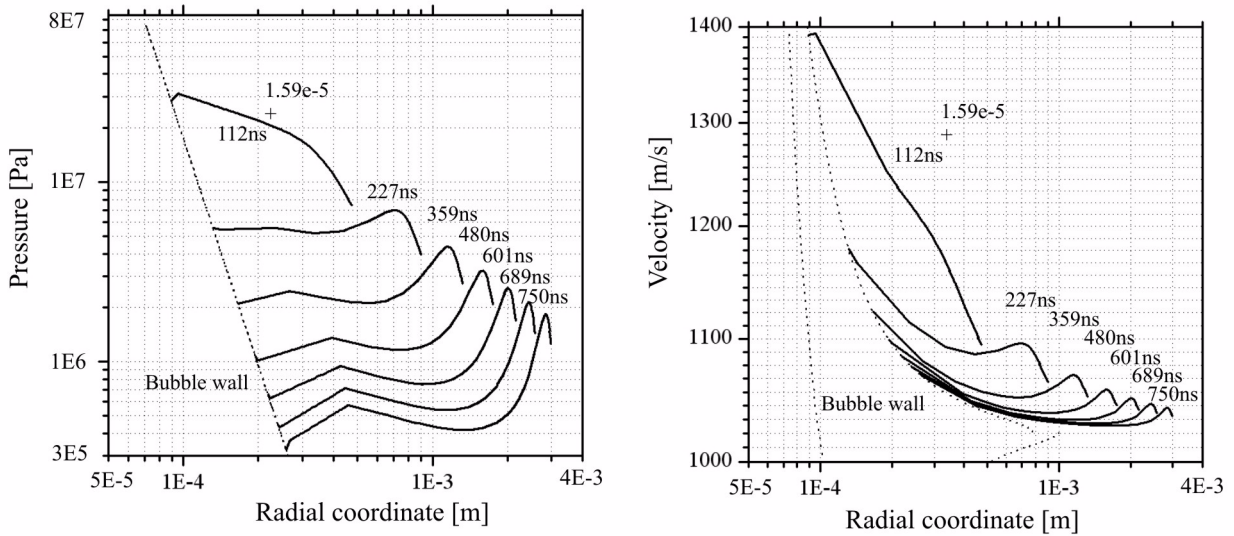


Fig.6.5 Pressure and velocity field in liquid surrounding cavitation bubble during its collapse in isoctane.

6.2 RESULTS - NUMERICAL SIMULATION OF THE PRESSURE AND VELOCITY FIELD

developed. This is, of course, physically incorrect, but the region with double values represents the discontinuity (shock wave). Usually it is adequate to place the shock wave in the centre of the double valued region. The idea of the placement of the shock wave follows from the equality of the surfaces defined by the velocity-position curve, as it was shown e.g. by Landau [42]. The times corresponding to the developed shock wave are about 20 ns in water and less than 10 ns in isoctane. The comparison of the shock wave velocity in water 2500 m/s and in isoctane 10,000 m/s shows that the shock waves in water are weaker than in isoctane. The peak points of the curves represent approximately the position of the shock wave at different instants, which is in agreement with the measured shock wave velocities obtained from the experiment. The comparison of the experimental curves, shown in Figure 4.21, shows good agreement for water, however, for isoctane there is a strong disproportion. This can be caused by incorrect material data for iso-

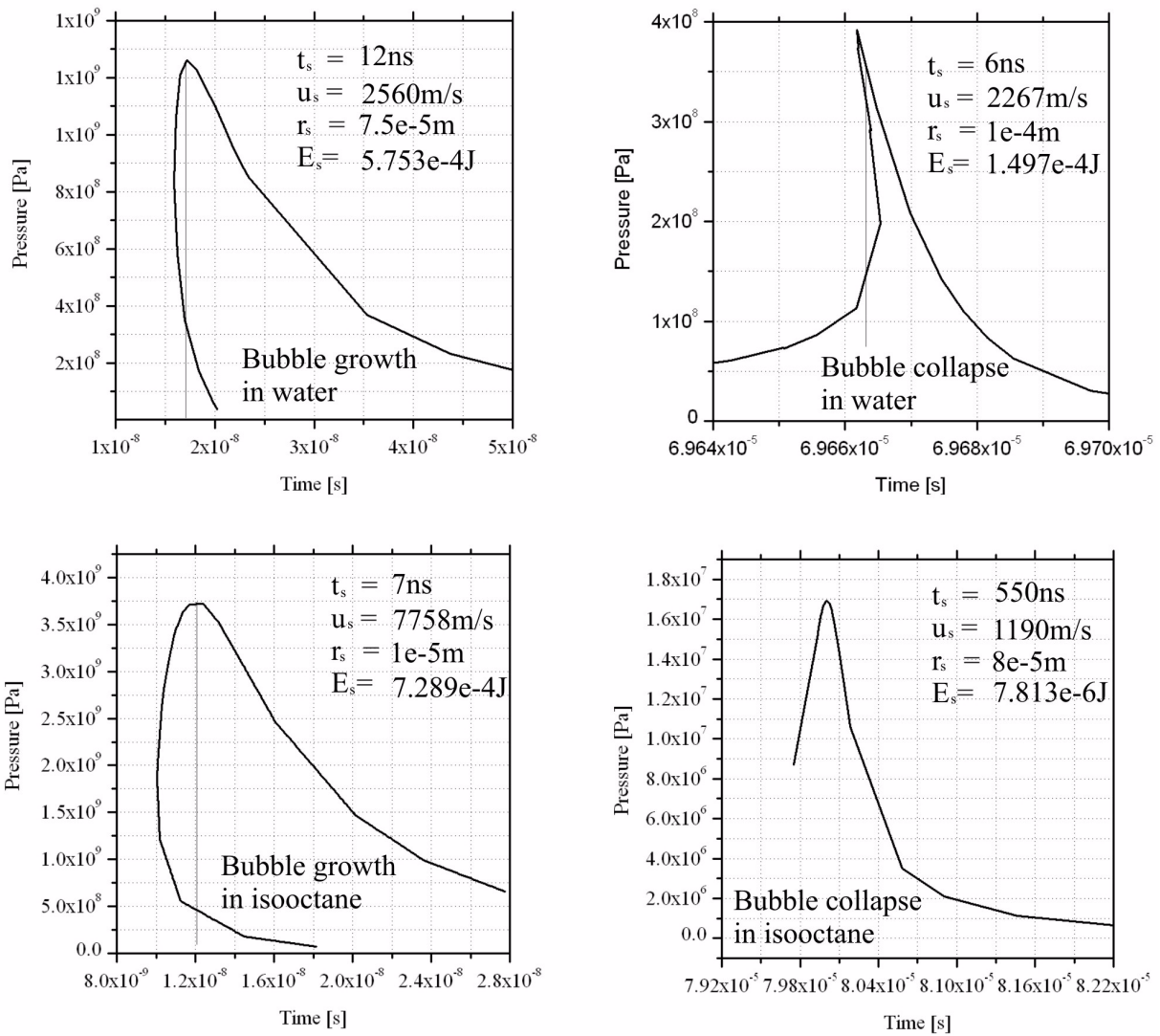


Fig.6.6 Pressure-time profiles of the shock waves in water and isoctane calculated by the modified method of characteristics.

octane, which is not available for such high pressures. The second reason can be neglecting the dissipation effects in the solution of the shock wave using the modified method of characteristics. Note that the measurement data were obtained in the region, where the shock wave velocity was already close to the sound wave velocity and huge amount of the energy had already been dissipated.

6.3 Evaluation of the shock wave pressure-time profiles

The pressure fields calculated in Chapter 6.2 are used at this point to evaluate the pressure-time profiles, which are needed for the shock wave energy calculation. The results of the calculations are presented in Figure 6.6, which also includes the data characterizing the shock wave; such as the position r_s , the peak pressure p_s , shock wave velocity u_s and the full width at half maximum of the pressure-time curve. This parameter connects the pressure-time profiles obtained by the method of characteristics (in Figure 6.6) with the time profiles given by Eq. (5.29), which have the form acceptable for the calculations. The profiles were obtained by collecting the pressure data at the position, where the shock wave developed from the sound wave. Because the shock wave energy is calculated from the pressure-time profile, the surface under the curve indicates that the shock wave energy would be higher in isoctane than in water. The results also show that in water the shock wave is generated during the first and the second bubble expansion but in isoctane the shock wave is generated only during the first expansion.

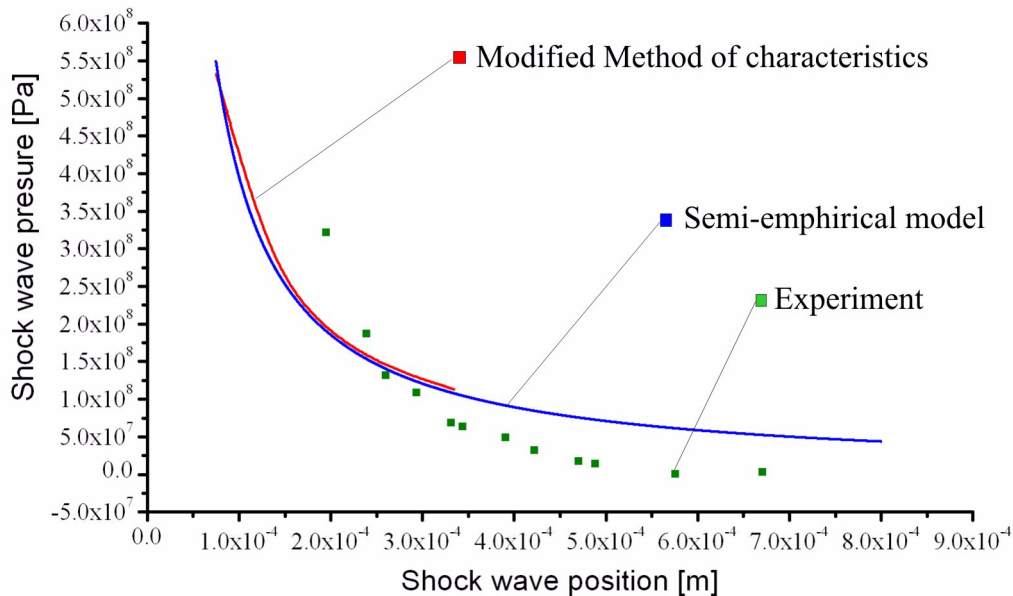


Fig.6.7 Curves of position of the shock wave peak pressure in water obtained by the modified method of characteristics (without dissipation), by semi-empirical model (including dissipation) and from experiment.

6.4 Numerical simulation of energy dissipation at the shock wave

The equations describing the shock wave propagation including the energy dissipation are (5.51) and (5.52). These equations require two boundary conditions: the shock wave peak pressure p_s and the shock wave energy E_s both evaluated at the position r_s . This information is usually obtained from the experiment. As it was not possible to obtain the data with the used experimental setup, the boundary condition were set according to the modified method of characteristics. Because the pressure peak p_s was known from the solution as a function of the coordinate r_s it was also possible to calculate

$T_0=293K$	NIST			Richardson[47]
p_s [MPa]	ΔT_1 [K]	T1 [K]	h_{dis} [J/kg]	h_{dis} [J/kg]
0	0.0	293.0	0.0	0.0
2.5	0.2	293.2	1046.0	x
5	1.2	294.2	5152.0	5570.0
10	5.4	298.4	22480.0	23450.0
15	11.5	304.5	47978.0	49350.0
20	18.8	311.8	78484.0	80050.0
25	26.9	319.9	112547.0	115000.0
30	35.6	328.6	148720.0	152500.0
35	44.7	337.7	186806.0	192000.0
40	54.0	347.0	225771.0	233000.0
45	63.5	356.5	265524.0	x
50	73.1	366.1	305979.0	317500.0
53	78.8	371.8	330194.0	x

Table6.2 Dissipated enthalpy calculated as a function of pressure at the shock wave.

the energy integral (5.28) at the position r_s . Note that the propagation of the shock wave including the energy dissipation was calculated only for water. The specific heat data, the shock wave velocity and density as functions of temperature and pressure were approximated from NIST Webbook and then implemented into the model. First, the temperature of the liquid after the shock wave passed was calculated from Eq. (5.57). Using this temperature the dissipated enthalpy was calculated from Eq. (5.56). The analytical expression for the dissipated enthalpy as the function of the shock peak pressure derived from the NIST data can be written as

$$h_{dis}(p_s) = 3.0917 \times 10^{-2} p_s^4 - 4.7538 p_s^3 + 2.8574 \times 10^2 p_s^2 - 1.5626 \times 10^2 p_s. \quad (6.1)$$

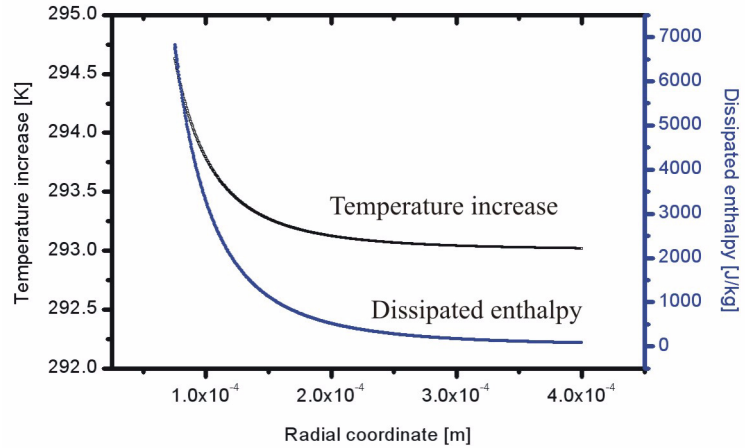


Fig.6.8 Dissipated enthalpy and temperature increase at the shock wave as a function of radial coordinate.

6.4 RESULTS - NUMERICAL SIMULATION OF ENERGY DISSIPATION AT THE SHOCK WAVE

The results of the calculation of the dissipated enthalpy as the function of the shock peak pressure p_s are presented in Table 6.2. It is obvious from the results that for lower pressures up to 10 MPa the temperature increase after the shock wave has passed is small. However, for high pressures the temperature rise is considerable.

	Water	Isooctane	Units
Bubble energy Rmax1	1.59E-04	3.94E-04	J
Bubble energy Rmax2	4.98E-06	1.86E-04	J
Radiated energy	4.04E-07	4.52E-06	J
Evaporation energy	1.12E-04	1.10E-05	J
Energy between the first and second maximum bubble radius	1.54E-04	2.09E-04	J
Energy of the first shock wave	5.75E-04	7.29E-04	J
Energy of the second shock wave	1.50E-04	7.81E-06	J

Table 6.3 Energy distribution of the laser pulse in water and in isooctane.

Note that the calculations are approximated only under the boiling point of water. The results for the propagation of the shock wave peak pressure are presented in Figure 6.7. From the figure it is obvious that the modified method of characteristics and the semi-empirical model give similar results and the inclusion of the dissipation effect results in a slightly faster decay. This is in agreement with the results presented in Figure 3.11, which shows similar shock wave propagation for low pressures for both theories. The dissipation effect is small as the temperature rise corresponding to the peak pressure is only about 1.5 K. This results in a small dissipated enthalpy, which is evident from Figure 6.8. The comparison of the measured data with the calculations indicates that the time resolution of the experiment was not satisfactory, especially at the positions close to the plasma centre. It can be expected that the pressure and the velocity on the plasma surface are higher.

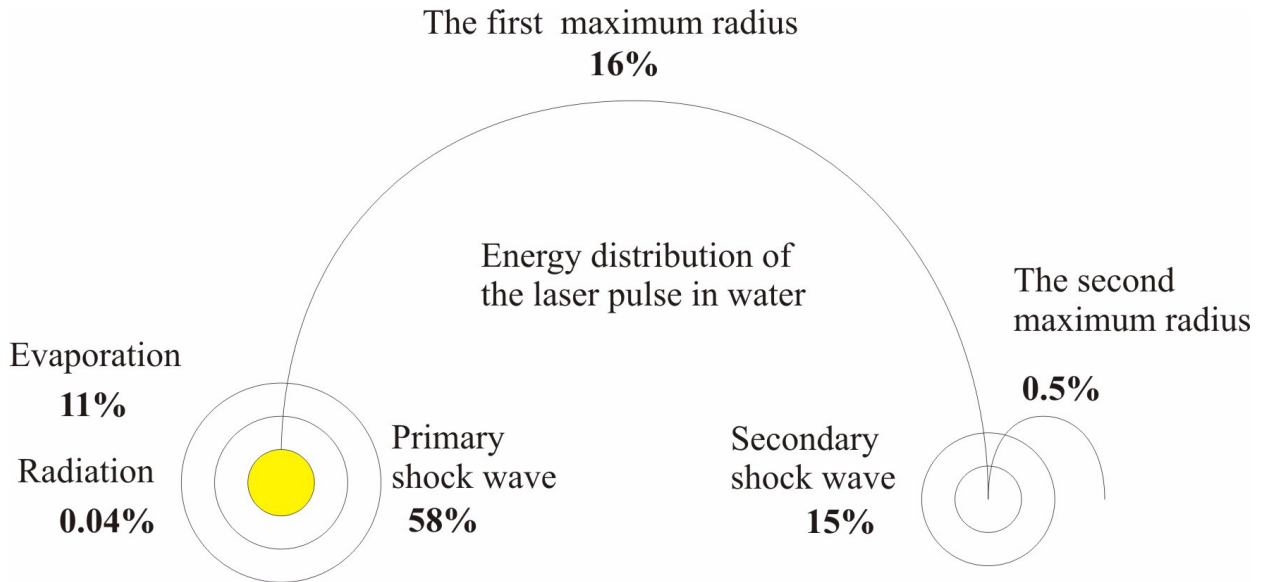


Fig. 6.9 Energy distribution of the laser pulse in water.

6.5 Energy distribution during the bubble growth and collapse

The energy distributions of the laser pulse in water and isooctane are summarized in Table 6.3. Generally, it is possible to conclude that the most important energy consumers are the cavitation bubble, the first shock wave and the evaporation energy. The radiated energy is low due to small plasma size. The results for water, which are also illustrated in Figure 6.9, show that the sum of the individual energy fractions is about 1mJ. This indicates that the laser energy was probably underestimated and the real energy was higher than the measured one. The comparison of the second shock wave energy and the energy between the first and the second maximum bubble radii shows that it is possible to represent this energy difference as the energy consumed for the creation of the secondary shock wave. The sum of the individual fractions of the laser energy for isooctane is about 50% higher than the total pulse energy. This is probably caused by the inaccurate value of the first shock wave energy, which is very high. Note that the pressure data for isooctane are available only up to 1000 MPa, which is exceeded several times by the peak pressure at the shock wave in isooctane. Also the energy of the second shock wave did not correspond to the available energy (the difference between the first and the second maximum radii). The value of the energy of the secondary shock wave calculated from the energy difference between the first and second maximum bubble radii is probably more correct. The comparison of the energy distribution in water and isooctane shows that in both cases the most important part of the laser pulse is consumed for the primary shock wave and the first bubble expansion.

6.6 Density of cavitation bubble rising in glycerine

This short chapter represents the results of the calculation of the density inside the cavitation bubble in glycerine using the relation (5.64). The results and the required material data are presented in Table 6.4. The bubble density in this case is closer to the liquid density than the gas den-

Thermophysical quantities		Measured quantities		
η [Pa.s]	$\rho_{\text{Glyc.}}$ [kg/m ³]	U_{∞} [m/s]	R_{∞} [m]	ρ_B [kg/m ³]
1,42	1260	1.80E-04	4.40E-04	654

Table 6.4 Material data and results of calculation of density inside the cavitation bubble rising in glycerine.

sity. The value can be influenced by neglecting the memory term in the momentum balance (5.59), however, the error given by this simplification is less than several percent.

6.7 Numerical simulation of bubble collapse

The simulation of the cavitation bubble collapse near the solid wall was performed using the CFD software Fluent using the Volume of fluid method, which was developed by Hirt and Nichols [47]. The bubble collapse was simulated from its first maximum radius and the driving

6.7 RESULTS - NUMERICAL SIMULATION OF BUBBLE COLLAPSE

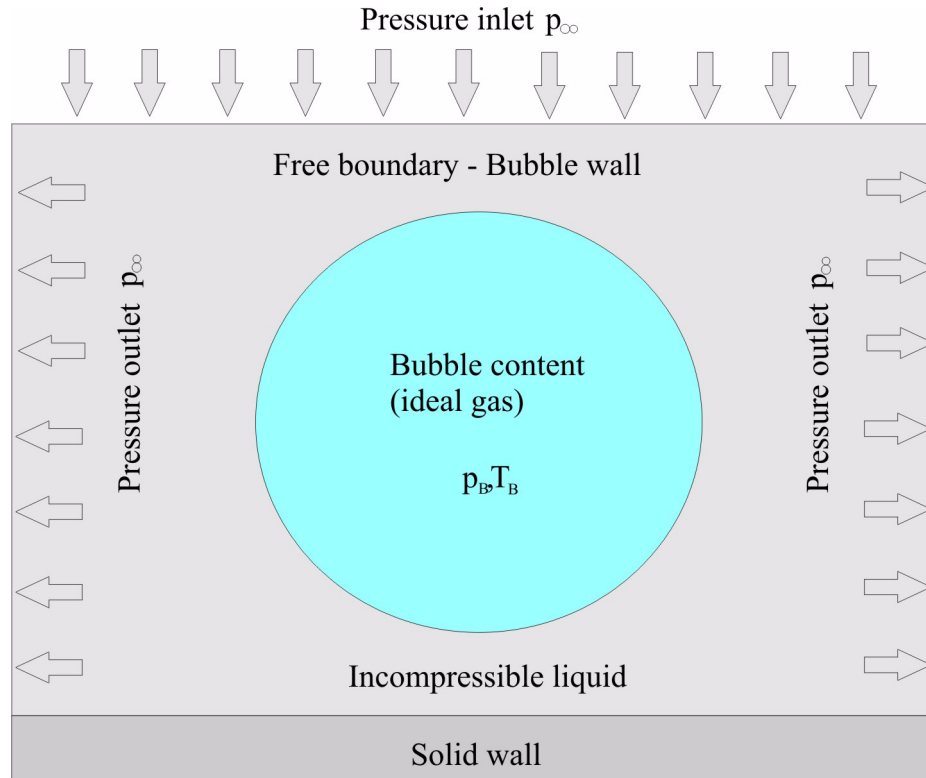


Fig.6.10 Model for simulation of cavitation bubble collapse.

mechanism to initiate the bubble wall motion was the pressure difference between the bubble contents and the surrounding liquid. The schematic arrangement of the model is shown in Figure 6.10. The calculations were realized on a mesh including 20,000 quadratic elements and the single bubble was placed into the liquid at several different distances from the solid wall. The problem was treated as symmetrical and the heat and mass transfer between the bubble and the wall was neglected. The boundary conditions were the atmospheric pressure at the pressure inlet and outlet. The initial conditions were set to 30 kPa inside the bubble and to the atmospheric pressure in the liquid around the bubble. At the initial time the temperature was set to 293.15 Kelvin in the whole computational domain and the phase fraction coefficient $\alpha = \text{gas/liquid}$ was set to 0 in the bubble domain and to 1 in the incompressible liquid domain. The flow was treated as laminar and the physical properties of the liquid were assumed constant in space and time. The gas inside the bubble was treated as ideal (the equation of state for ideal gas was used). For the simulation, the segregated solver was used and the momentum and energy equations were discretized using the first order upwind scheme. For the pressure interpolation, the Standard scheme [56] was used and the pressure and velocity were coupled using the Simple method [56]. For the temporal discretization of the equations, the first order approximation was used. The bubble boundary was approximated using the Geometrical reconstruction scheme [55], [56]. The bubble behaviour was

6.7 RESULTS - NUMERICAL SIMULATION OF BUBBLE COLLAPSE

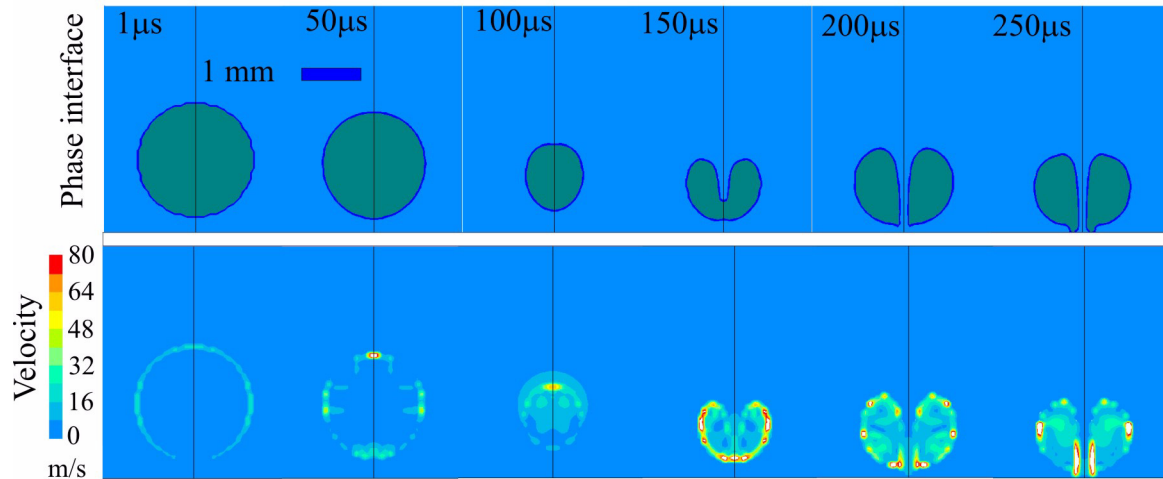


Fig.6.11 Bubble collapse at the distance 1.22 mm from the solid wall. The first line represents the phase shape and the second line represents the interface velocity. The initial bubble radius was 1 mm.

compared for the bubble positions 1.2 mm and 2 mm from the wall and for two different bubble radii.

The results of the numerical calculations with the initial bubble radius 1 mm are shown in Figure 6.11 and in Figure 6.12. The first figure sequence shows two successive bubble compressions and expansions. It can be seen that the presence of the solid wall strongly influences the bubble shape, especially when the bubble withstands the second collapse. As it has already been

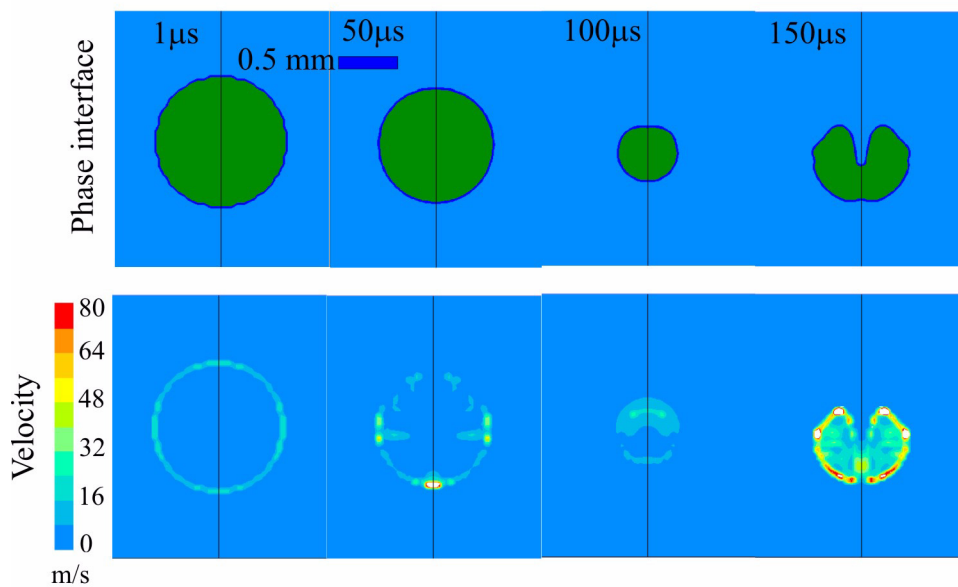


Fig.6.12 Bubble collapse at the distance 2 mm from the solid wall. The first line represents the phase shape and the second line represents the interface velocity.

6.7 RESULTS - NUMERICAL SIMULATION OF BUBBLE COLLAPSE

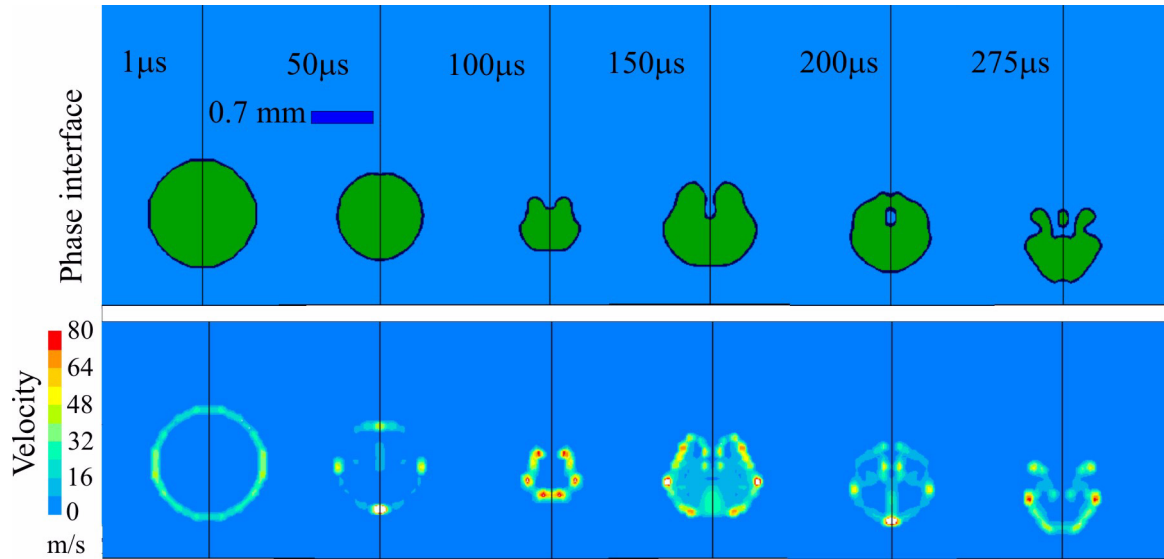


Fig.6.13 Bubble collapse at the distance 1.2 mm from the solid wall. The first line represents the phase shape and the second line represents the interface velocity. The initial bubble radius was 0.7 mm.

predicted from the experiment, a bubble jet is generated against the wall. When comparing the results for the distance at 2 mm and at 1.2 mm from the wall one can conclude that the bubbles at the position closer to the solid wall tend to generate the jet sooner than the bubbles farther from the wall. It can also be seen that the bubbles at the positions farther from the wall are accelerated more than the bubbles at the close positions. The comparison of the velocity fields between the

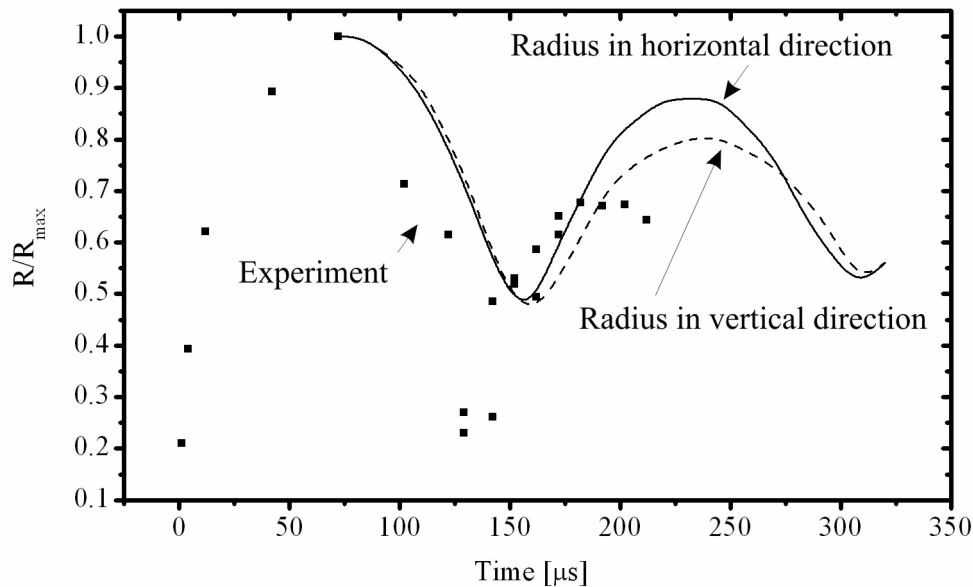


Fig.6.14 Comparison of the time curves of the bubble radius during the collapse obtained by the numerical calculation using CFD (corresponding to Figure 6.13) and from experiment. The initial bubble radius was 0.7 mm and the distance of the bubble centre from the wall was 1.2 mm.

6.7 RESULTS - NUMERICAL SIMULATION OF BUBBLE COLLAPSE

two cases shows no significant difference in the bubble behaviour. The calculations show that during the jet generation the liquid close to the bubble axis exceeds the velocity of 80 m/s, which is indicated by white color in the figures. The maximum reached jet velocity was 118 m/s for the 1.2 mm distance and 160 m/s for the 2 mm distance. The densities inside the bubble during the first two expansions were close to 10 kg/m^3 , which shows that the pressure inside the bubble does not significantly contribute the erosion process. Also the temperature during the bubble collapse oscillates close to the initial value. This, however, does not mean that the densities and temperatures inside the bubble cannot reach higher values.

The simulation presented in Figure 6.14 shows the comparison of the time curves of the bubble radius during the collapse obtained from the CFD calculation (corresponding to Figure 6.13) and from the experiment (corresponding to Figure 4.24). The difference in the values of the bubble radius is probably caused by different pressures inside the bubble, which prevent the bubble radius to collapse to a smaller value. It is also seen that the vertical and the horizontal bubble deformation differs significantly as soon as the rebound starts. It should be noted that the initial bubble pressure was set to 30 kPa, which results in a rather modest bubble collapse. It would be appropriate to test the calculations using a lower initial bubble pressure, however, for this kind of simulation the numerical model has to be improved.

7. CONCLUSION

7.1 Summary and critical evaluation

Many investigations in the framework of the cavitation bubble dynamics and shock wave propagation have been done in regular fluids, however, only a small attention has been paid to the comparison of the cavitation bubble dynamics and the bubble collapse in various liquids. In addition, only a small fraction of the reviewed works concentrated on the influence of the bubble generation (laser type, wavelength) on the bubble dynamics. The shock wave propagation in the case of the laser-induced breakdown in liquid is usually solved using models, which exclude the dissipative effects. This, however, results in the fact that the shock wave decay occurs on a longer distance than in reality. This effect is responsible for the disproportion between the measured and calculated data.

This work provides a comprehensive investigation of the behaviour of the cavitation bubble generated by two different types of lasers in three different types of liquids. The following liquids were chosen as samples: water as a representative of regular liquids, isooctane as a representative of irregular liquids, and glycerine for its high viscosity and density. Based on the information obtained from the literature research, two experimental setups were designed. The phenomena were recorded by the ultra-speed camera Imager 3 using the multi-exposure and single-exposure camera modes. The multi-exposure measurement mode was developed in order to improve the reproducibility of the experiment. The first experimental setup used the pulse Tm-Yag laser at 2000 nm wavelength and 1 ms pulse width. In this setup, an optical fiber was placed into the investigated liquid in order to supply the laser energy. The results of the experiments performed with the Tm-Yag laser showed the classical behaviour of the bubble with its characteristic series of expansion and compressions. A shock wave at the end of the optical fiber was observed after the laser-induced breakdown and during the first bubble collapse. However, due to the instability of the laser power, the shock wave propagation could not be investigated. The shape of the produced cavitation bubble was strongly influenced by the optical fiber and the laser mode (free running, Q-switched). The bubbles generated in the free running laser mode were pyriform in contrast to the bubbles generated in the Q-switched mode, which were almost spherical. The collapsing cavitation bubble strongly damaged the end of the optical fiber by the liquid jet, a fact which could present a serious problem in medical applications.

The second experimental setup was based on the pulse Nd-Yag laser at the 1064 nm wavelength and 6 ns pulse width. The laser was used in the Q-switched mode only. The laser energy was delivered into the sample fluid through the monochromatic lens, which was built into one wall of the cuvette. The laser beam was focused through the lens into a small spot to produce the breakdown. The plasma formation was followed by shock waves and bubble production. The reproducibility of the experiments performed by the Nd-Yag laser enabled to record the propagation of the shock wave generated after the optical breakdown. The comparison of the bubble behaviour in the studied liquids showed that the second maximum bubble radius in isooctane was

7.1 CONCLUSION - SUMMARY AND CRITICAL EVALUATION

more than twice as high as in water for the same energy level. The experiments showed no significant differences in the shock wave propagation for water and for isooctane.

The cavitation bubbles generated by the Nd-Yag laser in glycerine showed no significant oscillation and no bubble collapse. The bubbles were let to rise to the free surface in order to estimate the density inside the bubbles. The density value was derived from the momentum balance on the bubble interface. The results showed that the density inside the bubble was closer to the liquid density (the the order of 10^2) than to the density of gas (of the order of 10^1).

Finally, the cavitation bubble collapse in the free liquid and near the solid wall was investigated using the setup based on the Nd-Yag laser. The laser beam was focused near an L-shaped profile, which represented the solid wall. The results showed that if the cavitation bubble is not generated directly on the wall the collapse and the first bubble growth are not influenced by the presence of the wall. The results also show the change of axis of symmetry of the bubble. During the bubble expansion the axis of symmetry of the bubble is coincident with the optical axis of the laser beam; however, during the first compression the axis of symmetry of the bubble is rotated perpendicularly to the solid wall. After that a jet is generated against the wall and the bubble either breaks up or rebounds. For the bubble collapse in the free liquid in some cases the bubble fission into smaller bubbles, which then coalesce again into a single bubble.

The experiments were performed in the way as to ensure the best possible reproducibility of the measured data; however, some problems, which were not taken into account, lead to some uncertainty. First, the laser was not focused into the smallest possible spot size, which can lead to uprise of hot spots along the beam path. This problem, however, was suppressed by using a small laser energy of about 1 mJ. The second problem is associated with the temporary resolution of the experiment. As a result, some of the high frequency phenomena could be overlooked.

The results obtained from the experimental investigation performed by the Nd-Yag laser in water and isooctane were used as the start values for numerical simulations. The model for calculation of the time evolution of the bubble radius considered viscous compressible liquid with the influence of surface tension and with boundary conditions respecting the laser energy absorbed by the liquid. The simulation was divided into two parts; the simulation of the first expansion driven by laser pulse and then the collapse from the first maximum bubble radius and the following rebounds. The laser pulse was simulated by the growth of the equilibrium bubble radius in the bubble dynamics equation. For the initial velocity of the bubble during the growth it was assumed that the bubble is an envelope of expanding plasma, which originated by the absorption of the laser pulse. The initial conditions for each phase were adjusted to reach the first maximum (in the case of the first expansion) and second maximum radius (in the case of the first collapse). The first bubble compression from the maximum bubble radius was already simulated with neglecting the laser pulse. In order to reach the value of the second maximum bubble radius, the gas pressure inside the bubble was adjusted as the parameter.

For the simulation of the shock wave propagation, the modified method of characteristics was used. The value of the quantity conserved along the characteristic line (kinetic enthalpy) was obtained from the simulation of the bubble radius, as the characteristic starts at the bubble wall. It

was found that the first shock wave produced in isooctane is stronger than in water. As the values of the shock wave velocity in isooctane attained high values, the validity of the used equation of state should be taken with care. The calculations showed that the second shock wave was generated only in water, which was in agreement with the results of the experiment.

Because energy dissipation was neglected for all calculations of the shock wave propagation, a semi-empirical solution was used to remove this defect. The model is based on the assumption of similarity of the shock pressure-time profiles (obtained from the experiment) for different shock front positions, which supplemented the system of partial differential equations describing the propagation of shock waves. This allowed to reduce the system to ordinary differential equations for the shock front peak pressure and shock wave energy in dependence on the shock front position. For this purpose an explicit formula for the enthalpy dissipation with the shock wave peak pressure was derived. The calculation of the enthalpy was based on the NIST data [54].

The calculated and measured data were used to estimate the energy distribution of the laser pulse. The results show that most of the pulse energy is consumed for the shock wave creation and bubble expansion. The energy required for evaporation of the bubble contents and the radiated energy were insignificant.

Finally, the cavitation bubble collapse near the solid wall at two different distances was simulated using the finite volume method of the commercial software Fluent. The results showed that the bubble behaviour is strongly influenced by the presence of the wall. During the bubble collapse, a high-speed liquid jet was generated against the wall. The simulation supported the finding observed during the experiments that the liquid jet is generated after the second bubble expansion is initiated.

7.2 Application and near objectives

A significant motivation for this work was to contribute to the understanding of behaviour of the cavitation bubble in various liquids. The multi-exposure method developed during the Ph.D. study can be used to investigate ultra-fast phenomena in different branches of fluid mechanics. The results obtained during the investigation of the bubble collapse near the solid wall can enhance our understanding cavitation erosion caused by the collapsing bubble, which is important in hydromachinery. The numerical model presented in detail in the thesis represents a comprehensive approach to the calculation of the laser-induced cavitation bubble dynamics including the shock wave propagation. The derived relations for the dissipation of energy at the shock wave in liquid can be implemented in other shock wave propagation models.

The near objectives of this work can be summarized as follows:

- 1) Perform a new experiment focused on the cavitation bubble collapse near the solid wall with the objective to evaluate the damaging effect of the collapsing bubble. Investigate the velocity field around the collapsing bubble using the Particle Image Velocimetry (PIV).

- 2) Improve the technique used for the measurement of the shock wave propagation based on the Laser Differential Interferometry.

7.2 CONCLUSION - APPLICATION AND NEAR OBJECTIVES

3) Investigate the density and velocity fields inside the bubble using the Particle Image Velocimetry.

4) Explain the effect of discontinuity in the bubble pressure between the first and second maximum radii, which causes discrepancy between the numerical simulation and the experiment. Use the findings to improve the bubble dynamics model.

References

- [1] BIRD, R., B., STEWARD, W., E., LIGHFOOD, E., N.: Transport phenomena. J. Wiley + Sons, New York 1960.
- [2] BIRKHOFF, G.: Stability of spherical bubbles. *Q. Appl. Math.*, 1956, vol. 13, no. 4, pp. 451.
- [3] MARŠÍK, F.: Termodynamika kontinua. Academia, Praha 1999.
- [4] ŠESTÁK, J., RIEGER, F.: Přenos hybnosti, tepla a hmoty. ČVUT, Praha 1993.
- [5] STŘEDA, I., SAZIMA, M., DOUBRAVA, J.: Termomechanika, ČVUT, Praha 1992.
- [6] SALEH, E. A. BAHAA, KARLTEICH, M.: Základy fotoniky, Matfyzpress, Praha 1994.
- [7] DOCCHIO, F., REGONDI, P., CAPON, M., R., C., MELERIO, J.: Study of the temporal and spatial dynamics of plasmas induced in liquids by nanosecond Nd:YAG laser pulses. 1. Analysis of the plasma starting times. *Appl. Opt.*, 1988, vol. 28, no. 17, pp. 3661-3668.
- [8] DOCCHIO, F., REGONDI, P., CAPON, M., R., C., MELERIO, J.: Study of the temporal and spatial dynamics of plasmas induced in liquids by nanosecond Nd:YAG laser pulses. 2: Plasma luminescence and shielding. *Appl. Opt.*, 1988, vol. 28, no. 17, pp. 3669-3674.
- [9] KENNEDY, P. K., HAMMER, D. X., ROCKWELL, B. A.: Laser induced breakdown in aqueous media. *Prog. Quantum Electron*, 1997, vol. 21, no. 3, pp. 155-248.
- [10] KELDYSH, L., V.: Ionization in the Field of a Strong Electromagnetic Wave. *Soviet Phys. JETP*, 1965, vol. 20, no. 5, pp. 1307-1314.
- [11] ZIMA, P.: Cavitation rates and bubble dynamics in gas-contaminated water, Dissertation thesis, CVUT, Praha, 2002.
- [12] BLAKE, F., G.: The onset of cavitation in liquids. Tech. Memo of I. Acoustics Res. Lab. of Harvard Univ. no. 12, 1949.
- [13] HERRING, C.: Theory of the pulsations of the gas bubble produced by an underwater explosion. OSRD Rep., no. 236., 1941.
- [14] TRILLING, L.: The collapse and rebound of a gas bubble. *J. Appl. Phys.*, 1952, vol. 23, no. 1, pp. 14-17.
- [15] FAN, C. H., LONGTIN, J. P.: Modeling optical breakdown in dielectrics during ultrafast laser processing. *Applied Optic*, 2000, Vol. 40, No. 18, pp. 3124-3131.
- [16] BRENNEN, CH., E.: Cavitation and Bubble Dynamics, Oxford University Press, Oxford 1995.
- [17] NOSKIEVIČ, J.: Kavitace v hydraulických strojích a zařízeních. SNTL, Praha 1989.
- [18] NOSKIEVIČ, J., SAMEK, L., TARABA, O.: Kavitace - Diagnostika a technické využití. SNTL, Praha 1981.
- [19] PLESSET, M., S., ZWICK, S., A.: The growth of vapour bubble in superheated liquid. *J. Appl. Phys.*, 1954, vol. 25, no. 4, pp. 493-500.
- [20] PLESSET, M., S.: On the stability of fluid flows with spherical symmetry. *J. Appl. Physics*, vol. 25, no. 1, pp. 96-98.
- [21] ŘEZNÍČEK, R.: Visualizace proudění. Academia, Praha 1972.
- [22] GAREN, W., BECKER, M., PAAL, G.: Condensation phenomena behind incident and reflected shock waves in heavy vapours at low mach numbers. 20th International symposium on shock waves, Pasadena, 1995
- [23] VOGEL, A., BUSH, S.: Shock wave emission and cavitation bubble generation by picosecond and nanosecond optical breakdown in water. *J. Acoust. Soc. Am.*, 1996, vol. 100., no 1., pp. 148-165.
- [24] VOGEL, A.: Nonlinear absorption: intraocular microsurgery and laser lithotripsy. *Phys. Med. Biol.*, 1997, vol. 42., no 1., pp. 895-912.

- [25] FUCHS, F., J.: Ultrasonic Cleaning - Fundamental theory and application. Aerospace environmental technology conference. In NASA, 1995, pp. 369-378.
- [26] KOZYUK, O., V.: Water treatment processes and devices utilizing hydrodynamic cavitation. United States Patent 7247244 (2007); "<http://www.freepatentsonline.com/7247244.html>" (2007)
- [27] PORITSKY, A.: The collapse or growth of a spherical bubble or cavity in a viscous fluid. First Nat. Cong. in Appl. Math., 1952
- [28] TOOSE, E., M., GEURTS, B., J., KUERTEN, J., B., M.: A boundary integral method for two-dimensional(non)-Newtonian drops in slow viscous flow. *J. Non-Newtonian Fluid Mech.*, 1995, vol. 60, no. 2-3, pp. 129-154.
- [29] CUNHA, F., R., SOUSA, A., J., LOEWENBERG, M.: A mathematical formulation of the boundary integral equations for a compressible stokes flow. *Mat. apl. comput.*, 2003, vol. 22, no. 1, p.53-73.
- [30] PLESSET, M., S., CHAPMAN, B., R.: Collapse of initially spherical vapour cavity in the neighbourhood of solid boundary. *J. Fluid Mech.*, 1970, Vol. 47, no. 2, pp. 283-290.
- [31] BLAKE, J., R., HOOTON, M., C., ROBINSON, P., B., TONG, R., P.: Collapsing cavities, toroidal bubbles and jet impacty. *Phil. Trans. R. Soc. Lond. A.*, 1997, vol. 355, pp. 537-550.
- [32] BLAKE, J., R., GIBSON, D., C.: Cavitation bubble near boundaries. *Ann. Rev. Fluid Mech.*, 1987, vol. 19, pp. 99-123.
- [33] BENJAMIN, T., B., ELLIS, A., T.: The Collapse of Cavitation Bubbles and the Pressures thereby Produced against Solid Boundaries. *Phil. Trans. R. Soc. Lond.*, Series A., 1966, vol. 260, no. 1110, pp. 221-240.
- [34] FRANC, J., P., MICHEL, J., M.: Fundamentals of cavitation. Springer, 2004.
- [35] RAYLEIGH: On the pressure developed in a liquid during the collapse of a spherical cavity, *Phil. Mag.*, 1917, vol. 34, pp. 94-98.
- [36] FUJIKAWA, S., AKAMATSU, T.: Effects of the non-equilibrium condensation of vapour on the pressure wave produced by the collapse of a bubble in a liquid. *J. Fluid Mech.*, 1980, vol. 97, pp. 481-512.
- [37] HICKLING, R., PLESSET, M., S.: Collapse and rebound of a spherical bubble in water. *The Physics of Fluids*, 1964, vol. 7, pp. 7-14.
- [38] PENNEY, W., G., PIKE, H., H., M.: Shock waves and the propagation of finite pulses in fluids, *Reports on Progress in Physics*, 1950, vol. 13, no. 1, pp. 46-82.
- [39] KIRKWOOD, B., T., BETHE, A., H.: The pressure wave produced by an underwater explosions. OSRD Rep., no. 588, 1942.
- [40] BRINKLEY, S., R., KIRKWOOD, G., J.: Theory of the Propagation of Shock Waves, *Physical Review*, 1947, vol. 71, no. 9, pp. 606-611.
- [41] COLE, R., H.: Underwater explosions, Princeton Univ. Press, Princeton 1948.
- [42] LANDAU, L., D., LIFSHITZ, E., M.: Fluid mechanics, Pergamon Press, Oxford 1987.
- [43] FUJIMOTO, G., J., LIU, J., M., IPPEN, E., P.: Femtosecond Laser Interaction with Metallic Tungsten and Nonequilibrium Electron and Lattice Temperatures, *Phys. Rev. Lett.*, 1984, vol. 53, no. 19, pp. 1837-1840.
- [44] RAID, R., C., PROUSNIC, J., M., SHERWOOD, T., K.: The Properties of Gases and Liquids, McGraw-Hill, N.Y. 1977.
- [45] BARNES, P., A., RIECKHOF, K., E.: Laser induced underwater sparks. *Applied Physics Letters*, 1968, vol 13, no. 8, pp. 282-284.
- [46] MICHAELIDES, E., E., LASEK, A.: Particulate flow with sublimation and evaporation and with thermal and hydrodynamics non-equilibrium. *Intern. J. of Heat and Mass Transfer*, 1991, vol. 34, no. 3, pp. 601-609.

- [47] HIRT, C., W., NICHOLS, B., D.: Volume of fluid (VOF) method for the dynamics of free boundaries, *J. Comput. Phys.*, 1981, vol. 39, pp. 201–225.
- [48] THOMPSON, P., A., SULIVAN, D., A.: On the possibility of complete condensation shock waves in retrograde fluids. *Journal of Fluid Mechanics*, 1975, vol. 70, no. 4, pp. 639-649.
- [49] GILMORE, R., H.: The growth or collapse of a spherical bubble in a viscous compressible liquid, Technical Report, no. 26-4, California Institute of Technology, Pasadena 1952.
- [50] FLINN, H., G.: Cavitation dynamics. I, *J. Acous. Soc. Amer.*, 1975, vol. 57, no. 6, pp. 1379-1396.
- [51] RICHARDSON, J., M., ARONS, A., B., HALVERSON, R., R.: Hydrodynamic Properties of Sea Water at the Front of a Shock Wave. *The Journal of Chemical Physics*, 1947, vol. 15, no. 11, pp. 785-794.
- [52] ASSAEL, M., J., DAYMOND, J., H., EXADAKTILOU, D.: An improved representation form-alkane liquid densities. *International Journal of Thermophysics*, 1994, vol. 15, no. 1, pp. 155-164.
- [53] MALTHORTA, R., WOOLF, L., A.: Thermodynamic properties of 2,2,4-trimethylpentane. *International Journal of Thermophysics*, 1990, vol. 11, no. 6, pp. 1059-1073.
- [54] LINSTROM, P., J., MALARD, W., G.: NIST Chemistry WebBook, NIST Standard Reference Database Number 69, June 2005, National Institute of Standards and Technology, Gaithersburg MD, 20899 (<http://webbook.nist.gov>).
- [55] YOUNGS, D., L.: Time-dependent multi-material flow with large fluid distortion. In: K.W. Morton and M.J. Baines, Editors, *Numerical Methods for Fluids Dynamics*, Academic Press, New York 1982.
- [56] FLUENT 6.1 DOCUMENTATION, Fluent, Inc., Lebanon, New Hampshire 2003.

Author's publications

- [57] MÜLLER, M., GAREN, W., KOCH, S., MARSIK, F., NEU, W., SABUROV, E.: Shock waves and cavitation bubbles in water and isoctane generated by Nd:YAG laser: experimental and theoretical results. *Proceedings of SPIE*, 2004, vol. 5399, pp. 275-282.
- [58] MÜLLER, M., MARSIK, F., GAREN, W.: The Energy Distribution during the Bubble Growth and Collapse in Water. *Proceeding of the 14th International Conference on the Properties of Water and Steam*, vol. 14, 2004
- [59] KOCH, S., GAREN, W., MÜLLER, M., NEU, W.: Detection of chromium in liquids by laser-induced breakdown spectroscopy (LIBS). *Applied Physics A: Materials Science & Processing*, 2004, Volume 79, Issue 4-6, pp. 1071-1073.
- [60] MÜLLER, M.: Studie dynamického chování bublinky v proměnném tlakovém poli tekutiny. Diplomová práce TU - Liberec, Liberec 2001.
- [61] MÜLLER, M.: Vliv stlačitelnosti tekutiny na dynamické chování bublinky. 21. mezinárodní konference pracovníků kateder a ústavů vyučujících mechaniku tekutin a termomechaniku. Nitra, 2002, pp. 106-110.
- [62] MÜLLER, M., MATEJEC, R., SKLIBA, J.: Numerické modelování kavitace v hydraulickém tlumiči. *Interaction and feedbacks*. Prague, 2004, pp. 103-108.
- [63] MÜLLER, M., GAREN, W., KOCH, S., POPELKA, L.: Experimental Investigation of Shock Waves and Cavitations Bubbles in Liquids. 23. mezinárodní konference pracovníků kateder a ústavů vyučujících mechaniku tekutin a termomechaniku. České Švýcarsko, 2003, pp. 69-74.
- [64] MÜLLER, M., GAREN, W., KOCH, S., MARSIK.: The Density Measurement inside the cavitation Bubble generated by Nd-YAG Laser in Glycerin. *Colloquium Fluid Dynamics 2003*. Prague, 2003, pp. 93-96.

- [65] MÜLLER, M., MARSIK, F.: The Calculation of Energy of Shock Wave Generated by Optical Breakdown in Liquids. *Computational mechanics 2006*. Nečtiny, 2006, pp. 395-400.
- [66] MÜLLER, M., MARSIK, F.: The Energy of Shock Waves Produced During the Bubble Growth Generated by Optical Breakdown in Water. *Experimental fluid mechanics 2006*. Liberec, 2006, pp. 123-130.
- [67] HRUBÝ, J., MÜLLER, M., RYCHTER, K., MAREŠ, R.: Transient Temperature Field in the Chamber for the Measurement of Surface Tension Supercooled Liquid. *Engineering Mechanics 2006*. Svatka, 2006, pp. 114-124.
- [68] POPELKA, L., MÜLLER, M., MATĚJKA, M., SEDLÁK, M., NOŽIČKA, J.: Club Class Sailplane Wing Loading And Airfoil Design. *21st Danubia-Adria Symposium on Experimental Methods in Solid Mechanics*. Zagreb, 2004, pp. 46-47.

Appendix A - Balance equation on spherical interface

This paragraph introduces the balance equations, given in the Chapter 3.1, after transformation to the spherical coordinate system with coordinates r , φ and θ . The notation used here corresponds to the spherical bubble interface illustrated in Figure 3.4. The index B denotes the variables on the inner side of the bubble interface and the index L denotes the variables on the outer side of the bubble interface (liquid side). The variables corresponding to the interface are indicated by R and the variables far from the interface are used without indexes. The balance of mass (3.10) at the interface can be written as

$$(\rho_B(v_B - \dot{R}) - \rho_L(v_L - \dot{R}))R^2 \sin\theta d\theta d\varphi = 0. \quad (\text{A.1})$$

If no mass is transferred across the surface it follows that

$$\dot{R} = v_B = v_L. \quad (\text{A.2})$$

The balance of mass (3.10) between the outward bubble boundary and the spherical surface far in the liquid can be written as

$$(\rho_L v_L R^2 - \rho v r^2) \sin\theta d\theta d\varphi = 0, \quad (\text{A.3})$$

which for incompressible liquid results in the relation between the velocity of the bubble surface and the velocity of an element far in the liquid as

$$v = v_L \frac{R^2}{r^2} = \dot{R} \frac{R^2}{r^2}, \quad (\text{A.4})$$

The balance of momentum (3.15) at the interface has the form

$$(\rho_B v_B (v_B - \dot{R}) - t_{rr}|_B - \rho_L v_L (v_L - \dot{R}) + t_{rr}|_L) R^2 \sin\theta d\theta d\varphi = 0, \quad (\text{A.5})$$

where

$$t_{rr}|_B = -p_B + \frac{2\sigma}{R} + 2\mu_B \frac{\partial v_B}{\partial r} \quad \text{and} \quad (\text{A.6})$$

$$t_{rr}|_L = -p_L + 2\mu_L \frac{\partial v}{\partial r} \quad (\text{A.7})$$

are the radial components of the stress tensor. The balance of mass in the liquid surrounding the bubble (3.9) can be written as

$$\frac{\partial \rho}{\partial t} + \frac{\partial \rho}{\partial r} v + \frac{\partial v}{\partial r} \rho + \frac{2\rho v}{r} = 0 \quad (\text{A.8})$$

and the balance of momentum (3.14) in the liquid is

$$\frac{\partial v}{\partial t} + \frac{\partial v}{\partial r} v + \frac{\partial p}{\partial r} \frac{1}{\rho} = \frac{\mu}{\rho} \left[\frac{1}{r} \frac{\partial^2 (rv)}{\partial r^2} - \frac{2v}{r^2} \right]. \quad (\text{A.9})$$

For spherical symmetry, when the combined effect of viscosity and compressibility can be neglected the equation reduces to

$$\frac{\partial v}{\partial t} + \frac{\partial v}{\partial r} v + \frac{\partial p}{\partial r} \frac{1}{\rho} = 0. \quad (\text{A.10})$$

Appendix B - Derivation of Gilmore's cavitation bubble model

In this chapter, the model of cavitation bubble dynamics in compressible viscous liquid will be rederived. The model is based on the Kirkwood-Bethe hypothesis, which was presented in Chapter 3.3.4. The considered problem can be described by the continuity (A.8) and the momentum equation (A.10) given in Appendix A. For the purpose of derivation, it is better to use the equations in the form using the total differentials:

$$\frac{1}{\rho c^2} \frac{dp}{dt} = -\frac{\partial v}{\partial r} - \frac{2v}{r}, \quad (\text{B.1})$$

$$\rho \frac{dv}{dt} = -\frac{\partial p}{\partial r}. \quad (\text{B.2})$$

The fundamental idea of the Kirkwood-Bethe hypothesis states that the variable $Y(r,t)$ called the kinetics enthalpy is propagated with the velocity $c + v$ such that

$$\frac{\partial Y}{\partial t} + (c + v) \frac{\partial Y}{\partial r} = \frac{DY}{Dt} = 0. \quad (\text{B.3})$$

This equation can be rewritten using the definition of kinetic enthalpy $Y(r,t)$ (Eq. (3.79)) in the coordinate frame moving with the liquid as

$$\frac{d}{dt} \left[r \left(h + \frac{v^2}{2} \right) \right] + c \frac{\partial}{\partial r} \left[r \left(h + \frac{v^2}{2} \right) \right] = 0. \quad (\text{B.4})$$

Note that the operator d/dt denotes the derivative moving with the liquid velocity and the operator D/Dt denotes the derivative moving with velocity $c + v$. After performing the indicated derivation Eq. (B.3) takes the form

$$r \frac{dh}{dt} + rv \frac{dh}{dt} + (c + v) \left(h + \frac{v^2}{2} \right) + cr \frac{\partial h}{\partial r} + crv \frac{\partial v}{\partial r} = 0. \quad (\text{B.5})$$

The enthalpy h satisfies the fundamental thermodynamic relation

$$dh = Tds + \frac{1}{\rho} dp. \quad (\text{B.6})$$

If the second term in Eq. (B.6) is small it can be rewritten as

$$dh = \frac{1}{\rho} dp, \quad \frac{\partial h}{\partial r} dr + \frac{\partial h}{\partial t} dt = \frac{1}{\rho} \left(\frac{\partial p}{\partial r} dr + \frac{\partial p}{\partial t} dt \right), \quad (\text{B.7})$$

where the total differentials dp and dh were evaluated in order to obtain the relations between

$$\frac{\partial h}{\partial r} = \frac{1}{\rho} \frac{\partial p}{\partial r} \quad \text{and} \quad \frac{\partial h}{\partial t} = \frac{1}{\rho} \frac{\partial p}{\partial t}. \quad (\text{B.8})$$

Applying these relations to Eqs. (B.1) and (B.2) and using the resulting relations to eliminate the partial derivative of pressure and velocity from Eq. (B.5) we obtain

$$\frac{R}{c} \frac{dH}{dt} \left(1 - \frac{\dot{R}}{c}\right) + H \left(1 - \frac{\dot{R}}{c}\right) - r \frac{d\dot{R}}{dt} \left(1 - \frac{\dot{R}}{c}\right) - \frac{3\dot{R}^2}{2} \left(1 - \frac{\dot{R}}{c}\right) = 0. \quad (\text{B.9})$$

The capital letters indicate the values of the quantities at the bubble wall.

Appendix C - Characteristics of 2D Euler's equations

In this paragraph, the characteristics for the system of equations (A.8) and (A.10) will be derived. The characteristics are curves along which the solution of the system of partial differential equations can be transformed to the solution of a system of ordinary differential equations. At first, it is convenient to transform the system (A.8) and (A.10) to a more suitable form. If pressure in the momentum equation is replaced by the variable

$$c^2 = \frac{\partial p}{\partial \rho}, \quad (\text{C.1})$$

the system can be rearranged as

$$\frac{\partial \rho}{\partial t} + v \frac{\partial \rho}{\partial r} + \rho \frac{\partial v}{\partial r} = 0, \quad (\text{C.2})$$

$$\frac{\partial v}{\partial t} + v \frac{\partial v}{\partial r} + \frac{c^2}{\rho} \frac{\partial \rho}{\partial r} = 0. \quad (\text{C.3})$$

If the first equation is multiplied by λ and added to the second equation the resulting equation we obtain

$$\frac{\partial v}{\partial t} + (v + \lambda \rho) \frac{\partial v}{\partial r} + \lambda \frac{\partial \rho}{\partial t} + \left(\lambda v + \frac{c^2}{\rho} \right) \frac{\partial \rho}{\partial r} = 0. \quad (\text{C.4})$$

The characteristic of the above equation is a curve in the r, t plane with a parameter ξ such that $x(\xi)$ and $t(\xi)$ is a point on the curve. Along the curve Eq. (C.4) can be expressed in the form

$$\frac{\partial v}{\partial \xi} + \lambda \frac{\partial \rho}{\partial \xi} = 0, \quad (\text{C.5})$$

because $dv + \lambda d\rho$ is constant along the curve. If $dv + \lambda d\rho$ is a total differential of a function, it is possible to determine the quantity propagated along the curve. The derivative along the characteristic has the following form

$$\frac{\partial}{\partial \xi} = \frac{\partial r}{\partial \xi} \frac{\partial}{\partial r} + \frac{\partial t}{\partial \xi} \frac{\partial}{\partial t}. \quad (\text{C.6})$$

If this operator is applied to Equation (C.5), it results in

$$\left(\frac{\partial r}{\partial \xi} \frac{\partial v}{\partial r} + \frac{\partial t}{\partial \xi} \frac{\partial v}{\partial t} \right) + \lambda \left(\frac{\partial r}{\partial \xi} \frac{\partial \rho}{\partial r} + \frac{\partial t}{\partial \xi} \frac{\partial \rho}{\partial t} \right) = 0. \quad (\text{C.7})$$

If this equation is divided by $\left(\frac{\partial t}{\partial \xi}\right)$ and then equalized to Equation (C.4) it follows

$$\left(\frac{\partial r}{\partial \xi}\left(\frac{\partial t}{\partial \xi}\right)^{-1}\frac{\partial u}{\partial r} + \frac{\partial u}{\partial t}\right) + \lambda\left(\frac{\partial r}{\partial \xi}\frac{\partial \rho}{\partial r}\left(\frac{\partial t}{\partial \xi}\right)^{-1} + \frac{\partial \rho}{\partial t}\right) = \frac{\partial u}{\partial t} + (u + \lambda\rho)\frac{\partial u}{\partial r} + \lambda\frac{\partial \rho}{\partial t} + \left(\lambda u + \frac{c^2}{\rho}\right)\frac{\partial \rho}{\partial r}. \quad (\text{C.8})$$

If the coefficients by the derivative are compared it follows

$$\frac{\partial r}{\partial \xi}\left(\frac{\partial t}{\partial \xi}\right)^{-1} = (v + \lambda\rho). \quad (\text{C.9})$$

$$\lambda\frac{\partial r}{\partial \xi}\left(\frac{\partial t}{\partial \xi}\right)^{-1} = \left(\lambda v + \frac{c^2}{\rho}\right). \quad (\text{C.10})$$

The combination between Equations (C.9) and (C.10) results finally in the expression of λ

$$\left(\lambda v + \frac{c^2}{\rho}\right) = v + \lambda\rho, \quad (\text{C.11})$$

from which

$$\lambda = \mp \frac{c}{\rho}. \quad (\text{C.12})$$

Equation (C.9), when the relation for λ is applied, gives the equation for the characteristic curve, because

$$\frac{\partial r}{\partial \xi}\left(\frac{\partial t}{\partial \xi}\right)^{-1} = v \mp c. \quad (\text{C.13})$$

Then

$$\frac{dr}{dt} = v \mp c. \quad (\text{C.14})$$

Equation (C.14) is the required characteristic of system (A.8) and (A.10).

Appendix D - Equation of state

The equation of state for liquids used in this work is the Tait's equation, which has two basic modifications. The first form is

$$\frac{\rho(p, T) - \rho_0(0, T)}{\rho(p, T)} = A \cdot \log\left(\frac{B(T) + p}{B(T) + p_0}\right), \quad (\text{D.1})$$

where A is a constant, $B(T)$ is a function of temperature only and the density ρ_0 is evaluated at pressure p_0 and temperature T . The second, isentropical, form of Tait's equation can be written as follows

$$\frac{\rho(p, s)}{\rho_0(0, s)} = \left[\frac{B(s) + p}{B(s) + p_0}\right]^{\frac{1}{n}}, \quad (\text{D.2})$$

where n is a constant and $B(s)$ is a function of entropy. The function $B(T)$ in Equation (D.1) is related to the function $B(s)$ in Equation (D.2) as

$$B(s) = B(t(0, s)). \quad (\text{D.3})$$

The parameter $B(s)$ can also be expressed as a function of the sound velocity c_0 and the density ρ_0 at pressure p_0 as

$$B(s) = \frac{\rho_0 c_0^2}{n}. \quad (\text{D.4})$$

As some data in the used literature were published only for Equation (D.1), these values were approximated to the isentropic form of the Tait's equation (D.1), which is the only form used in this work. For water, the parameters B , ρ_0 , c_0 , c_p for the pressure $p_0 = 0.1\text{MPa}$ expressed as the functions of temperature can be obtained from the NIST database [54] in the following form

$$B(T(0, s)) = -1.313589 \times 10^{-1} T^4 + 2.215867 \times 10^2 T^3 - 1.451439 \times 10^5 T^2 + 4.244095 \times 10^7 T + 4.267196 \times 10^9 \quad [Pa], \quad (\text{D.5})$$

$$\rho(0, T) = -1.288819 \times 10^{-7} T^4 + 1.817291 \times 10^{-4} T^3 - 9.867555 \times 10^{-2} T^2 + 2.378523 \times 10^1 T + 1.120944 \times 10^3 \quad \left[\frac{kg}{m^3}\right], \quad (\text{D.6})$$

$$c(0, T) = -6.599914 \times 10^{-7} T^4 + 9.801810 \times 10^{-4} T^3 - 5.629782 \times 10^{-1} T^2 + 1.469587 \times 10^2 T - 1.303670 \times 10^4 \quad \left[\frac{m}{s}\right], \quad (\text{D.7})$$

$$c_p(0, T) = 2.828450 \times 10^{-6} T^4 - 3.815560 \times 10^{-3} T^3 + 1.921642 T^2 \left[\frac{J}{kgK} \right] - 4.307597 \times 10^2 T + 4.040970 \times 10^4 \quad (D.8)$$

For the coefficient n , the value of 7 was used. The relations (D.5)-(D.8) were approximated within the interval from 274 to 292 K with an error lower than 1%. The function for B was proved to be valid up to 5000 MPa [41].

For isooctane, the parameters of B and ρ_0 were obtained from the data published by Malthorta [53] and instead of the parameters c_0 and c_p for isooctane, the data for heptane were used from the NIST database [54]. The heptane has similar physical properties and almost the same eccentric factor as isooctane. The parameters as the functions of temperature for the pressure $p_0 = 0.1$ MPa are given by

$$B(T) = 7.8508 \times 10^{-4} T^2 - 0.9123 T + 261.18 [MPa], \quad (D.9)$$

$$\rho(0, T) = -1.797 \times 10^{-6} T^3 + 1.1034 \times 10^{-3} T^2 - 1.0040 T + 936.721 \left[\frac{kg}{m^3} \right], \quad (D.10)$$

$$c(0, T) = -1.846816 \times 10^{-8} T^4 + 1.074077 \times 10^{-5} T^3 + 3.064072 \times 10^{-3} T^2 \left[\frac{m}{s} \right] - 6.892120 T + 2.772295 \times 10^3 \quad (D.11)$$

$$c_p(0, T) = 1.207104 \times 10^{-7} T^4 - 1.734988 \times 10^{-4} T^3 + 9.994113 \times 10^{-2} T^2 \left[\frac{J}{kgK} \right] + 2.235542 \times 10^1 T + 3.666132 \times 10^3 \quad (D.12)$$

For the coefficient n , the value of $n = 9.8$ was calculated using (D.3). The formula for B is valid up to 558 MPa within the temperature range from 278 to 373 K with a standard error up to 0.5%. The function for ρ_0 is valid in the temperature range from 278 to 323 K. The formulas for c_0 and c_p were approximated in the temperature interval from 274 to 292 K with an error lower than 1%.

Appendix E - Experimental results

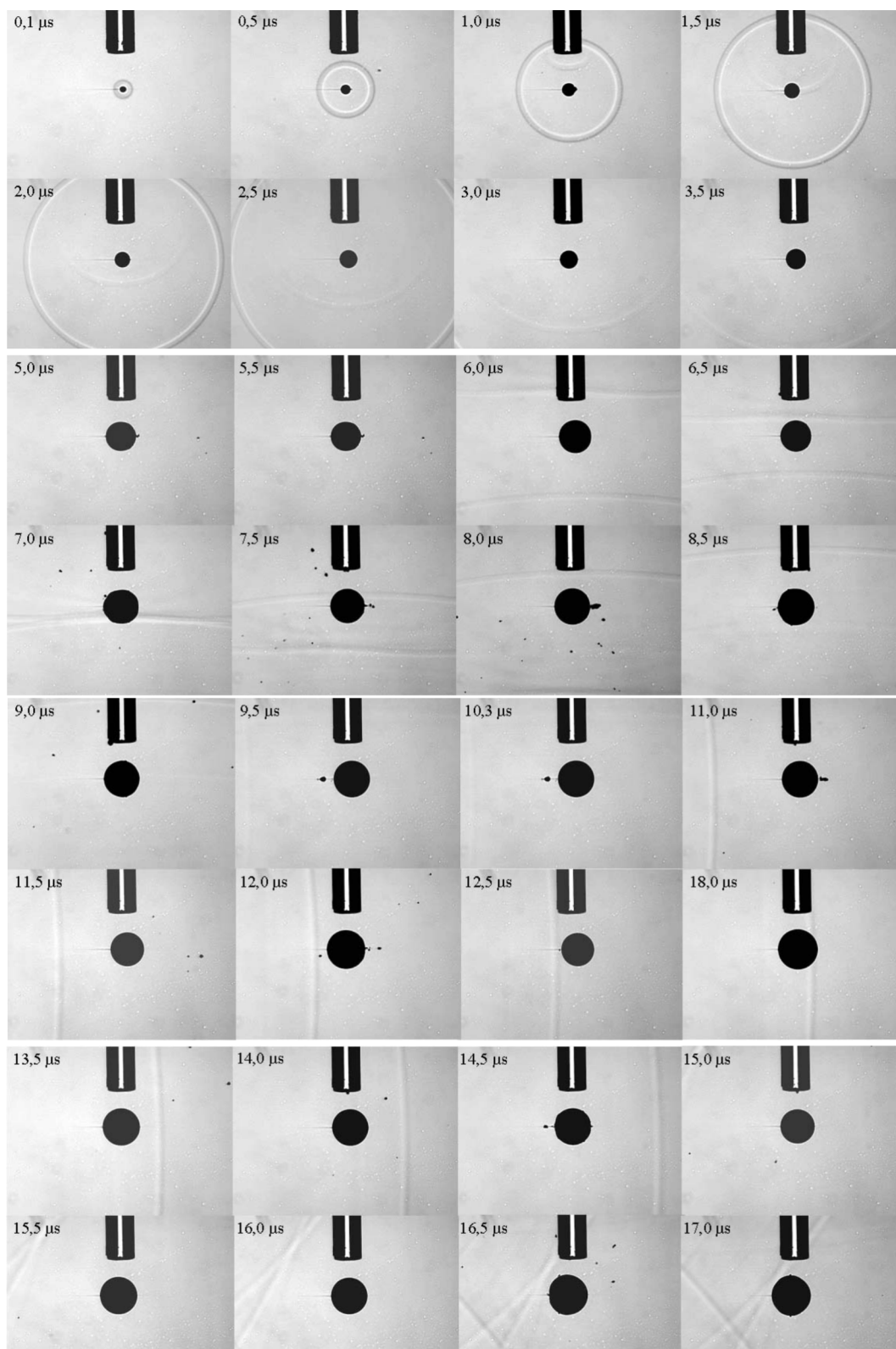


Fig.E1 Shock wave in isoctane recorded using the single-exposure mode. Shock wave reflections from optical fiber and cuvette wall are also visible.

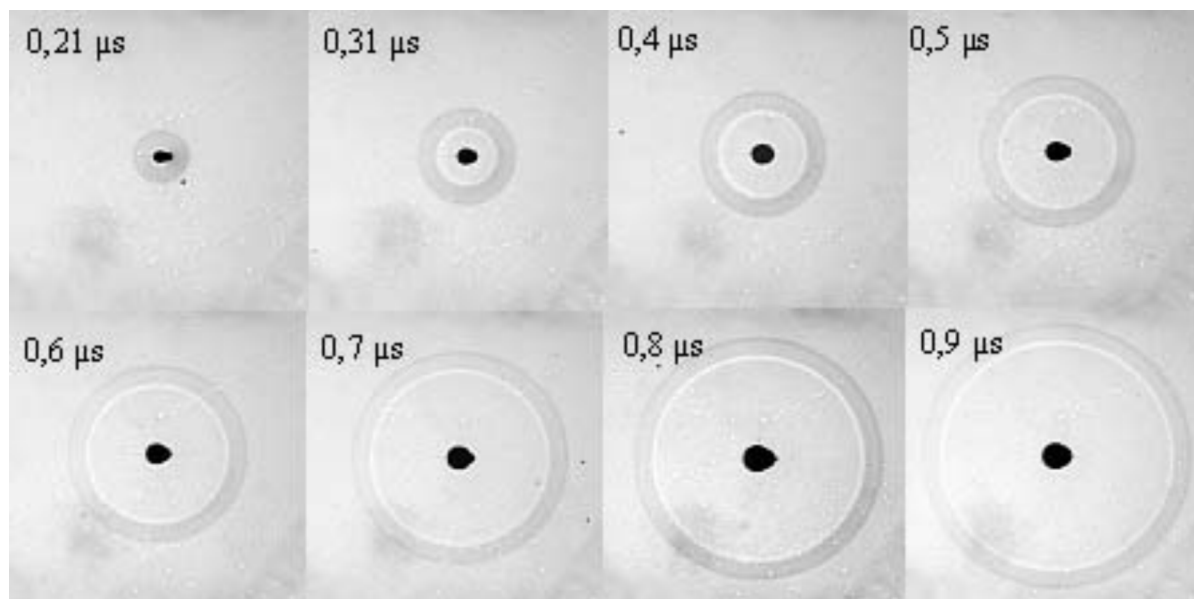


Fig.E2 Shock wave in water recorded using the single-exposure mode.

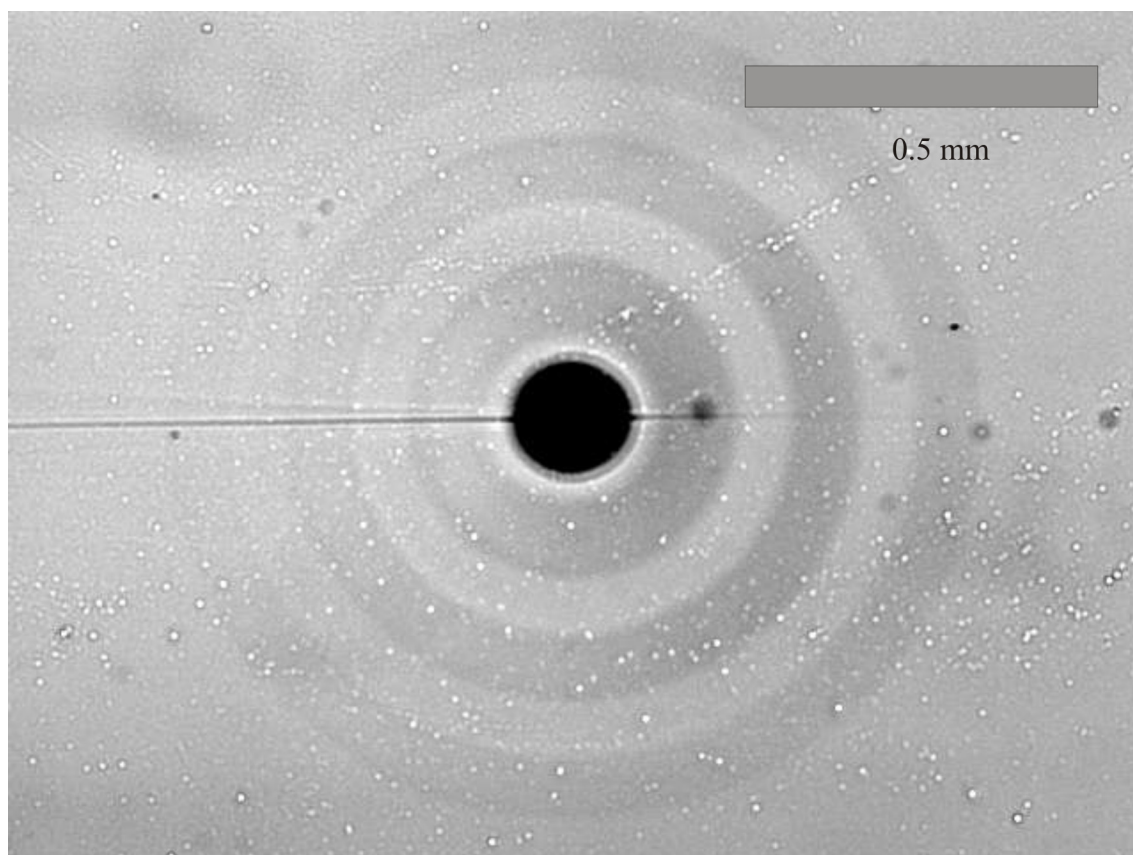


Fig.E3 Shock wave in isoctane recorded using the multi-exposure mode.

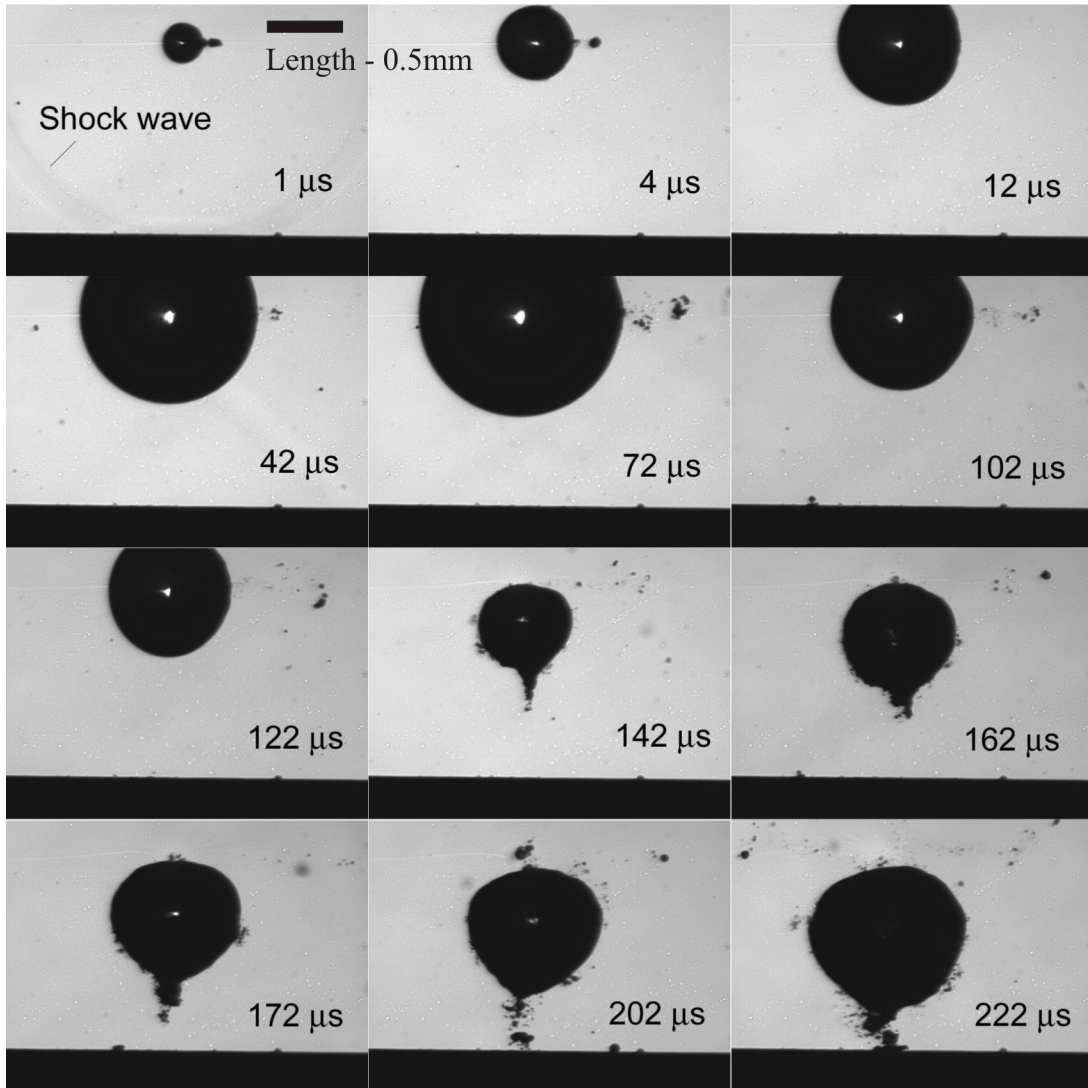


Fig.E4 Cavitation bubble collapse near the solid wall corresponding to the time history given in Figure 4.24.